

UNIVERSIDADE DE SÃO PAULO–USP
ESCOLA DE ENGENHARIA DE SÃO CARLOS
DEPARTAMENTO DE ENGENHARIA ELÉTRICA E DE COMPUTAÇÃO
PROGRAMA DE PÓS-GRADUAÇÃO EM ENGENHARIA ELÉTRICA

Lucas Rodrigues Borges

**Redução da Dose de Radiação em
Tomossíntese Mamária através de
Processamento de Imagens**

São Carlos
2017

Lucas Rodrigues Borges

**Redução da Dose de Radiação em
Tomossíntese Mamária através de
Processamento de Imagens**

Tese de doutorado apresentada ao Programa de Engenharia Elétrica da Escola de Engenharia de São Carlos como parte dos requisitos para a obtenção do título de Doutor em Ciências, Programa de Engenharia Elétrica.

Área de concentração: Processamento de Sinais e Instrumentação

Orientador: Prof. Dr. Marcelo Andrade da Costa Vieira

São Carlos

2017

Trata-se da versão corrigida da tese. A versão original se encontra disponível na EESC/USP que aloja o Programa de Pós-Graduação de Engenharia Elétrica.

AUTORIZO A REPRODUÇÃO TOTAL OU PARCIAL DESTE TRABALHO,
POR QUALQUER MEIO CONVENCIONAL OU ELETRÔNICO, PARA FINS
DE ESTUDO E PESQUISA, DESDE QUE CITADA A FONTE.

B732r Borges, Lucas Rodrigues
 Redução da Dose de Radiação em Tomossíntese Mamária
 através de Processamento de Imagens / Lucas Rodrigues
 Borges; orientador Marcelo Andrade da Costa Vieira. São
 Carlos, 2017.

 Tese (Doutorado) - Programa de Pós-Graduação em
 Engenharia Elétrica e Área de Concentração em
 Processamento de Sinais e Instrumentação -- Escola de
 Engenharia de São Carlos da Universidade de São Paulo,
 2017.

 1. Restauração de imagem. 2. Redução de ruído. 3.
 Injeção de ruído. 4. Ruído Poisson. 5. Mistura
 Poisson-Gaussiana. 6. Redução de dose de radiação. 7.
 Tomossíntese digital mamária. 8. Mamografia Digital. I.
 Título.

FOLHA DE JULGAMENTO

Candidato: Engenheiro **LUCAS RODRIGUES BORGES**.

Título da tese: "Redução da dose de radiação em tomossíntese mamária através de processamento de imagens".

Data da defesa: 14/06/2017.

Comissão Julgadora:

Resultado:

Prof. Dr. **Marcelo Andrade da Costa Vieira**
(Orientador)
(Escola de Engenharia de São Carlos/EESC)

APROVADO

Prof. Associado **Homero Schiabel**
(Escola de Engenharia de São Carlos/EESC)

APROVADO

Profa. Dra. **Ana Maria Marques da Silva**
(Pontifícia Universidade Católica do Rio Grande do Sul/PUC-RS)

APROVADO

Prof. Dr. **Andrew Douglas Arnold Maidment**
(Universidade da Pensilvânia)

APROVADO

Prof. Dr. **Alessandro Foi**
(Universidade de Tampere-Finlândia)

APROVADO

Coordenador do Programa de Pós-Graduação em Engenharia Elétrica:
Prof. Associado **Luis Fernando Costa Alberto**

Presidente da Comissão de Pós-Graduação:
Prof. Associado **Luis Fernando Costa Alberto**

*I dedicate this thesis to my parents Nivan and Dulcinéia,
to my brothers Davi and Thiago
and to my fiancée Tamiris.*

Acknowledgements

First, I would like to thank my family. Without their love and support none of this work would have been possible.

My gratitude goes also to my future wife Tamiris. Thank you for all the love and support. For being there every time I needed, and for understanding my crazy thoughts and philosophies.

Next, I would like to thank my supervisor Prof. Dr. Marcelo Vieira. Thank you for sharing your knowledge with me, for supporting my ideas, and for being a good friend.

I also would like to express my appreciation to Dr. Bakic. Thank you for having me as part of your family, I will always be grateful for that. Thank you for being there every time I needed someone to talk.

Thank you Dr. Maidment for having me in your lab, and for teaching me so much. A great part of this work was possible thanks to your support.

Thank you Dr. Foi, for also having me in your lab, and for all the discussions through Skype. Thank you for staying up until 3 a.m. so many times and help me with my work.

Thanks to Bruno and Kristen, for all the fun and time spent together in Philly! I am looking forward to visiting you.

And finally, I would like to thank the Department of Electrical and Computer Engineering at the São Carlos School of Engineering for all the support. A special thank you to Marisa and Daniel, for taking care of all the administrative aspects and giving me every support I needed.

This work was supported by the São Paulo Research Foundation (FAPESP grant no. 2013/18915-5 and 2016/25750-0), and by the Brazilian Foundation for the Coordination of Improvement of Higher Education Personnel (CAPES grant no. 88881.030443/2013-01).

*“Anyone who has never made a mistake
has never tried anything new.”
(Albert Einstein)*

Abstract

Borges, Lucas Rodrigues **Dose Savings in Digital Breast Tomosynthesis through Image Processing**. 109 p. Ph.D. Thesis – São Carlos School of Engineering, University of São Paulo, 2017.

In x-ray imaging, the x-ray radiation must be the minimum necessary to achieve the required diagnostic objective, to ensure the patient's safety. However, low-dose acquisitions yield images with low quality, which affect the radiologists' image interpretation. Therefore, there is a compromise between image quality and radiation dose. This work proposes an image restoration framework capable of restoring low-dose acquisitions to achieve the quality of full-dose acquisitions. The contribution of the new method includes the capability of restoring images with quantum and electronic noise, pixel offset and variable detector gain. To validate the image processing chain, a simulation algorithm was proposed. The simulation generates low-dose DBT projections, starting from full-dose images. To investigate the feasibility of reducing the radiation dose in breast cancer screening programs, a simulated pre-clinical trial was conducted using the simulation and the image processing pipeline proposed in this work. Digital breast tomosynthesis (DBT) images from 72 patients were selected, and 5 human observers were invited for the experiment. The results suggested that a reduction of up to 30% in radiation dose could not be perceived by the human reader after the proposed image processing pipeline was applied. Thus, the image processing algorithm has the potential to decrease radiation levels in DBT, also decreasing the cancer induction risks associated with the exam.

Keywords: Image restoration. Noise suppression. Noise injection. Poisson noise. Poisson-Gaussian mixture. Dose reduction. Breast tomosynthesis. Mammography.

Resumo

Borges, Lucas Rodrigues **Redução da Dose de Radiação em Tomossíntese Mamária através de Processamento de Imagens**. 109 p. Tese de doutorado – Escola de Engenharia de São Carlos, Universidade de São Paulo, 2017.

Em programas de rastreamento de câncer de mama, a dose de radiação deve ser mantida o mínimo necessário para se alcançar o diagnóstico, para garantir a segurança dos pacientes. Entretanto, imagens adquiridas com dose de radiação reduzida possuem qualidade inferior. Assim, existe um equilíbrio entre a dose de radiação e a qualidade da imagem. Este trabalho propõe um algoritmo de restauração de imagens capaz de recuperar a qualidade das imagens de tomossíntese digital mamária, adquiridas com doses reduzidas de radiação, para alcançar a qualidade de imagens adquiridas com a dose de referência. As contribuições do trabalho incluem a melhoria do modelo de ruído, e a inclusão das características do detector, como o ganho variável do ruído quântico. Para a validação a cadeia de processamento, um método de simulação de redução de dose de radiação foi proposto. Para investigar a possibilidade de redução de dose de radiação utilizada na tomossíntese, um estudo pré-clínico foi conduzido utilizando o método de simulação proposto e a cadeia de processamento. Imagens clínicas de tomossíntese mamária de 72 pacientes foram selecionadas e cinco observadores foram convidados para participar do estudo. Os resultados sugeriram que, após a utilização do processamento proposto, uma redução de 30% de dose de radiação pôde ser alcançada sem que os observadores percebessem diferença nos níveis de ruído e borramento. Assim, o algoritmo de processamento tem o potencial de reduzir os níveis de radiação na tomossíntese mamária, reduzindo também os riscos de indução do câncer de mama.

Palavras-chave: Restauração de imagem. Redução de ruído. Injeção de ruído. Ruído Poisson. Mistura Poisson-Gaussiana. Redução de dose de radiação. Tomossíntese digital mamária. Mamografia digital.

Contents

1	Introduction	17
1.1	Specific objectives	20
1.2	Thesis organization	20
2	Initial Considerations	23
3	Paper 1: Method for simulating dose reduction in digital mammography using the Anscombe transformation	27
4	Paper 2: Simulation of dose reduction in digital breast tomosynthesis	41
5	Paper 3: Unbiased injection of signal-dependent noise in variance-stabilized range	51
6	Paper 4: Method for simulating dose reduction in digital breast tomosynthesis	59
7	Paper 5: Pipeline for effective denoising of digital mammography and digital breast tomosynthesis	73
8	Paper 6: Restored Low-Dose Digital Breast Tomosynthesis: A Perception Study	85
9	Conclusions	103
9.1	Future works	104
9.2	Publications	105
	Bibliography	107

Introduction

Breast cancer is the most lethal cancer among women. According to statistics from the Brazilian National Institute of Cancer (INCA, 2016), 57,960 women were diagnosed with breast cancer in Brazil in 2016, and approximately 14,206 deaths were caused by the disease.

The development of breast cancer is relatively rare before the age of 35, and the chances of incidence raise progressively with age, especially in patients older than 50 years. Because the early detection of the disease increases the chances of survival up to 30% (VERONESI et al., 2005), many countries adopt breast cancer screening programs. The Brazilian Institute of Cancer recommends that women older than 50 years periodically undergo an imaging exam to detect signs of the development of breast cancer.

For many years, the gold standard imaging modality for breast cancer screening was digital mammography (DM). In DM exams, the breast is exposed to a small dose of x-ray radiation, and a conventional 2-D radiography of the breast is generated. The image is then analyzed by a radiologist, who searches for lesions such as masses, architectural distortions and microcalcifications, that may indicate the development of cancer.

In DM exams, the three-dimensional volume of the breast is projected into a two-dimensional plane. As a result, tissues and structures within the breast may overlap and obscure lesions, decreasing the sensitivity and specificity of the exam (BAKER; LO, 2011). The current sensitivity achieved by DM exams is around 80% (NCI, 2009).

Limitations related to tissue overlap are being solved with the clinical use of digital breast tomosynthesis (DBT) systems. In DBT, 2-D projections are acquired along an arc around the breast. The projections are then reconstructed into tomographic slices, similarly to Computed Tomography (CT) systems. The slices allow the 3-D visualization of the tissues and structures within the breast. Recent studies have shown that the benefits of using DBT for screening purposes include increase on the specificity and sensitivity of cancer detection (CONANT et al., 2016; SKAANE et al., 2014; DURAND et al., 2015)

Although DBT is still being developed, it is rapidly becoming a major clinical tool for breast cancer screening. It is known that the performance of radiologists is affected

by the quality of the image (HAUS; YAFFE, 2000; HUDA et al., 2003; SAUNDERS et al., 2007). Images acquired with higher radiation dose yield lower relative noise and therefore have better signal-to-noise ratio. However, excessive radiation can represent risks to the patients' health. The literature have shown the risks of cancer induction in healthy women due to the exposure to ionizing radiation during breast cancer screening (YAFFE; MAINPRIZE, 2011; GONZALEZ et al., 2009). Thus, the optimization of radiation dose versus image quality is of great interest in the medical field, especially in screening programs.

A number of works have been proposed to achieve low radiation dose and maintain acceptable image quality. Dose reduction can be achieved, *e.g.*, by the optimization of imaging protocols (KALENDER; WOLF; SUESS, 1999; GREESS et al., 2000), the improvement of reconstruction algorithms (SILVA et al., 2010; LEIPSIC et al., 2010), or by applying image restoration algorithms to images acquired at low-dose range (WANG et al., 2006; MANDUCA et al., 2009). Although many studies have investigated dose savings in conventional imaging modalities, such as CT, the availability of studies about dose savings in DBT is still very limited.

In this work we investigate the feasibility of reducing the radiation dose in DBT exams by restoring images acquired with low-dose. A few other works have been proposed to restore DBT images through denoising (WU; MAINPRIZE; YAFFE, 2012; VIEIRA; BAKIC; MAIDMENT, 2013; VIEIRA et al., 2015). However, one common issue of these methods is the incompleteness of the noise model assumed, and the smooth appearance observed in the denoised images. We propose a restoration framework dedicated to DBT systems, that considers particularities of this imaging modality, and avoids excessive smoothness by the injection of denoised signal into the scaled noisy signal.

To validate studies about dose reduction, such as the one proposed in this work, it would be desirable to have sets of images from the same patient acquired at different radiation levels. However, acquiring such dataset would require repeated exposures of each individual, resulting in risks to the patient's health. To overcome this issue, one common approach is to simulate reduced dose images starting with a standard-dose clinical image.

The development and application of simulation methods for standard imaging modalities such as CT and DM has been widely explored in the literature (FRUSH et al., 2002; SAUNDERS; SAMEI, 2003; BATH et al., 2005; MASSOUMZADEH et al., 2009; SVALKVIST; BATH, 2010; MACKENZIE et al., 2012; MACKENZIE et al., 2014). However, to the best of our knowledge, no methods have been proposed or validated on DBT images up to this point.

The task of simulating dose reduction in x-ray images can be divided into two steps: signal scaling and noise insertion. The first step, signal scaling, is straightforward and depends on the linearity of the system being simulated. Generally, x-ray detectors do not present an exact linear response to x-rays, however it is possible to perform mathematical operations to linearize the response.

The second step, noise injection, must be performed with special attention. In digital mammography images, for example, quantum noise is predominant. The quantum noise follows the Poisson distribution, and therefore has the variance described as a function of the underlying true signal. In clinical applications, the true signal is unknown and therefore the simulation of quantum noise requires some initial assumptions.

The literature presents a number of works that overcome this issue by assuming that the clinical image, acquired with a standard radiation dose, is a good approximation of the underlying signal (SAUNDERS; SAMEI, 2003; BATH et al., 2005; SVALKVIST; BATH, 2010; MACKENZIE et al., 2012; MACKENZIE et al., 2014). This assumption converges asymptotically as the expectation of the signal increases, as shown in (BORGES; VIEIRA; FOI, 2016), thus an error is associated with this assumption at low photon fluence applications.

Thus, before the restoration method could be validated, we proposed an alternative algorithm for injection of quantum noise into clinical images, to simulate dose reduction. The method performs noise injection in a variance-stabilizing range, and therefore does not require any previous knowledge of the signal. To validate this concept, initial tests were performed on DM images, assuming a simple model of pure white quantum noise. The description and validation of this method is presented in **Paper 1**. The work also presents a complete review of the simulation methods presented in the literature.

As our main goal is to investigate dose reduction in DBT images, in the second part of this work we evaluated our previously presented method applied to DBT images. Because of the lower radiation doses used to acquire each DBT projection, the assumption of pure quantum noise is no longer valid and the electronic noise generated by the detector must be accounted for. Thus, the approximation of a pure quantum noise model resulted in simulation errors, which were published in **Paper 2**.

To account for the imaging modalities with lower energies, our noise injection operator was optimized for low photon fluence applications and the new operator was presented in **Paper 3**. Finally, the operator was modified to adopt a Poisson-Gaussian model, rather than a pure Poisson. The updated model accounts for both quantum and electronic noise. The operator was also modified to account for pixel cross-talk, which causes the noise to be frequency-dependent (non-white). **Paper 4** describes the complete operator, and the validation on DBT images using objective metrics and a human observer experiment.

After we developed the tool capable of accurately simulating dose reduction in DBT images, we have proposed an image denoising pipeline. In this pipeline, noise suppression was performed on the raw DBT projections. The efficiency of the denoising algorithm was improved by choosing a noise model that faithfully represents what is found in DBT images. A Gaussian-Poisson model was chosen, and features such as spatially varying quantum gain, and detector offset were considered in our model. The denoising pipeline was presented and validated on **Paper 5**.

In **Paper 5** the goal of the proposed denoising pipeline is to enhance, as much as

possible, the signal-to-noise ratio (SNR), starting with low-dose DBT images with low SNR. Although the pipeline yields images with high SNR and very low noise, the smooth appearance of denoised images is not appreciated by radiologists.

Thus, the next step of our work was to propose an image restoration framework that uses the denoising pipeline presented previously and controls the image smoothness and SNR by the injection of noisy signal into a denoised signal. The method was formalized and presented in **Paper 6**.

Paper 6 also presents the final experiment of this Ph.D. thesis. Using a two-alternative forced-choice (2-AFC) human observer study we analyzed the human perception of noise and blur from restored DBT images at a range of radiation dose levels. This study allowed the definition of a dose reduction point at which no differences in noise and blur levels could be perceived by the observer.

The results presented by this Ph.D. thesis are preliminary to a much greater study that would lead to dose savings in breast cancer screening. Further studies are necessary before the implementation of the proposed method into clinical practice.

1.1 Specific objectives

- ❑ Review methods for simulation of dose reduction presented in the literature.
- ❑ Propose an improved algorithm and validate the concept using DM images.
- ❑ Evaluate the performance of the proposed simulation method when applied to DBT images.
- ❑ Improve the method to work properly with DBT images.
- ❑ Evaluate and validate the method using a dataset of clinical DBT images.
- ❑ Propose a dedicated image restoration framework for DBT images acquired at low-doses.
- ❑ Evaluate and validate the feasibility of achieving dose reduction by restoring DBT images acquired at low radiation dose.

1.2 Thesis organization

This Ph.D. thesis was organized into eight chapters. The first chapter introduces the problems addressed by this work, and gives a general overview of the solutions proposed. Chapter 2 gives specific information about the work and explains how each portion of the work is connected to the main objective.

Chapters three to eight present a series of papers either published or submitted during the development of this project. They explain in details the methodology, materials and validation used on each portion of the work. The papers are:

- **Paper 1** - Borges, L.R.; Oliveira, H.C.; Nunes, P.F.; Bakic, P.R.; Maidment, A.D.A.; Vieira, M.A.C. Method for simulating dose reduction in digital mammography using the Anscombe transformation. **Medical Physics**. v. 43, n. 6, p. 2704-2714, 2016.
- **Paper 2** - Borges, L.R.; Guerrero, I.; Bakic, P.R.; Maidment, A.D.A.; Schiabel, H.; Vieira, M.A.C. Simulation of dose reduction in digital breast tomosynthesis. In: **International Workshop on Digital Mammography**, Springer International Publishing, p. 343-350, 2016.
- **Paper 3** - Borges, L.R.; Vieira, M.A.C.; Foi, A. Unbiased injection of signal-dependent noise in variance-stabilized range. **IEEE Signal Processing Letters**, v. 23, n. 10, p. 1994-1998, 2016.
- **Paper 4** - Borges, L.R.; Guerrero, I.; Bakic, P.R.; Foi, A.; Maidment, A.D.A.; Vieira, M.A.C. Method for simulating dose reduction in digital breast tomosynthesis. **IEEE Transactions on Medical Imaging journal**. Preprint available at: <http://dx.doi.org/10.1109/TMI.2017.2715826>
- **Paper 5** - Borges, L.R.; Bakic, P.R.; Foi, A.; Maidment, A.D.A.; Vieira, M.A.C. Pipeline for effective denoising of digital mammography and digital breast tomosynthesis. **Proceedings SPIE 10132**, Medical Imaging 2017: Physics of Medical Imaging, 1013206, 2016.
- **Paper 6** - Borges, L.R.; Bakic, P.R.; Maidment, A.D.A.; Vieira, M.A.C. Restored low-dose digital breast tomosynthesis: a perception study. Submitted to the *Physics in Medicine and Biology* journal (May 15 2017).

Chapter nine presents the general conclusions of this work, along with future directions. A list of other scientific works published during this project is also provided in chapter 9.

Initial Considerations

The initial portion of this Ph.D. project aimed at developing algorithms to simulate dose reduction in x-ray images, followed by a clinical application of the method that explores dose savings in digital breast tomosynthesis (DBT).

The first two noise-injection operators developed in this thesis adopted a pure Poisson noise model. This model describes the uncertainties predominantly found in applications such as microscopy, many of the x-ray systems, photon-counting systems, etc.

In a Poisson model, the noise variance is a function of the underlying true signal - and therefore is classified as signal-dependent noise. This poses a challenge to the simulation of these variables in real applications. In real systems, it is not possible to have access to the underlying true signal, and therefore an error is associated to the simulation of extra noise into real-world images.

The proposed method takes advantage of the properties of variance stabilizing transformations (VST), to perform accurate injection of extra signal-dependent noise into Poisson variables. In the variance stabilizing range, the signal-dependency between the noise variance and the signal expectation is ceased. In this scenario, the extra injected noise is independent of the underlying signal, and the simulation process becomes simpler and accurate.

The first operator was based on the Anscombe Transformation, a VST for Poisson variables. The validation was performed on digital mammography images (DM). Due to the high photon fluence found in DM images, the noise can be modeled as Poisson with no harm to the accuracy. This portion of the work was summarized in **Paper 1**. The article was published by the *Medical Physics* journal, in June 2016, which has high international relevance (Impact Factor: 2.63), and is classified as A1 by the CAPES Qualis rank. The work was selected to stamp the journal's cover page.

The first operator yielded high accuracy performing noise injection to DM images, as seen in **Paper 1**. However, applications such as tomosynthesis and computed tomography (CT) have lower photon fluence range, and thus some of the assumptions necessary for the first operator are not fulfilled, resulting in errors. A preliminary study was conducted to

explore the direct application of the method presented in **Paper 1** to DBT images. The results are organized in **Paper 2**, which was published by the *Lecture Notes in Computer Science*, by Springer, and presented at the *International Workshop in Breast Imaging*. The paper was awarded the student fellowship at the conference. Although the results were promising, the current operator yielded higher errors compared to **Paper 1**.

The next step was to optimize the operator to perform accurate noise injection in low photon fluence applications. The optimization was achieved by using a different VST, other than the Anscombe Transformation used in **Papers 1 and 2**. The new transformation follows the same square root type of function as the Anscombe VST, but had the coefficients optimized to minimize the errors on the variance and expectation of the simulated distribution. The second operator was demonstrated and validated using hypothetical signals and fluorescence images. The formalization and validation were organized in **Paper 3**, which was published by the *IEEE Signal Processing Letters* journal, in October 2016. This journal also has high reputation and visibility in the signal processing field (Impact Factor: 2.53), and is classified as A1 by the CAPES Qualis rank.

To increase the accuracy and be appropriate for DBT images, two other aspects must be considered in our third noise injection operator: the electronic noise, and the pixel crosstalk. The electronic noise is caused by the random fluctuations on the electronics of the system and can be described by a signal-independent Gaussian noise model. Thus, the pure white Poisson model is no longer adequate for this application, and a Poisson-Gaussian model must be adopted. The pixel crosstalk is caused by physical aspects of the system, such as electron drift, and it causes the noise to be frequency-dependent (non-white).

The new operator was inspired by the Generalized Anscombe Transformation (GAT). The GAT is a VST for Poisson-Gaussian variables, such as the noise found in DBT images. The injection was performed in a variance-stabilized range, similarly to the previous operators. Furthermore, an additional step was performed to create noise correlation, which simulates the pixel crosstalk.

In our previous publications, the evaluation of the simulation method was performed using anthropomorphic phantom images, which mimics the anatomical and physical aspects of the human breast. The use of phantoms allowed the approximation of a ground-truth image, and thus objective metrics of similarity were used to compare statistics of the simulated and real images. For the validation of the third operator, once more the phantoms were used. However, in addition to objective measurements, a human observer experiment was also conducted. In this experiment, experienced medical physicists evaluated a set of phantom images to assess the similarity of the noise levels in real and simulated images. The subjective evaluation using human observers is closer to the real clinical task in image interpretation, and therefore is an important aspect to be investigated.

The formalization and validation of the third operator are presented in **Paper 4**. The work has been submitted and accepted for publication at the *IEEE Transactions in Medical Imaging*. This journal is relevant to the medical imaging and signal processing fields (Impact Factor: 3.94), and is classified as A1 in the CAPES Qualis rank.

After developing and validating the operators used to simulate dose reduction DBT images, the second part of the thesis focuses on the clinical application of the method. The goal is to investigate the feasibility of restoring DBT images, acquired at lower radiation levels, to achieve a similar SNR regime as full-dose acquisitions.

First, a denoising pipeline was proposed. A Poisson-Gaussian model was adopted, and particularities such as spatially varying quantum gain, pixel offset and electronic noise were considered. Furthermore, an appropriate VST allowed the use of "off-the-shelf" state-of-the-art denoising techniques developed for Gaussian variables. The pipeline was formalized and validated using DM and DBT phantom images. The results are organized in **Paper 5**. The work was submitted and presented at the *2017 SPIE Medical Imaging Conference*, and was awarded runner-up on the best student paper on the physics track.

The final goal of this thesis was to study the feasibility of dose savings in clinical DBT images by restoring low-dose acquisitions. To achieve the SNR of full-dose acquisitions, DBT projections acquired at low-dose were denoised, and a weighted-average was used to inject the denoised signal into the noisy signal. This process avoids the excessive signal smoothing found in denoised images. The final evaluation was presented in **Paper 6**. It contains a 2-AFC human observer experiment to compare the noise and blur levels from restored low-dose and full-dose acquisitions. **Paper 6** has been submitted to the *Physics in Medicine and Biology* journal, which also has relevant impact in the field (Impact Factor: 2.76) and is classified as A1 by the CAPES Qualis rank.

Paper 1: Method for simulating dose reduction in digital mammography using the Anscombe transformation

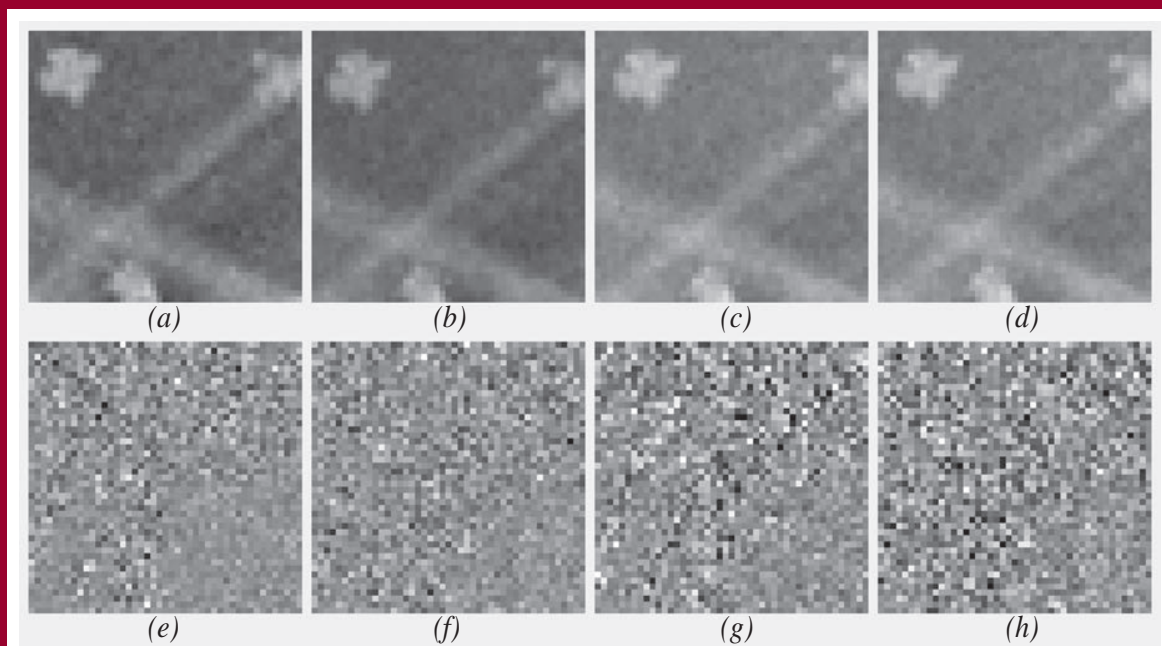
This paper was granted open access through the Creative Commons program. The readers are free to copy and redistribute the material in any medium or format, as long as the appropriate credit is given. <http://dx.doi.org/10.1118/1.4948502>

Medical Physics

AVAILABLE ONLINE—See <http://www.medphys.org>

June 2016 Volume 43, Number 6

The International Journal of Medical Physics Research and Practice



Examples of simulated and real images of a physical 5 cm thick anthropomorphic breast phantom at two entrance radiation doses, and the corresponding noise. Top-row: Magnified view of a region of interest extracted from the (a) real image acquired with 5.29 mGy entrance dose; (b) simulated image (5.29 mGy); (c) real image acquired with 3.02 mGy; (d) simulated image (3.02 mGy). Bottom-row: Residual noise masks calculated for the: (e) real image acquired with 5.29 mGy; (f) simulated image (5.29 mGy); (g) real image acquired with 3.02 mGy; (h) simulated image (3.02 mGy). For the simulated images, the inserted noise is obtained by acquiring images of a flat-field phantom at the standard radiation dose and at the simulated dose. Using the Anscombe transformation, a relationship is created between the calculated noise mask and the scaled image, resulting in a simulated clinical mammogram with the same noise and gray level characteristics as a clinical image acquired at the lower radiation dose. The residual noise masks were calculated by subtracting the noiseless approximation of the signal from each image, where the 'noiseless' signal was approximated by averaging 5 realizations for each dose.

[Adapted from Figure 12 from Borges, de Oliveira, Nunes, Bakic, Maidment, and Vieira, "Method for simulating dose reduction in digital mammography using the Anscombe transformation," *Med. Phys.* 43, 2704-2714 (2016)].

Published by the American Association of Physicists in Medicine (AAPM) with the association of the Canadian Organization of Medical Physicists (COMP), the Canadian College of Physicists in Medicine (CCPM), and the International Organization for Medical Physics (IOMP) through the AIP Publishing LLC. *Medical Physics* is an official science journal of the AAPM and of the COMP/CCPM/IOMP.

Medical Physics is a hybrid gold open-access journal.

Method for simulating dose reduction in digital mammography using the Anscombe transformation

Lucas R. Borges, Helder C. R. de Oliveira, Polyana F. Nunes, Predrag R. Bakic, Andrew D. A. Maidment, and Marcelo A. C. Vieira

Citation: *Medical Physics* **43**, 2704 (2016); doi: 10.1118/1.4948502

View online: <http://dx.doi.org/10.1118/1.4948502>

View Table of Contents: <http://scitation.aip.org/content/aapm/journal/medphys/43/6?ver=pdfcov>

Published by the [American Association of Physicists in Medicine](#)

Articles you may be interested in

[Method of measuring NEQ as a quality control metric for digital mammography](#)

Med. Phys. **41**, 031905 (2014); 10.1118/1.4865175

[Monte Carlo performance on the x-ray converter thickness in digital mammography using software breast models](#)

Med. Phys. **39**, 6638 (2012); 10.1118/1.4757919

[Effects of exposure equalization on image signal-to-noise ratios in digital mammography: A simulation study with an anthropomorphic breast phantom](#)

Med. Phys. **38**, 6489 (2011); 10.1118/1.3659709

[A technique optimization protocol and the potential for dose reduction in digital mammography](#)

Med. Phys. **37**, 962 (2010); 10.1118/1.3276732

[The value of scatter removal by a grid in full field digital mammography](#)

Med. Phys. **30**, 1712 (2003); 10.1118/1.1584044

View this article in issue here

"It can be reasonably postulated that verification of the dose distribution inside the patient was always the intent behind the secondary calculation process..."



Free White Paper

Secondary Calculations:
Revisiting Rationale, Rethinking
Methodology

NEW! DoseCHECK™
3D Independent Secondary Dose Check



Method for simulating dose reduction in digital mammography using the Anscombe transformation

Lucas R. Borges,^{a)} Helder C. R. de Oliveira, and Polyana F. Nunes
*Department of Electrical and Computer Engineering, São Carlos School of Engineering,
University of São Paulo, 400 Trabalhador São-Carlense Avenue, São Carlos 13566-590, Brazil*

Predrag R. Bakic and Andrew D. A. Maidment
*Department of Radiology, Hospital of the University of Pennsylvania, University of Pennsylvania,
3400 Spruce Street, Philadelphia, Pennsylvania 19104*

Marcelo A. C. Vieira
*Department of Electrical and Computer Engineering, São Carlos School of Engineering,
University of São Paulo, 400 Trabalhador São-Carlense Avenue, São Carlos 13566-590, Brazil*

(Received 20 July 2015; revised 14 April 2016; accepted for publication 18 April 2016; published 6 May 2016)

Purpose: This work proposes an accurate method for simulating dose reduction in digital mammography starting from a clinical image acquired with a standard dose.

Methods: The method developed in this work consists of scaling a mammogram acquired at the standard radiation dose and adding signal-dependent noise. The algorithm accounts for specific issues relevant in digital mammography images, such as anisotropic noise, spatial variations in pixel gain, and the effect of dose reduction on the detective quantum efficiency. The scaling process takes into account the linearity of the system and the offset of the detector elements. The inserted noise is obtained by acquiring images of a flat-field phantom at the standard radiation dose and at the simulated dose. Using the Anscombe transformation, a relationship is created between the calculated noise mask and the scaled image, resulting in a clinical mammogram with the same noise and gray level characteristics as an image acquired at the lower-radiation dose.

Results: The performance of the proposed algorithm was validated using real images acquired with an anthropomorphic breast phantom at four different doses, with five exposures for each dose and 256 nonoverlapping ROIs extracted from each image and with uniform images. The authors simulated lower-dose images and compared these with the real images. The authors evaluated the similarity between the normalized noise power spectrum (NNPS) and power spectrum (PS) of simulated images and real images acquired with the same dose. The maximum relative error was less than 2.5% for every ROI. The added noise was also evaluated by measuring the local variance in the real and simulated images. The relative average error for the local variance was smaller than 1%.

Conclusions: A new method is proposed for simulating dose reduction in clinical mammograms. In this method, the dependency between image noise and image signal is addressed using a novel application of the Anscombe transformation. NNPS, PS, and local noise metrics confirm that this method is capable of precisely simulating various dose reductions. © 2016 American Association of Physicists in Medicine. [<http://dx.doi.org/10.1118/1.4948502>]

Key words: dose reduction, digital mammography, Anscombe transformation, quantum noise

1. INTRODUCTION

To validate studies of radiation dose reduction, it is necessary to have a set of clinical images acquired from the same patient at different radiation levels. The availability of such images is limited, since these require repeated irradiation of patients. One way to overcome this limitation is to use realistic breast phantoms; anthropomorphic phantoms are capable of mimicking the appearance of breast tissues, either as physical models^{1,2} or through digital simulation.^{3–5}

Another approach to validate dose reduction methods is to simulate the reduced dose by postprocessing clinical images.^{6–12} In fact, this method is used frequently when studying the influence of dose reduction on the detection of

breast lesions.^{13–15} Saunders and Samei⁶ proposed a method to simulate different exposures that uses a noiseless image as input. However, it is not possible to acquire noiseless clinical images. Furthermore, the method is based on a radially symmetric noise power spectrum (NPS),¹⁶ which does not account for the anisotropic noise in digital mammograms.

Bâth *et al.*⁷ presented a method capable of simulating dose reduction in radiographic images using information extracted from the 2D NPS, therefore accounting for the anisotropic behavior of the noise. However, the method is based on the assumption that the detective quantum efficiency (DQE)¹⁶ is approximately constant over the range of doses simulated. In digital mammography, the additive noise has a relevant influence on the DQE for low doses.¹⁷

Kroft *et al.*⁸ argued that to be clinically useful, the noise simulation algorithm has to be simple. With this argument, they proposed an alternative approach for measuring the amount of noise to be added to the image, discarding the NPS. This method was based on the local standard deviation of the image. However, as shown by the authors themselves,⁹ although the simulated images have the same local standard deviation as real images, they have different NPS. Since the standard deviation is not a good metric of the image noise when comparing images with different NPS,¹⁸ the clinical application of this method is questionable.

In recent work, Svalkvist and Båth¹⁰ presented a modification of the method proposed by Båth *et al.*⁷ that accounts for the DQE variation with dose. However, as pointed by the authors themselves,¹⁰ the method does not account for local variations in pixel gain, caused by the nonuniformities between detector elements.

Other methods have also been proposed recently,^{11,12} based on the NPS. However, to account for the spatial dependency of the variance, these methods propose the application of algorithms to remove flat-field corrections before simulating the dose reduction, to eliminate the spatial dependency of the noise.

A new method for simulating dose reduction in digital mammograms is proposed in this paper. The method is based on the local simulation of noise calculated using the local variance of uniform images. It can be applied to flat-fielded clinical images and accounts for the anisotropy of the noise and DQE variations. The method is based on a novel idea of inserting noise after applying a variance-stabilizing transformation (e.g., Anscombe transformation). In the variance-stabilized domain, noise is independent of the mean pixel value; therefore, the inserted noise can be modeled based only on the spatial dependency of the variance, thus accounting for the flat-field corrections. The dependency between the noise mask and the pixel value is created when the inverse transformation is applied.

2. BACKGROUND ON THE ANSCOMBE TRANSFORMATION

The Anscombe transformation is a variance-stabilizing transformation that converts a random variable with Poisson distribution into an approximately Gaussian distribution, with zero mean and unity variance.¹⁹ Let the degraded image, $g(x, y)$, at spatial coordinates x and y , be the random variable. The Anscombe transformation applied on $g(x, y)$ is given by the following:



FIG. 1. Schematic of a common application for the Anscombe transformation.

$$\mathcal{A}\{g(x, y)\} = 2\sqrt{g(x, y) + \frac{3}{8}}. \tag{1}$$

The original inverse transformation proposed by the author¹⁹ is biased for small counting values ($\lambda < 10$); therefore in applications where the counting values are small, the results obtained after using the inverse transformation are different from the expected values. In recent work, Mäkitalo and Foi²⁰ proposed a new approach for the inverse transformation, without any bias for small counts. Although counting values are considerably higher in mammography images ($\lambda \gg 10$), in this work, we used the unbiased exact inverse, available online.²¹

The Anscombe transformation has been commonly explored in the field of image denoising, where a noisy image $g(x, y)$ is filtered in the Anscombe domain using filters designed to treat Gaussian signal-independent noise.^{22,23} Figure 1 illustrates the rationale for this transformation; the Anscombe transformation transforms the image noise into signal-independent noise.

The new approach consists on adding signal-independent noise to the image in the Anscombe domain and applying the inverse transformation afterward. Figure 2 shows a schematic of the new application.

Let $Im(x, y)$ be the noiseless original image and $\eta(x, y)$ be a mask containing signal-independent noise. The image contaminated by signal-dependent noise, $Im_{Noisy}(x, y)$, is given by

$$Im_{Noisy}(x, y) = \mathcal{A}^{-1}\{\mathcal{A}\{Im(x, y)\} + \eta(x, y)\}. \tag{2}$$

In the particular case when $\eta(x, y)$ is a Gaussian signal-independent noise mask with unity variance and zero mean, the inserted noise will follow the Poisson distribution.

As a preliminary empirical test of this method, we created a 512×512 pixel synthetic image containing three distinct regions with various gray levels. Each region simulates a counting process with a different mean (λ). The Anscombe transformation was applied to the synthetic image and a Gaussian signal-independent mask with zero mean and unity variance was added to the image in the Anscombe domain. After applying the inverse transformation proposed by Mäkitalo and Foi,²⁰ a dependency was created between the noise mask and the signal. Figure 3 illustrates the results of

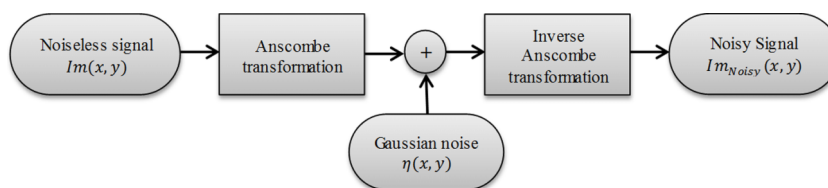


FIG. 2. Novel application for the Anscombe transformation.

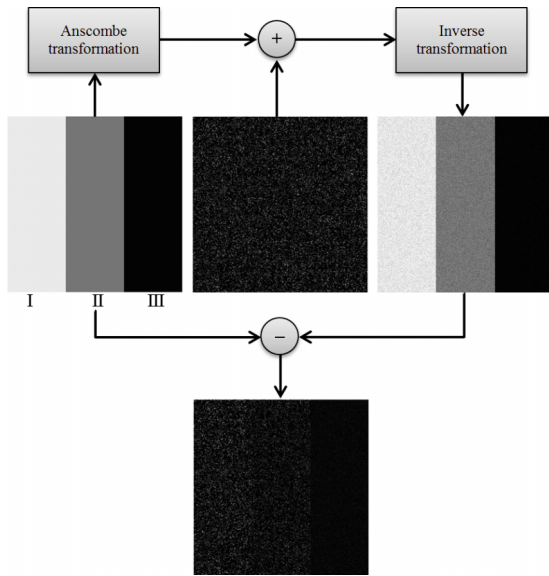


FIG. 3. Top-left: synthetic noiseless image [Average signal: (I) 60 000 (II) 30 000 (III) 1000]. Top-center: Gaussian signal-independent noise (zero mean and unity variance). Top-right: noisy image after addition in the Anscombe domain and inverse Anscombe transformation. Bottom: Poisson signal-dependent noise subtracted from the noisy image. Contrast and brightness were improved for better visualization.

this process. Note that after processing, the noise is signal-dependent.

Table I shows the standard deviation (std) from each simulated stripe from Fig. 3 (bottom), along with the average signal (λ) in that region and the expected theoretical standard deviation for a Poisson distribution, calculated²⁴ using

$$\text{std}(X) = \sqrt{\lambda}, \tag{3}$$

where X is a region of the image with average signal of λ .

Table I illustrates the potential of using the Anscombe transformation to contaminate a noiseless image with signal-dependent noise. However, three problems are associated with the use of this method for simulating noise in digital mammography images acquired with lower-radiation dose. First, a clinical mammogram must be used as input for the proposed method. However, such an image cannot be used as a noiseless approximation of the signal once it has been contaminated with noise from the acquisition system.

Second, the method produces unscaled pure Poisson noise. In clinical mammography, very few systems use photon-

TABLE I. Comparison between theoretical std and measured std obtained using the inverse Anscombe transformation to convert Gaussian signal-independent noise into Poisson signal-dependent noise.

Region	Average signal (λ) (from Fig. 3, top-left)	Measured std (from Fig. 3, bottom)	Expected std [from Eq. (3)]
I	60 000	245.4	245.0
II	30 000	173.0	173.2
III	1 000	31.6	31.6

counting detectors; most systems use energy integrating detectors. Therefore, the noise added in the Anscombe domain should be different from a Gaussian with unity variance and must be estimated. Finally, the noise found in mammograms depends on the position of the pixel on the field, due to the flat-fielding process, which corrects the nonuniformity of the field caused by the heel effect and the oblique incidence of x-rays.¹⁷

In Sec. 3, we address each of these problems and present ways to solve them using the new algorithm proposed in this work.

3. MATERIALS AND METHODS

3.A. Method

Let $Y_o(x, y)$ be a clinical mammogram at coordinates x and y . To simulate a low-dose mammogram ($Y_{\text{sim}}(x, y)$) acquired at the simulated dose D_{sim} , it is necessary to acquire two uniform images [$H_o(x, y)$ and $H_{\text{sim}}(x, y)$] at the original and simulated doses, respectively. These uniform images determine how much noise must be added to the clinical image acquired at the original dose to ensure that the noise is correctly simulated for the lower-dose acquisition.

The proposed method consists of three steps. In the first step, all of the images are linearized and the images acquired at the original dose are scaled by the dose reduction factor. The second step is to simulate the noise distribution at each pixel of the image, using local information extracted from the uniform images acquired at the different doses. Lastly, a dependency is created between the simulated noise and the clinical image acquired using the standard radiation dose to generate the simulated low dose image.

This processing method assumes that the input images are in the raw format. The raw format, identified as “for processing” in the DICOM header of the image, contains image data which is minimally processed, lacking processing to improve tissue contrast for easier interpretation by the radiologist. Figure 4 shows an overview of the proposed method.

Section 3.A is divided into three subsections where each step of the algorithm will be explained in more detail. Indexes L , S , and A indicate that the associated variables are linearized, scaled, and in the Anscombe domain, respectively.

3.A.1. Linearization and scaling

Images acquired with lower-radiation dose have lower overall signal, as compared to standard-dose mammograms. Therefore, initially we need to adjust the gray level of the clinical mammogram to match the simulated lower-dose acquisition. If we consider an x-ray system where the radiation dose is the input variable and the mean pixel value is the output, it is possible to scale the gray level of an image acquired by this equipment as long as the relation between these quantities is linear.

Although the relationship between mean pixel value and radiation dose usually has an offset, it is possible to remove this

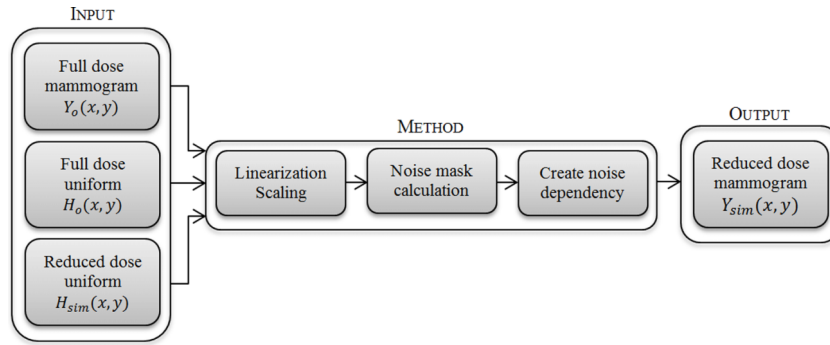


FIG. 4. Overview of the method proposed in this work.

value.⁷ One simple way to correct this problem is to subtract the offset from the image before the processing is performed, and then to add the offset back after all the processing steps are complete. To find the offset, we acquire at least two uniform images at different radiation doses using the equipment to be simulated. Then, we calculate a linear regression to find the relation between dose and mean pixel value of the uniform images. The constant term of the regression is the photodetector offset.

After linearizing the image, it is possible to scale the gray levels to simulate the distribution of an image acquired at a lower-radiation dose. Thus, pixel is multiplied by a constant term, hereby denoted the reduction rate (α). This constant can be calculated as the ratio between the current-exposure time product of the full dose mammogram and the current-exposure time product of the reduced-dose mammogram. Therefore, the linearized scaled image ($Y^{L,S}(x,y)$) is given by

$$Y^{L,S}(x,y) = \alpha Y^L(x,y). \tag{4}$$

3.A.2. Noise calculation

Since clinical mammograms intrinsically contain noise, it is vital to have information about the amount of noise present in an image acquired by the particular system that will be simulated. Using a uniform image exposed with the same parameters as the clinical image, it is possible to obtain a good approximation of the noise present in the clinical exam. The second challenge is to measure the noise present in the low dose configuration. Again, this information can be extracted from a uniform image acquired at the simulated radiation dose. Due to the flat-fielding process, the noise in a mammogram

is also a function of the spatial position in the detector array. Thus, the noise must either be simulated locally or the flat-field correction must be removed. In this work, we propose a local method, which allows the simulation of flat-fielded images.

Traditionally, the expected local standard deviation of the noise to be added to the original image is calculated as follows:

$$\sigma_{sim}(x,y) = \sqrt{\sigma_{H_{sim}^L}^2(x,y) - \sigma_{H_o^{L,S}}^2(x,y)}, \tag{5}$$

where $\sigma_{sim}(x,y)$ is the expected local standard deviation of the noise, $\sigma_{H_{sim}^L}^2(x,y)$ and $\sigma_{H_o^{L,S}}^2(x,y)$ are the variance masks calculated locally using a square window that runs through H_{sim}^L and $H_o^{L,S}$, respectively. To create the noise mask, an array of randomly generated Gaussian noise with zero mean and unity variance, the same size as the clinical image, is multiplied by the standard deviation calculated using Eq. (5). Next, the noise mask is added to the scaled clinical mammogram $Y_o^{L,S}$.

There are two problems associated with this simple way to incorporate the noise. First, the quantum noise present in digital mammograms is signal-dependent, i.e., its local variance depends on the local mean of the signal. The noise calculated above is not dependent on the signal found in the clinical image, thus a dependency must be created before adding them together. Second, quantum noise cannot be described as a uniform additive fraction of the signal.

The following is a new approach for creating signal-dependent noise that is additive to the signal. Figure 5 shows an overview of this noise creation process, in which the

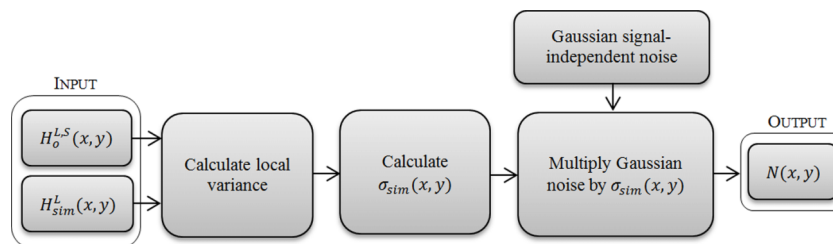


FIG. 5. Overview of the noise creation process where $H_o^{L,S}(x,y)$ is the uniform image acquired with full dose after linearization and scaling; $H_{sim}^L(x,y)$ is the uniform image acquired with the simulated dose after linearization and $\sigma_{sim}(x,y)$ is the standard deviation mask as calculated from Eq. (5). $N(x,y)$ is the noise mask with the local variance modulated by $\sigma_{sim}(x,y)$.

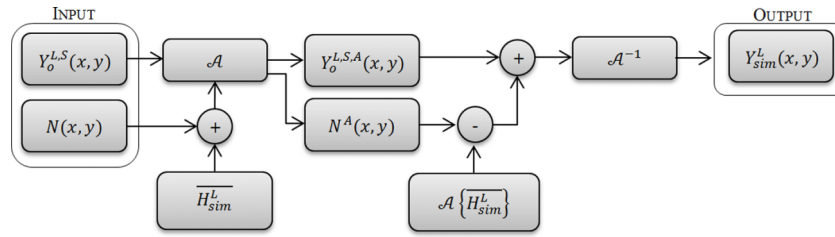


Fig. 6. Novel method for creating dependency between noise and signal, where $Y_o^{L,S}(x,y)$ is the clinical mammogram acquired with full dose after linearization and scaling process, $N(x,y)$ is the noise mask calculated previously, $\overline{H_{sim}^L}$ is the mean pixel value of the uniform image acquired with the simulated dose.

Anscombe transformation is used to incorporate the calculated noise to the clinical image.

3.A.3. Signal-dependency and additivity

When the Anscombe transformation is applied to a signal, Poisson noise is converted to additive signal-independent noise.¹⁹ Therefore, once in the Anscombe domain, the noise mask can be correctly added to the signal. After applying the inverse transformation, the dependency between the noise mask and the signal is also created and the resulting image is similar to a low-dose mammogram.

The first step to add the noise mask and create the dependency between it and the scaled clinical mammogram is to apply the Anscombe transformation to both images, using Eq. (1). However, the Anscombe transformation must be applied to a signal contaminated with noise, and the noise mask calculated previously does not contain any signal.¹⁹ Therefore, to allow the correct use of the Anscombe transformation, a positive DC signal has to be added to the noise mask prior to the application of the transformation. The added signal is the mean pixel value of the uniform image acquired at the simulated dose ($\overline{H_{sim}^L}(x,y)$). Once in the Anscombe domain, it is necessary to subtract the DC component to get the noise mask. Equation (6) presents the mathematical expression for the process,

$$N^A(x,y) = \mathcal{A}\left\{N(x,y) + \overline{H_{sim}^L}\right\} - \mathcal{A}\left\{\overline{H_{sim}^L}\right\}, \tag{6}$$

where $\overline{H_{sim}^L}$ is the mean pixel value of the linearized uniform image acquired at the simulated dose, $N(x,y)$ is the noise mask calculated as shown in Fig. 5, and $N^A(x,y)$ is the noise mask in the Anscombe domain.

Next, the noise mask and the linearized scaled clinical image can be added together to generate an image with additive Gaussian noise in the Anscombe domain. This image approximates the image obtained if the Anscombe transformation was applied to a mammographic image acquired with lower-radiation dose. The next step for our method is to apply the inverse Anscombe transformation to that image in order to obtain the simulated image in the spatial domain. Figure 6 shows an overview of the process.

Finally, the last step of the method is to add the offset back to the image, to guarantee the same behavior as a clinical image, as follows:

$$Y_{sim}(x,y) = Y_{sim}^L(x,y) + \theta. \tag{7}$$

3.B. Materials

3.B.1. Images

To assess the performance of the simulation method proposed in this work, a set of FFDM images was acquired using an anthropomorphic breast phantom, prototyped by CIRS, Inc. (Reston, VA) and the University of Pennsylvania.²⁵ Four different technique factors, resulting in four different entrance doses to the phantom (6.05, 5.29, 4.53, and 3.02 mGy), were used to validate the simulation method.



Fig. 7. Slabs of the physical phantom used in this work. The arrow indicates one of the inserted microcalcification clusters.

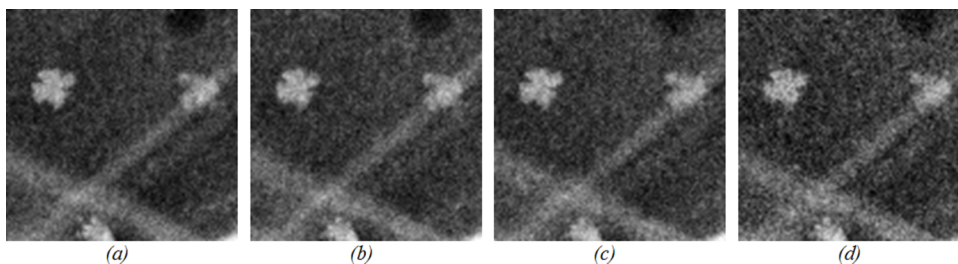


FIG. 8. Magnified region of the phantom containing a cluster of microcalcifications. (a) 6.05 mGy, (b) 5.29 mGy, (c) 4.53 mGy, and (d) 3.02 mGy.

A few reasons are presented to justify why a physical phantom was chosen to validate this work. First, the physical phantom allows repeated exposures at different radiation levels without putting a patient’s health at risk due to radiation exposure. Second, by using the physical phantom properly affixed to the breast support, it is possible to avoid any motion throughout the experiment, obviating the need for image registration. Finally, physical phantoms are subjected to an actual x-ray exposure, ensuring that every noise characteristic found in the clinical situation is found in the image of the physical phantom. By comparison, in digital phantoms, the exposure process is simulated using a mathematical model; therefore the noise behavior is simulated and might have slight differences when compared to a clinical exposure.

The breast phantom consists of six slabs, each containing simulated anatomical structures manufactured using tissue mimicking materials, based upon a realization of the companion breast software phantom.³ The phantom simulates a 450 ml breast, compressed to 5 cm, with 17% volumetric breast density (excluding the skin). In addition to the normal breast anatomy, individual pieces of calcium oxalate (99%, Alfa Aesar, Ward Hill, MA) with different sizes were placed between slabs of the phantom to mimic a cluster of microcalcifications. Figure 7 shows a photograph of all slabs of the anthropomorphic breast phantom used in this study.

A set of phantom images was acquired using a clinical mammography imaging system (Selenia Dimensions, Hologic, Bedford, MA) at the hospital of the University of Pennsylvania. First, we acquired one FFDM image of the phantom using the automatic exposure control (AEC) mode of the clinical machine. Then, we switched to the manual mode and acquired four sets of images, containing five images each, using the same kVp and target/filter combination as provided by the AEC mode but changing the exposure time in steps ranging from the original value (standard dose) to half of the standard dose. Each of these sets had a different current-exposure time resulting in different values of entrance dose to the phantom: 6.05, 5.29, 4.53, and 3.02 mGy. These doses correspond to 100%, 87.5%, 75%, and 50% of the standard dose provided by the AEC mode for this particular breast phantom. All images were acquired using the antiscatter grid. Figure 8 shows one magnified region containing a cluster of microcalcifications at each exposure configuration used in this work.

Each exposure configuration was repeated with a uniform phantom, i.e., a 4 cm thick acrylic block commonly used for flat-fielding the mammography system. Two uniform

images were acquired for each combination of exposure parameters.

3.B.2. Metrics

The metrics used to compare the real and simulated images were chosen taking into account two characteristics of the image: spatial distribution and power spectrum (PS). Since noise depends on the position of the pixel in the field, these metrics were calculated locally inside a 14.3 × 3.8 cm (2048 × 512 pixels) ROI containing the breast to avoid false statistics from the background. A regular nonoverlapping square mask with 64 × 64 pixels (0.45 × 0.45 cm) was used to calculate the variance from both simulated and real images. The center of the mask was shifted by 64 pixels before calculating each value; therefore, the total number of samples was 256. Each point was plotted in a graph to allow visual comparison of the results. Relative error was calculated to quantify similarity between images and the average difference was reported along with the 95% confidence interval (C.I.).

The normalized noise power spectrum (NNPS) was used to analyze noise in the frequency domain. This metric is a normalized form of the noise power spectrum, defined as follows:¹⁶

$$NPS(u,v) = \lim_{N_x, N_y, M \rightarrow \infty} \left(\frac{N_x N_y \Delta x \Delta y}{M} \right) \times \sum_{m=1}^M |\mathcal{F} \{I_m(x,y) - S_m(x,y)\}|^2, \tag{8}$$

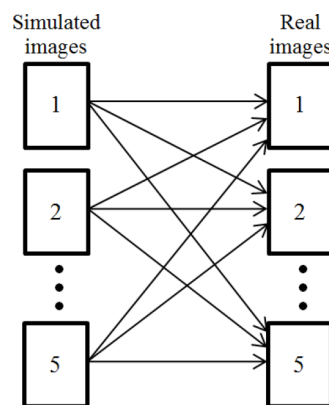


FIG. 9. Method used for crossed comparison between simulated and real images.

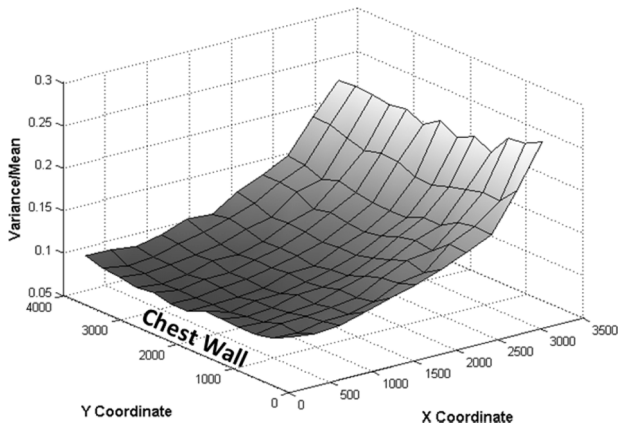


FIG. 10. Relation between variance and mean throughout the x-ray field.

where N_x and N_y are the ROI dimensions, Δx and Δy are the pixel dimensions in the x and y directions, respectively, $S(x, y)$ is an approximation of the noiseless signal, M is the total number of ROI's used, and \mathcal{F} indicates the Fourier transform. The normalization is performed by dividing the spectra by the square of the large area signal, as defined by the following:¹⁶

$$NNPS(u, v) = \frac{NPS(u, v)}{L^2}, \tag{9}$$

where L is the large area signal of the region. The NNPS was calculated using uniform images, where there is no information about the breast texture complexity. We also calculated the normalized PS.

The 1D spectrum was calculated¹⁶ and plotted for each dose reduction to allow visual evaluation of the similarity between simulated and real images. The mean and the standard deviation of the difference between the spectra of the simulated and real images were calculated. This calculation was restricted to 1.5–7.1 mm^{-1} , where the spectra did not show strong frequency dependence. The average of the difference

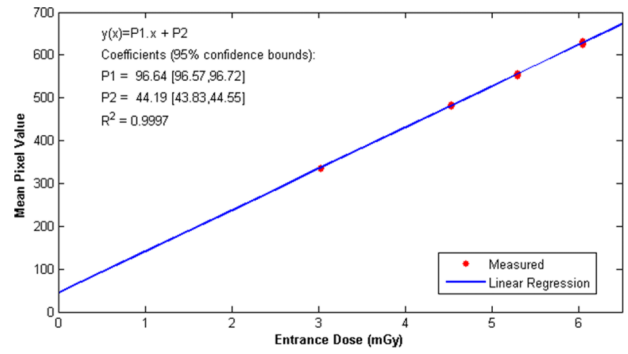


FIG. 11. Linear regression of the relation between mean pixel value and entrance dose to the phantom. The linear coefficient is important for the linearization process.

was calculated and presented along with the 95% confidence interval. Relative error was also reported.

Comparisons between simulated and real image sets were performed using the method shown in Fig. 9 in which each simulated image is compared to each real image, generating more statistically relevant data.

4. RESULTS

4.A. Preliminary noise analysis

Preliminary investigation of the noise was performed using uniform images. The graph shown in Fig. 10 shows the ratio between local noise variance and local mean pixel value.

Equation (3) indicates that a uniform image contaminated by Poisson noise would have a constant relation equal to one. However, in Fig. 10, the ratio between noise variance and mean pixel value ranges from 0.1 to 0.3, depending on the position in the field. This spatial dependence is a result of the flat-field correction performed during the system calibration, which corrects for the heel effect and x-ray oblique incidence.

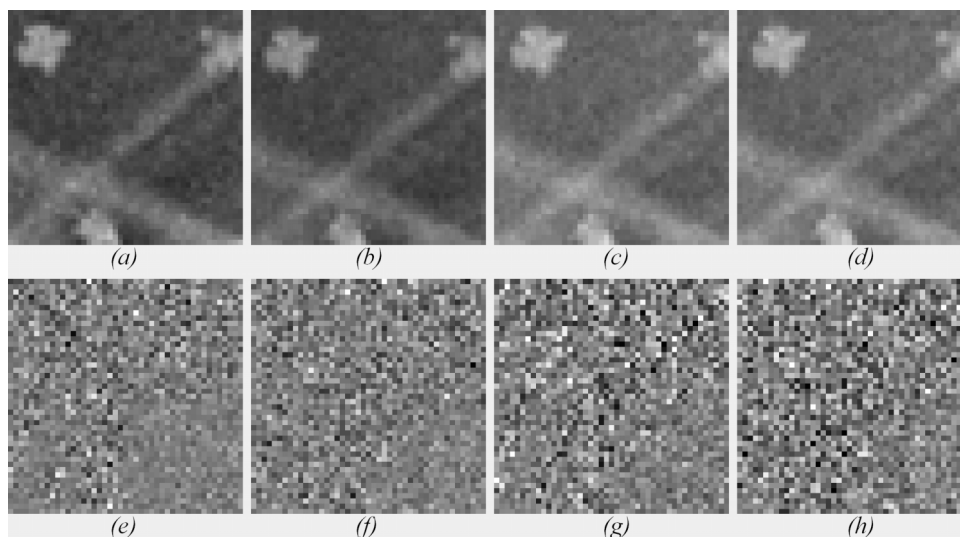


FIG. 12. Top-row: magnified view of a region of interest extracted from (a) real image acquired with 5.29 mGy. (b) Simulated image (5.29 mGy). (c) Real image acquired with 3.02 mGy. (d) Simulated image (3.02 mGy). Bottom-row: residual noise calculated for (e) real image acquired with 5.29 mGy. (f) Simulated image (5.29 mGy). (g) Real image acquired with 3.02 mGy. (h) Simulated image (3.02 mGy).

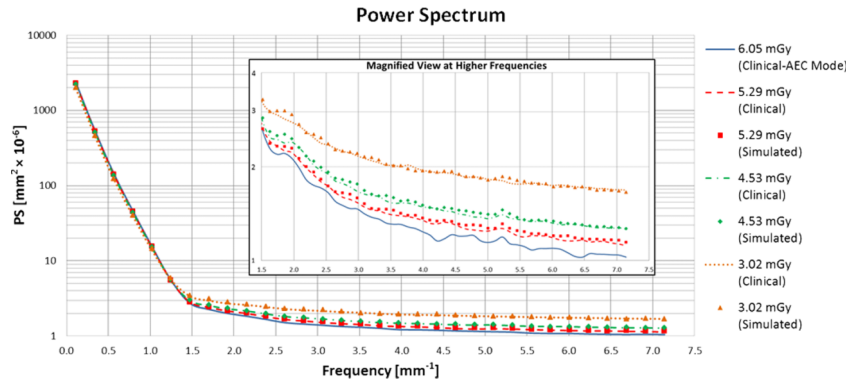


FIG. 13. Normalized PS for real and simulated images acquired with different radiation doses. In detail: magnified view of the high frequencies of the spectrum.

Figure 10 shows the importance of using a dose reduction method that is locally adaptive.

4.B. Photodetector offset

The first step in evaluating the new method was calculating the photodetector offset. To calculate the value, four different doses were used and the relation between mean pixel value and entrance dose to the phantom was represented by linear regression. The uniform images were acquired imaging a 4 cm uniform PMMA block at four different exposure configurations, all of them acquired with 29 kVp, with tungsten anode filtered with rhodium. The current–time parameter was initially set to 160 mAs, followed by 140, 120, and 80 mAs. Two images were acquired at each dose.

To calculate the linear regression, the mean pixel value was calculated in 207 different regions of the uniform images using a 64×64 pixels window, totaling 1656 measured points. Figure 11 shows the results.

The offset for the machine used in this study is approximately 44. Although the manufacturer of the mammographic unit estimates the offset to be 50,²⁶ this value was measured experimentally to guarantee the correct linearity of the images, as in our experience, this value can encompass small nonlinearities found with various imaging systems.

4.C. Method evaluation

4.C.1. Physical phantom

Examples of simulated and real images of the physical phantom are shown in Fig. 12. It shows a magnified view of a region of interest extracted from real and simulated images at two radiation doses: 5.29 and 3.02 mGy. The magnified view allows better visualization of the noise in each image. Along with the ROIs are the residual noise masks calculated by subtracting the noiseless approximation of the signal from each image. The “noiseless” signal was approximated by averaging five realizations for each dose.

Visual analysis of Fig. 12 provides evidence that the simulated and real images are very similar. However, it is

important to use appropriate metrics to evaluate the proposed method objectively. Local metrics such as variance are not a good measurement of similarity when comparing x-ray images with distinct noise power spectra.¹⁸ Thus, NNPS and PS are used to evaluate the simulation method.

Figure 13 provides a comparison between PS at different doses for clinical and simulated images. We performed crossed comparisons between real and simulated images. In Table II, values are reported after calculating the absolute percent error between the simulated and real images at each frequency and averaging them. In addition, it shows the average difference between simulated and real PS and its 95% confidence interval. For the PS, a regular nonoverlapping 0.90×0.90 cm window was used, resulting in 1600 comparisons per dose, 4800 in total.

The averaged error for the PS is less than 2.5%. The confidence interval of the average difference does not span zero, indicating that there is a bias in the PS; however, the average difference is 100 times smaller than the average signal, showing that the bias is small.

Using the same 0.45×0.45 cm window, we calculated the local variance from both simulated and real images and plotted the different regions in the graph shown in Fig. 14 (as explained in Sec. 3.B.2). Similarly to the previous image, in Fig. 14 lines represent clinical images acquired at different doses while markers identify simulated images. Each point is the average of five different realizations.

TABLE II. Comparison between PS and variance for the simulated and real images acquired at three different doses, average difference between variables, and 95% C.I. of the difference.

Radiation dose	Calculated metrics	Average error (%)	Average difference [95% C.I.]
5.29 mGy	PS	2.47 ± 1.78	0.28 [0.26 0.29] × 10 ⁻⁷
	Variance	0.81 ± 0.66	0.28 [-1.01 1.52]
4.53 mGy	PS	2.41 ± 1.88	0.32 [0.24 0.40] × 10 ⁻⁷
	Variance	0.85 ± 0.70	1.90 [-1.02 2.57]
3.02 mGy	PS	2.15 ± 1.69	0.19 [0.06 0.32] × 10 ⁻⁷
	Variance	1.00 ± 0.84	0.91 [-0.71 2.93]

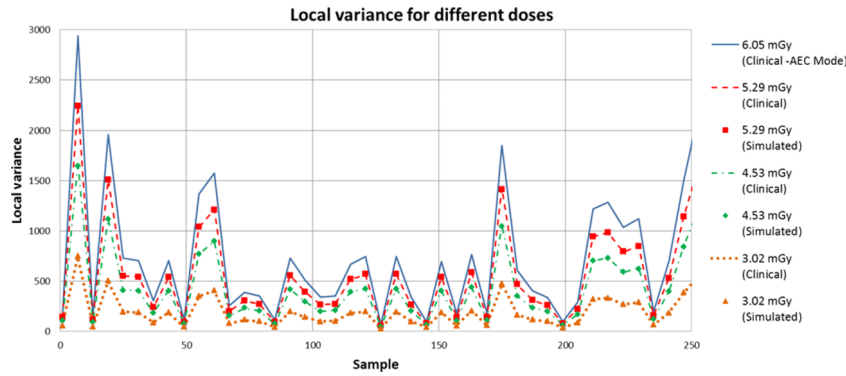


FIG. 14. Local variance for real and simulated images acquired with different radiation dose.

Again, we performed crossed comparison between clinical and simulated images. A total of 19 400 comparisons were averaged and reported at Table II, along with the average difference and the 95% confidence interval. It is important to note that averaged errors are less than 1.0% for the local variance and the confidence interval of the average difference spans zero, indicating a high correlation between simulated and real variance.

4.C.2. Uniform images

An additional study was performed using uniform images. In this section, we present the results of the simulation method applied to these uniform images, acquired using the radiograph factors described in Sec. 4.B. This analysis is important to show that the low frequency components of the spectrum are not biased by the DC component of the signal. Two images were acquired at each dose and the results of the simulation were compared using crossed comparison as presented in Sec. 3.B.2 for the physical phantom images. Figure 15 shows the NNPS of clinical and simulated uniform images at different radiation doses.

The noise insertion resulted in visually similar NNPS for each simulated dose, as seen in Fig. 15. The second metric used to compare the uniform images was the local variance. Figure 16 shows the local variance calculated using 64 × 64 pixels (0.45 × 0.45 cm) non-overlapping windows located at different positions of the field.

As expected, the noise variance increases in regions further from the chest wall. Figure 16 indicates that the simulation method was capable of approximating the local variance of a real acquisition.

Table III shows the absolute relative error calculated for the NNPS and local variance at each radiation dose when comparing simulated and real uniform images. In addition, it shows the average difference between simulated and real noise power spectra, along with the 95% C.I.

The reported averaged error was maintained lower than 3.8% for the NNPS and lower than 3.0% for the local variance, which indicates that the simulation method is capable of approximating the characteristics of real acquisitions even in uniform images, where it is possible to have a good approximation of the added noise. The confidence interval of the average difference does not span zero, indicating that there is a bias on the noise simulation. However, the values are insignificant when compared to the average signal.

5. DISCUSSION

A new method for simulating dose reduction in flat-fielded digital mammograms is proposed in this paper. The method is based on the local simulation of noise calculated using the local variance of uniform images. It can be applied to flat-fielded clinical images and accounts for the anisotropy

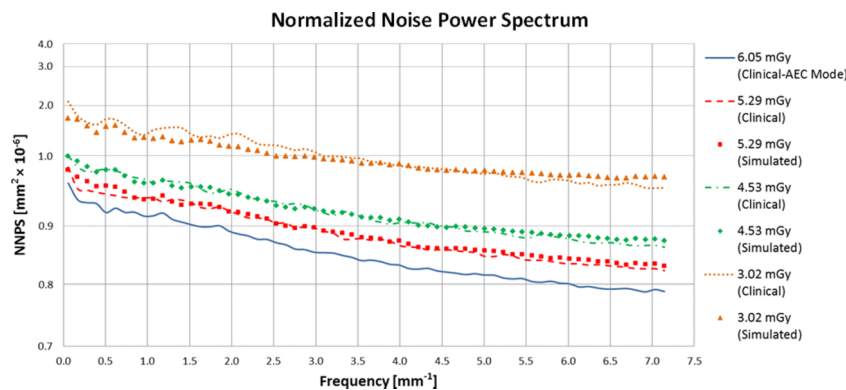


FIG. 15. Normalized noise power spectrum calculated for real and simulated uniform images at different radiation doses.

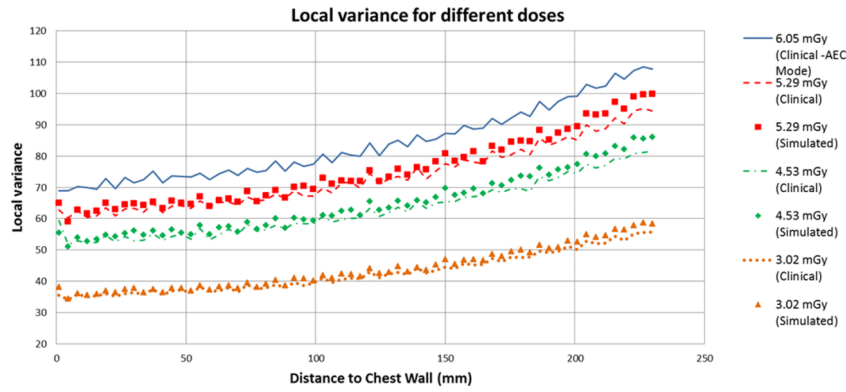


Fig. 16. Local variance calculated for real and simulated uniform images at different radiation doses.

of the noise and DQE variations. The method is based on a novel idea of inserting noise after applying a variance-stabilizing transformation (e.g., Anscombe transformation). In the variance stabilized domain, noise is independent of the mean pixel value; therefore the inserted noise mask can be modeled based only on the spatial dependency of the variance, thus accounting for the flat-field correction. In this way, the dependency between the noise mask and the pixel value is created when the inverse transformation is applied.

The proposed method accounts for the anisotropic behavior of the noise found in digital mammograms, since it uses 2D uniform images for measuring quantum noise. Also, it accounts for noise present in the input mammogram by measuring the local variance of a uniform image acquired at the same radiographic technique. No assumptions regarding the dependency between radiation dose and DQE are necessary, since noise is measured at the actual simulated dose. Furthermore, the method is capable of simulating noise locally, taking into account the spatial dependency between pixel value and variance along the field, caused by the digital mammography acquisition system. Such information is lost when only the NPS is used.

Preliminary analysis of the noise extracted from uniform images supported the development of the local simulation method proposed in this work. It is apparent from Fig. 10 that the quotients of the variance and mean pixel value have different values throughout the field; this is attributable to the pixel gain calibration that occurs during the acquisition

process and the flat-fielding. As discussed above, the simple insertion of Poisson noise into clinical images does not accurately simulate dose reduction.

It is important to note that, although the NPS is not used explicitly by the proposed method when generating the noise mask, the noise mask image is real and hence intrinsically contains noise with the correct NPS. The graph reported in Fig. 14 supports the visual verification of the correspondence between clinical and simulated images in terms of local variance. In addition, it is noticeable that lower levels of radiation produced lower local variance, which is consistent with the expected behavior from an image contaminated by quantum noise.

Some limitations and future work are now addressed. The current version of the simulation method was validated assuming that dose reduction is performed exclusively by a decrease of the current-exposure time product (mAs), following the majority of previous methods.⁶⁻¹⁰ Future work should include analysis of simulating changes to other parameters such as tube peak voltage (kVp) and the target/filter combination, as well as greater reduction in dose, such as that seen in creating tomosynthesis projection images.

The validation of this method was performed using images acquired with a-Se detectors. The validity of such method has to be tested before being applied to other detectors, such as CsI/TFT, which have significant correlated noise. The method was tested using a phantom equivalent to a 5 cm breast using a 4 cm uniform PMMA block. Further studies must be performed to analyze the influence that the thickness of the PMMA block might exert on the simulation accuracy.

Another potential application for this method is simulating various radiation dose levels in virtual clinical trials (VCTs). Further studies are needed to separate and characterize the different components of the noise; in this way, it is possible to simulate the various sources of noise separately.

TABLE III. Comparison between NNPS and variance for the simulated and real uniform images acquired at 3 different doses, average difference between variables and 95% C.I. of the difference.

Radiation dose	Calculated metrics	Average error (%)	Average difference [95% C.I.]
5.29 mGy	NNPS	2.61 ± 0.75	0.20 [0.13 0.27] × 10 ⁻⁷
	Variance	2.78 ± 0.24	2.06 [2.44 1.68]
4.53 mGy	NNPS	2.35 ± 0.50	0.07 [0.00 0.15] × 10 ⁻⁷
	Variance	2.83 ± 0.33	1.91 [2.29 1.54]
3.02 mGy	NNPS	3.79 ± 0.25	0.27 [0.05 0.48] × 10 ⁻⁷
	Variance	2.94 ± 0.25	1.37 [1.55 1.18]

6. CONCLUSION

To the best of our knowledge, this work presents the first noise insertion method for simulating dose reduction to be performed in a variance-stabilizing domain (e.g., Anscombe domain). The method developed allows the modeled noise to

account for the spatial dependency of the noise, allowing it to be applied to flat-fielded images.

ACKNOWLEDGMENTS

This work was supported by the São Paulo Research Foundation (FAPESP) Grant No. 2013/18915-5, by the Brazilian Foundation for the Coordination of Improvement of Higher Education Personnel (CAPES) Grant No. 88881.030443/2013-01 and by the US National Institutes of Health (NIH): R01 Grant No. CA154444. The content is solely the responsibility of the authors and does not necessarily represent the official views of NIH, CAPES, or FAPESP.

CONFLICT OF INTEREST DISCLOSURE

The authors have no COI to report.

^{a)} Author to whom correspondence should be addressed. Electronic mail: lucas.rodrigues.borges@usp.br

- ¹A.-K. Carton, P. Bakic, C. Ullberg, H. Derand, and A. D. A. Maidment, "Development of a physical 3D anthropomorphic breast phantom," *Med. Phys.* **38**(2), 891–896 (2011).
- ²A. Nolte, N. Kiarashi, E. Samei, W. P. Segars, and J. Y. Lo, "A second generation of physical anthropomorphic 3D breast phantoms based on human subject data," *Proc. SPIE* **9033**, 90331Y (2014).
- ³D. D. Pokrajac, A. D. A. Maidment, and P. R. Bakic, "Optimized generation of high resolution breast anthropomorphic software phantoms," *Med. Phys.* **39**(4), 2290–2301 (2012).
- ⁴K. Bliznakova, S. Suryanarayanan, A. Karellas, and N. Pallikarakis, "Evaluation of an improved algorithm for producing realistic 3D breast software phantoms: Application for mammography," *Med. Phys.* **37**(11), 5604–5617 (2010).
- ⁵N. Kiarashi, J. Y. Lo, Y. Lin, L. C. Ikejimba, S. V. Ghate, L. W. Nolte, J. T. Dobbins 3rd, W. P. Segars, and E. Samei, "Development and application of a suite of 4-D virtual breast phantoms for optimization and evaluation of breast imaging systems," *IEEE Trans. Med. Imaging* **33**(7), 1401–1409 (2014).
- ⁶R. S. Saunders and E. Samei, "A method for modifying the image quality parameters of digital radiographic images," *Med. Phys.* **30**(11), 3006–3017 (2003).
- ⁷M. Båth, M. Håkansson, A. Tingberg, and L. G. Månsson, "Method of simulating dose reduction for digital radiographic systems," *Radiat. Prot. Dosim.* **114**(1-3), 253–259 (2005).
- ⁸L. J. M. Kroft, W. J. H. Veldkamp, B. J. A. Mertens, J. P. A. Van Delft, and J. Geleijns, "Detection of simulated nodules on clinical radiographs: Dose reduction at digital posteroanterior chest radiography," *Radiology* **241**(2), 392–398 (2006).
- ⁹W. J. H. Veldkamp, L. J. M. Kroft, J. P. A. Van Delft, and J. Geleijns, "A technique for simulating the effect of dose reduction on image quality in

- digital chest radiography," *J. Digital Imaging* **22**(2), 114–125 (2009).
- ¹⁰A. Svallkvist and M. Båth, "Simulation of dose reduction in tomosynthesis," *Med. Phys.* **37**(1), 258–269 (2010).
- ¹¹A. Mackenzie, D. R. Dance, A. Workman, M. Yip, K. Wells, and K. C. Young, "Conversion of mammographic images to appear with the noise and sharpness characteristics of a different detector and x-ray system," *Med. Phys.* **39**(5), 2721–2734 (2012).
- ¹²A. Mackenzie, D. R. Dance, O. Diaz, and K. C. Young, "Image simulation and a model of noise power spectra across a range of mammographic beam qualities," *Med. Phys.* **41**(12), 121901 (14pp.) (2014).
- ¹³P. Timberg, M. Ruschin, M. Bath, B. Hemdal, I. Andersson, S. Mattsson, D. Chakraborty, R. Saunders, E. Samei, and A. Tingberg, "Potential for lower absorbed dose in digital mammography: A JAFROC experiment using clinical hybrid images with simulated dose reduction," *Proc. SPIE* **6146**, 614614 (2006).
- ¹⁴R. S. Saunders, J. A. Baker, D. M. DeLong, J. P. Johnson, and E. Samei, "Does image quality matter? Impact of resolution and noise on mammographic task performance," *Med. Phys.* **34**(10), 3971–3981 (2007).
- ¹⁵M. Ruschin, P. Timberg, M. Bath, B. Hemdal, T. Svahn, R. Saunders, E. Samei, I. Andersson, S. Mattsson, D. P. Chakraborty, and A. Tingberg, "Dose dependence of mass and microcalcification detection in digital mammography: Free response human observer studies," *Med. Phys.* **34**(2), 400–407 (2007).
- ¹⁶I. A. Cunningham, "Applied linear-systems theory," in *Handbook of Medical Imaging: Volume 1 Physics Psychophysics*, edited by J. Beutel, H. L. Kundel, and R. L. V. Metter (SPIE, Bellingham, 2000), Chap. 2, pp. 79–159.
- ¹⁷M. Yaffe, "Digital mammography," in *Handbook of Medical Imaging: Volume 1 Physics Psychophysics*, edited by J. Beutel, H. L. Kundel, and R. L. V. Metter (SPIE, Bellingham, 2000), Chap. 5, pp. 329–372.
- ¹⁸A. E. Burgess, "The Rose model, revisited," *J. Opt. Soc. Am. A* **16**(3), 633–646 (1999).
- ¹⁹F. J. Anscombe, "The transformation of Poisson, binomial and negative-binomial data," *Biometrika* **35**(3-4), 246–254 (1948).
- ²⁰M. Mäkitalo and A. Foi, "Optimal inversion of the Anscombe transformation in low-count Poisson image denoising," *IEEE Trans. Image Process.* **20**(1), 99–109 (2011).
- ²¹M. Mäkitalo and A. Foi, "Optimal inversion of the Anscombe and generalized Anscombe variance-stabilizing transformations," 2015, available at <http://www.cs.tut.fi/~foi/invausc/#ref~software>.
- ²²L. C. S. Romualdo, M. A. C. Vieira, H. Schiabel, N. D. A. Mascarenhas, and L. R. Borges, "Mammographic image denoising and enhancement using the Anscombe transformation, adaptive Wiener filtering, and the modulation transfer function," *J. Digital Imaging* **26**(2), 183–197 (2013).
- ²³N. D. A. Mascarenhas, C. A. N. Santos, and P. E. Cruvinel, "Transmission tomography under Poisson noise using the Anscombe transformation and Wiener filtering of the projections," *Nucl. Instrum. Methods Phys. Res., Sect. A* **423**(2), 265–271 (1999).
- ²⁴F. A. Haight, "Handbook of the Poisson distribution," *J. Oper. Res. Soc.* **18**(4), 478–479 (1967).
- ²⁵L. Cockmartin, P. R. Bakic, H. Bosmans, A. D. A. Maidment, H. Gall, M. Zerhouni, and N. W. Marshall, "Power spectrum analysis of an anthropomorphic breast phantom compared to patient data in 2D digital mammography and breast tomosynthesis," in *Proceedings of IWDM* (Springer International Publishing, Gifu City, Japan, 2014), Vol. 8539, pp. 423–429.
- ²⁶K. C. Young and J. M. Oduko, "Technical evaluation of the Hologic Selenia full field digital mammography system with a tungsten tube," NHSBSP Equipment Report 0801, 2008.

Paper 2: Simulation of dose reduction in digital breast tomosynthesis

This article is a personal copy of the work published by Springer Nature. If interested in reprinting/republishing this work, please access http://dx.doi.org/10.1007/978-3-319-41546-8_43

Simulation of Dose Reduction in Digital Breast Tomosynthesis

Lucas R. Borges^{1,2}, Igor Guerrero¹, Predrag R. Bakic², Andrew D. A. Maidment²,
Homero Schiabel¹ and Marcelo A. C. Vieira¹

¹University of São Paulo, Department of Electrical Engineering, São Carlos, Brazil
{lucas.rodriques.borges, igor.guerrero}@usp.br
{mvieira, homero}@sc.usp.br

²University of Pennsylvania, Department of Radiology, Philadelphia, USA
{Predrag.Bakic, Andrew.Maidment}@uphs.upenn.edu

Abstract. Clinical evaluation of dose reduction studies in x-ray breast imaging is problematic because it is difficult to justify imaging the same patient at a variety of radiation doses. One common alternative is to use simulation algorithms to manipulate a standard-dose exam to mimic reduced doses. Although there are several dose-reduction simulation methods for full-field digital mammography, the availability of similar methods for digital breast tomosynthesis (DBT) is limited. This work proposes a method for simulating dose reductions in DBT, based on the insertion of noise in a variance-stabilized domain. The proposed method has the advantage of performing signal-dependent noise injection without knowledge of the noiseless signal. We compared clinical low-dose DBT projections and reconstructed slices to simulated ones by means of power spectra, mean pixel values, and local standard deviations. The results of our simulations demonstrate low error (< 5%) between real and simulated images.

Keywords: Noise simulation · dose reduction · digital breast tomosynthesis · Anscombe transformation

1 Introduction

The ultimate study of radiation dose reduction in medical x-ray imaging requires images from the same patient at different radiation doses. In practice, such images cannot be obtained because of radiation risks. One way to overcome this limitation is to use anthropomorphic phantoms; phantom images can be acquired at various conditions without concern. However, physical phantoms do not simulate a sufficiently wide variety of breasts, which may negatively influence studies of radiologists' performance [1]. Another common approach is to manipulate standard dose images to exhibit the noise properties of an image acquired at lower radiation dose. In medical x-ray imaging, several methods have been proposed to simulate dose reduction [2-9]. However, the applicability of such methods to simulate dose reduction in digital breast tomosynthesis (DBT) is unknown.

Recently, we proposed a novel method of simulating dose reduction in full field digital mammography (FFDM) [9], based on noise insertion in a variance-stabilized domain, where no approximation of the noiseless signal is necessary. The method can be applied to flat fielded images. In this work, we evaluate our method to manipulate standard-dose DBT projections to mimic the noise characteristics of reduced-dose DBT projections.

2 Method

The proposed method for simulating dose reduction in DBT projections requires three sets of projection images as input: the standard-dose clinical exam and two uniform images at different doses. The two uniform images must be acquired using a uniform PMMA block, corresponding to the same kV and filtration as the clinical image. One uniform acquisition must be performed using the same exposure (mAs) as the standard-dose image; the other uniform image must be acquired using a reduced exposure time for the desired dose reduction. The three sets of images are used to generate simulated projections, which are then reconstructed to produce the reduced-dose DBT slices. Fig. 1 presents the workflow used in this method.

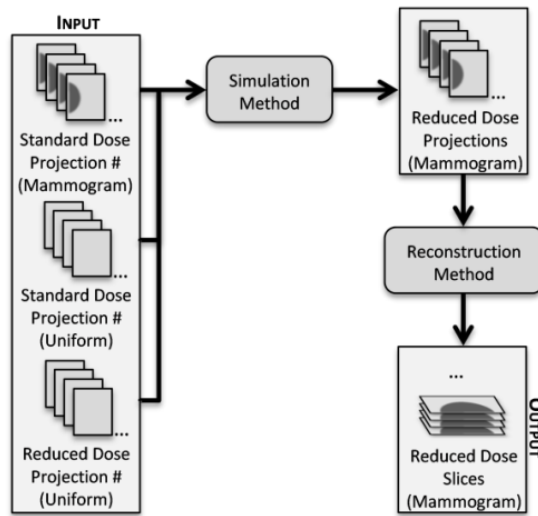


Fig. 1. Schematic of the simulation process adopted in this work.

The first stage of the simulation algorithm consists of linearizing all input images with respect to the entrance dose to the detector, and scaling the signal to the desired range. Since in this work we only consider reductions in exposure, scaling can be done simply by multiplying the original projections by the dose reduction factor (e.g., 0.7 for simulating 70% of the dose).

The second stage of the simulation method is the noise injection. To calculate how much noise should be added to the scaled image to mimic the noise at the reduced dose, we estimate the local standard deviation on both uniform images. The difference between these estimates is then used to modulate a mask of Gaussian noise with zero mean and unity variance.

The final step is to incorporate this noise mask to the scaled image. Since the added noise must be signal-dependent, its standard deviation depends on the underlying noiseless signal. To avoid making approximations of the signal, we perform the noise insertion in a variance-stabilized domain, the Anscombe domain, where no previous knowledge of the underlying signal is necessary. Importantly, the standard deviation mask calculated previously accounts for trends in the noise statistics caused by corrections such as the flat fielding. A detailed methodology is given in [9].

3 Materials

In this work we used a clinical Selenia Dimensions system (Hologic, Bedford, MA), at the Hospital of the University of Pennsylvania to assess the performance of the simulation method. Sets of DBT images were acquired using a physical anthropomorphic breast phantom, manufactured by CIRS, Inc. (Reston, VA) under license from the University of Pennsylvania [10]. The breast phantom consists of six slabs, each containing simulated anatomical structures manufactured using tissue mimicking materials, based upon a realization of the companion software phantom.

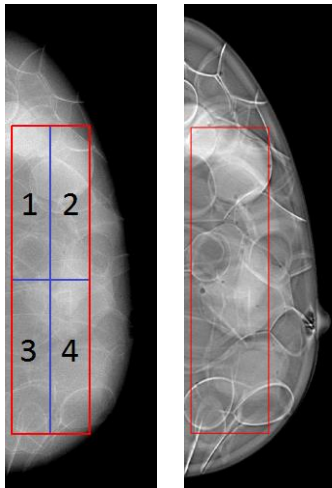


Fig. 2. Example of phantom images. Left: central raw projection. Right: central slice of the 3D reconstructed volume. The rectangles identify the ROI's used for the results.

Images were acquired using a fixed tube voltage of 31 kVp, with a tungsten target, filtered with aluminum. The exposure was decreased from 60 to 30 mAs in four steps to simulate different doses. The average incident air kerma to the phantom provided by the DICOM header for each radiographic setting was: 5.62 mGy, 4.78 mGy, 3.94 mGy and 2.81 mGy. Five acquisitions were performed for each configuration, resulting in 300 phantom projections (a set of 15 projections for each acquisition). Fig. 2 shows examples of a central projection before reconstruction and a central slice of the reconstructed 3D volume.

Each exposure configuration was repeated to image a uniform 4 cm thick PMMA block, commonly used for flat-field correction. Two acquisitions were performed for each exposure configuration, resulting in 120 uniform projections.

Real and simulated projections were reconstructed using the Briona reconstruction software (Real Time Tomography, Villanova, PA). Each

volume was generated using 1mm spacing, resulting in 2040 DBT slices, 1020 of them real and 1020 simulated.

To assess the simulation method we analysed images both before and after reconstruction. For the projections prior to reconstruction, three metrics were used: power spectrum (PS), local mean, and local standard deviation. The PS was calculated as the average PS of non-overlapping 64×64 regions within a $14.3 \text{ cm} \times 3.5 \text{ cm}$ (1024×256 pixels) ROI containing as much breast tissue as possible, as shown by the red rectangle in Fig. 2. The spatial dependence of the PS was explored by repeating the calculations in the four non-overlapping quadrants inside the ROI, as defined by the blue lines in Fig. 2. Spatial metrics, including the mean and standard deviation were calculated inside the large ROI using 256 non-overlapping $0.45 \text{ cm} \times 0.45 \text{ cm}$ (32×32 pixels) windows. After reconstruction of the 3D volume, we analysed mean and standard deviation of each slice, using an ROI of the same size and position as above.

The average absolute error between each simulated image and the corresponding real image was calculated for each metric at each simulated dose. The results reported are the crossed comparison between all five real and five simulated images, resulting in 25 comparisons for each metric at each dose.

4 Results

After the simulation method was applied to the DBT projections, we reconstructed the 3D volume and performed tests on both raw projections and processed slices. Fig. 3 shows examples of simulated and real images.

The first metric analysed was the global PS, calculated inside the entire ROI taken from the central projection. In Fig. 4 (a) it is possible to evaluate the similarity between the PS of the real and the simulated images acquired using three different doses. Fig. 4 (b) shows the average error between simulated and real images.

The PS was also calculated locally in four quadrants of the global ROI. This metric allows the evaluation of the spectrum of the simulated noise in different regions of the breast. Fig. 4 (c) shows the average absolute er-

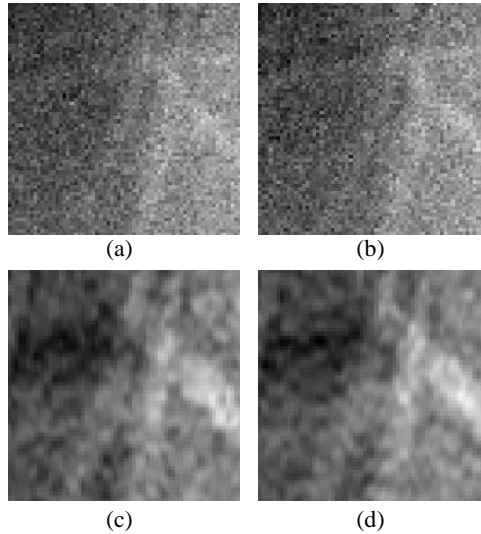


Fig. 3. Examples of real and simulated images (2.81 mGy, 50% dose). (a) Real central projection, (b) Simulated central projection, (c) Real central slice, (d) Simulated central slice.

ror at each quadrant. Note that the region used to calculate the PS on Fig. 4 (c) is different in size to that used in Fig. 4 (a-b); therefore, the spectral resolution differs in the two experiments.

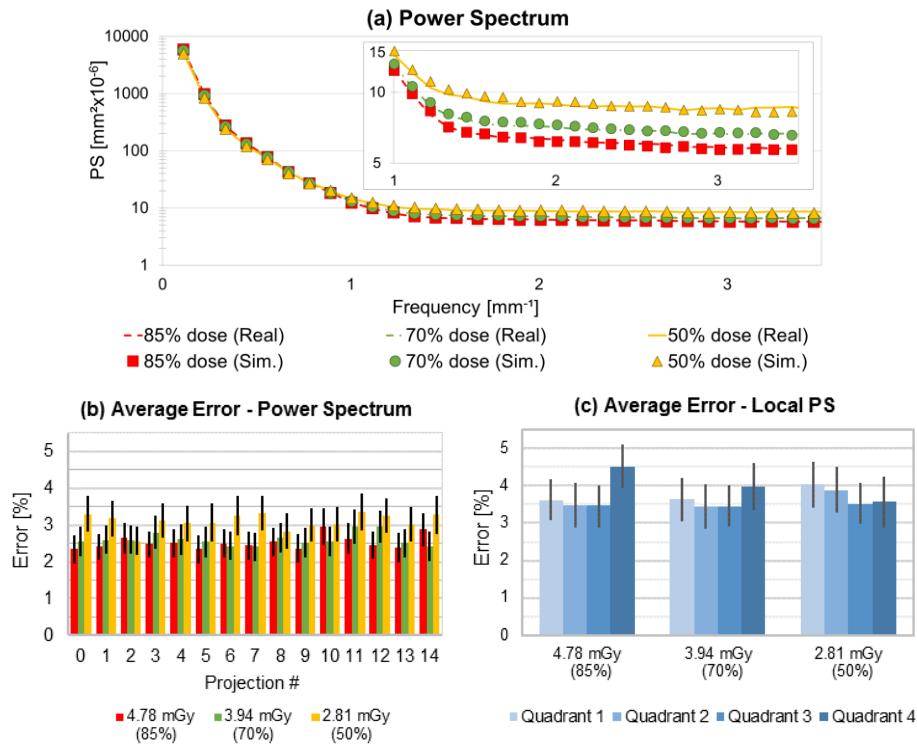


Fig. 4. Power spectra calculated from real and simulated central projections at different entrance doses to the phantom. (a) entire spectra and high frequencies in detail, (b) average absolute error for each projection, (c) average absolute error for each quadrant. Error bars are the standard error.

In the next experiment, we calculated the mean pixel value at each radiation dose and each projection before reconstruction. Fig. 5 (a) shows one example of the mean pixel value calculated at the central projection. Fig. 5 (b) is the average absolute error for each projection. Although we calculated the mean pixel value at 256 different ROIs as described in the methods section, we performed down sampling to allow better visualization of the data in Fig. 5 (a); however, the errors calculated in Fig. 5 (b) account for all 256 samples.

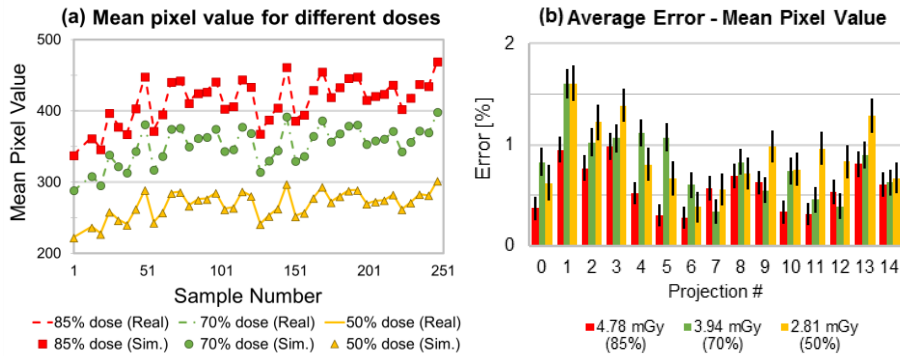


Fig. 5. Comparison between real and simulated mean pixel value at various doses to the phantom. (a) Example of the mean pixel value calculated in a central projection. (b) Average absolute error for each projection. Error bars represent the standard error.

The last metric calculated on the DBT projections was the standard deviation. Similar to previous results, we give an example of the standard deviation calculated on the central slice in Fig. 6 (a), and the average absolute error is reported in Fig. 6 (b). Again, we performed down sampling to allow better visualization of Fig. 6 (a), but the error reported in Fig. 6 (b) accounts for all 256 samples.

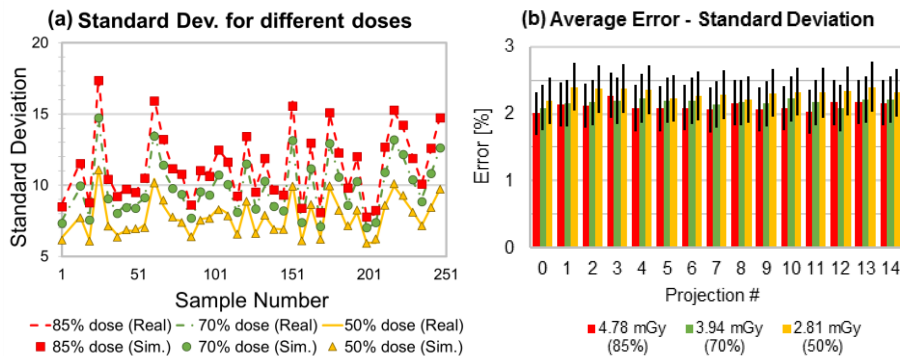


Fig. 6. Comparison between real and simulated standard deviation at various doses to the phantom. (a) Example of the standard deviation calculated in a central projection. (b) Average absolute error for each projection. Error bars represent the standard error.

Additional tests were performed on the reconstructed slices of the 3D volume. Fig. 7 (a) shows the average absolute error between the mean pixel value of the simulated and real reconstructed slices. Fig. 7 (b) shows the equivalent calculation for the standard deviation.

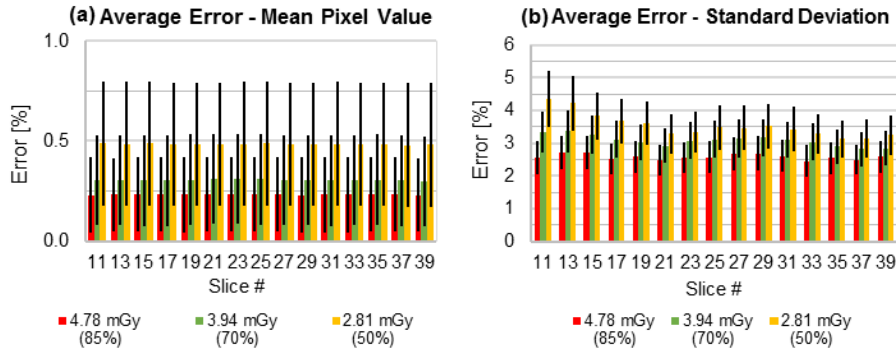


Fig. 7. Local metrics calculated from real and simulated slices at various doses to the phantom: (a) average absolute error of the mean pixel value, (b) average absolute error of the standard deviation.

5 Discussion and Conclusions

In this work, we propose a new method for simulating dose reduction in DBT images. A number of existing dose-reduction simulation methods [2-6,9] are based on a two-step approach: signal scaling, and noise insertion. Adding signal dependent noise to an already noisy image is a challenging task, since the noise statistics depend on the noiseless underlying signal, which is not available in most clinical cases. With the proposed method, noise insertion is performed in a variance-stabilized domain, where no knowledge of the noiseless signal is necessary. Furthermore, the method simulates noise locally; therefore, it can be applied to flat-fielded images and reproduce statistical trends, such as those generated by the heel effect.

A preliminary assessment was performed on the projection images and on the reconstructed slices. Power spectral analysis demonstrated that the noise was correctly simulated in terms of spatial frequency, with average absolute error below 3.5% for every projection, as shown in Fig. 4 (b). The average absolute error of the local power spectra reported on Fig. 4 (c) shows the simulation could replicate the global and local dependencies of the clinical PS. As seen in Fig. 5 and Fig. 6, the local spatial statistics on raw projections also show small errors ($< 2.5\%$) for every image.

The final experiment was performed on reconstructed slices. Fig. 7 shows that the pixel values of the reconstruction images were very similar to the real reconstruction images, with errors below 0.5%, and the standard deviation showed errors below 4.5%. It is interesting to notice that in Fig. 7 (a), that although the errors are extremely low, it is possible to notice a trend in the results, with higher dose reductions resulting in higher errors. Furthermore, Fig. 7 (b) shows that the noise was simulated with higher precision in slices farther from the detector plate. Further tests are necessary to understand this behaviour.

Some limitations and future work are now addressed. In this work, we used a clinical unit with an amorphous-selenium (a-Se) detector with minimally correlated noise. Further analysis is necessary to simulate systems with highly correlated noise. In this work,

we considered dose reductions achieved exclusively by reduction of the exposure. Further analysis is necessary for simulating changes on other radiographic factors, such as kV, target, and filtration. The PMMA blocks used for the uniform images were chosen to mimic the filtration of the breast. Future work should include analysis of the dependency between the thickness of the PMMA and the accuracy of the simulation method.

Acknowledgements. The authors would like to thank São Paulo Research Foundation (FAPESP grant# 2013/18915-5) and the Brazilian Foundation for the Coordination of Improvement of Higher Education Personnel (CAPES grant# 88881.030443/2013-01) for the financial support given to this project. The authors would also like to acknowledge the support of the National Institutes of Health/National Cancer Institute grant 1R01-CA154444. The content of this paper is solely the responsibility of the authors and does not necessarily represent the official views of the funding agencies. We thank Real Time Tomography (RTT) for providing assistance with image reconstruction. ADAM is a member of the scientific advisory board and shareholder of RTT.

References

1. Samei, E., Eyler, W., Baron, L.: Effects of anatomical structure on signal detection. Handbook of medical imaging. 655-682 (2000).
2. Saunders, R.S., Samei, E.: A method for modifying the image quality parameters of digital radiographic images. *Med. Phys.* 30, 3006–3017 (2003).
3. Båth, M., Håkansson, M., Tingberg, A., Månsson, L.G.: Method of simulating dose reduction for digital radiographic systems. *Radiat. Prot. Dosimetry.* 114, 253–259 (2005).
4. Kroft, L.J.M., Veldkamp, W.J.H., Mertens, B.J.A., Van Delft, J.P.A., Geleijns, J.: Detection of simulated nodules on clinical radiographs: dose reduction at digital posteroanterior chest radiography. *Radiology.* 241(2), 392–398 (2006).
5. Veldkamp, W.J.H., Kroft, L.J.M., Van Delft, J.P.A., Geleijns, J.: A technique for simulating the effect of dose reduction on image quality in digital chest radiography. *J. Digit. Imaging* 22(2), 114–125 (2009).
6. Svalkvist, A., Båth, M.: Simulation of dose reduction in tomosynthesis. *Med. Phys.* 37(January), 258–269 (2010).
7. Mackenzie, A., Dance, D.R., Workman, A., Yip, M., Wells, K., Young, K.C.: Conversion of mammographic images to appear with the noise and sharpness characteristics of a different detector and x-ray system. *Med. Phys.* 39, 2721 (2012).
8. Mackenzie, A., Dance, D.R., Diaz, O., Young, K.C.: Image simulation and a model of noise power spectra across a range of mammographic beam qualities. *Med. Phys.* 41, 121901-1-14 (2014).
9. Borges, L.R., Oliveira, H.C.R., Nunes, P.F., Vieira, M.A.C.: Method for inserting noise in digital mammography to simulate reduction in radiation dose. In: *Proc. SPIE 9412, Medical Imaging.* 94125J-94125J (2015).
10. Cockmartin, L., Bakic, P.R., Bosmans, H., Maidment, A.D.A., Gall, H., Zerhouni, M., Marshall, N.W.: Power spectrum analysis of an anthropomorphic breast phantom compared to patient data in 2D digital mammography and breast tomosynthesis. In: *12th Int. Work. Proc. Gifu,* 423–429 (2014)

Paper 3: Unbiased injection of signal-dependent noise in variance-stabilized range

In reference to IEEE copyrighted material which is used with permission in this thesis, the IEEE does not endorse any of University of São Paulo's products or services. Internal or personal use of this material is permitted. If interested in reprinting/republishing IEEE copyrighted material for advertising or promotional purposes or for creating new collective works for resale or redistribution, please go to http://www.ieee.org/publications_standards/publications/rights/rights_link.html to learn how to obtain a License from RightsLink.

Unbiased Injection of Signal-Dependent Noise in Variance-Stabilized Range

Lucas Rodrigues Borges, Marcelo Andrade da Costa Vieira, and Alessandro Foi

Abstract—The design, optimization, and validation of many image-processing or image-based analysis systems often require testing of the system performance over a dataset of images corrupted by noise at different signal-to-noise ratio (SNR) regimes. A noise-free ground-truth image may not be available, and different SNRs are simulated by injecting extra noise into an already noisy image. However, noise in real-world systems is typically signal dependent, with variance determined by the noise-free image. Thus, the noise to be injected shall also depend on the unknown ground-truth image. To circumvent this issue, we consider the additive injection of noise in variance-stabilized range, where no previous knowledge of the ground-truth signal is necessary. Specifically, we design a special noise-injection operator that prevents the errors on expectation and variance that would otherwise arise when standard variance-stabilizing transformations are used for this task. Thus, the proposed operator is suitable for accurately injecting signal-dependent noise, even to images acquired at very low counts.

Index Terms—Anscombe transformation, noise injection, optimization, Poisson noise, variance stabilization.

I. INTRODUCTION

MANY image-processing and image-based analysis systems are sensitive to variations on the image quality. It is imperative to understand the effect that image SNR may exert on the performance of these methods. Therefore, it is a common approach to evaluate them over sets of images corrupted by different noise levels.

For instance, the optimization of the radiation dose in X-ray systems is of great importance in medical applications. Acquiring several images of the same patient at different SNR regimes is prohibitive due to radiation-related risks. In this case, it is common to perform preclinical trials by simulating different radiation doses through injection of noise into a noisy standard-dose image [1]–[8].

In many applications, the observations are corrupted by signal-dependent nonadditive errors related to the inherent

uncertainties such as photon accumulation, which is often modeled through the Poisson distribution. The data distribution hence depends on its expectation, and simulations thus require an underlying noise-free signal, or a ground-truth image. However, this poses a challenge, as such noise-free image may not be available. One approach consists in estimating the true signal, either using local statistics from a single observation [2] or through previous modeling of the acquisition system [5]. However, estimating the underlying signal is not always feasible, since it may introduce errors due to smearing and blurring through smoothing, as pointed by the authors themselves [2], [5]. Another approach consists in creating a signal-independent noise mask with the desired noise properties and installing dependency by assuming that the observed Poisson variable is a good approximation of the true signal [1], [3], [4], [6], which provides good performance only at high-count regimes.

In previous works, we proposed the injection of additive Gaussian noise in a variance-stabilized range, resulting in an approximately Poissonian distribution in the signal range [7], [8]. In this way, no previous knowledge of the true signal is needed, and the noise injection is performed in a pixel-by-pixel manner, avoiding potential problems due to smoothing or due to inaccurate estimation of the signal. However, due to the use of generic variance-stabilizing transformations (VSTs) (ideally meant for the denoising task), the method [7], [8] is biased for small counting and performs poorly in applications in which the counting rate is reduced.

Thus, here we introduce an operator built using a pair of forward and inverse transformations jointly optimized, specifically for the noise-injection task. Such operator is capable of performing unbiased noise injection even at very low counting rates (≈ 1 count per pixel), allowing, e.g., the accurate simulation of reduced-dose X-ray images from inputs that are already in photon-limited imaging modalities. To the best of our knowledge, this is the first work that addresses this problem specifically taking into account the low-count regime, which is the most challenging case for two fundamental reasons. First, at low counts, the SNR of the input image is already very low, making it impossible to obtain a trustworthy estimate of the underlying noise-free image through denoising. Even state-of-the-art filters [9] invariably introduce smearing, blurring, or other artifacts [10], [11]. Second, variance-stabilization techniques are typically designed based on large-count asymptotics, which is well known to lead to inaccurate stabilization and bias at low counts [12], [13]. In particular, we demonstrate our methodology for the Poisson observation case, which is arguably the most challenging one, since exact variance stabilization of Poisson data is known to be fundamentally impossible to achieve [14].

Manuscript received June 25, 2016; accepted August 12, 2016. Date of publication August 19, 2016; date of current version September 8, 2016. This work was supported in part by the Academy of Finland under Project 252547, in part by the São Paulo Research Foundation (FAPESP) under Grant 2013/18915-5, and in part by the Brazilian Foundation for the Coordination of Improvement of Higher Education Personnel (CAPES) under Grant 88881.030443/2013-01. The associate editor coordinating the review of this manuscript and approving it for publication was Dr. Michael Liebling.

L. R. Borges and M. A. da Costa Vieira are with the University of São Paulo, São Paulo 13566-590, Brazil (e-mail: lucas.rodrigues.borges@usp.br; mvieira@sc.usp.br).

A. Foi is with Tampere University of Technology, Tampere 33720, Finland (e-mail: alessandro.foi@tut.fi).

This paper contains supplemental material available at <http://ieeexplore.ieee.org>. Color versions of one or more of the figures in this paper are available online at <http://ieeexplore.ieee.org>.

Digital Object Identifier 10.1109/LSP.2016.2601689

II. PRELIMINARIES

A. Poisson Observation Model and Problem Formulation

Consider $\hat{z}_i, i = 1, 2, \dots, N$ as the acquired pixels forming an image \hat{z} . We model each \hat{z}_i as an independent scaled Poisson random variable with underlying signal $y_i \geq 0$ as given below:

$$\hat{z}_i = \hat{\pi}_i / \hat{\lambda} \quad \hat{\pi}_i \sim \mathcal{P}(\hat{\lambda} y_i) \quad (1)$$

where $E\{\hat{z}_i|y_i\} = y_i$, $\text{var}\{\hat{z}_i|y_i\} = y_i/\hat{\lambda}$, and $\hat{\lambda} > 0$ is a scaling factor that controls the relative noise strength.

Our goal is to obtain from \hat{z}_i a new set of *noisier* scaled Poisson observations z_i with a smaller scaling factor $\lambda < \hat{\lambda}$:

$$z_i = \pi_i / \lambda \quad \pi_i \sim \mathcal{P}(\lambda y_i). \quad (2)$$

Thus, z_i has the same mean as \hat{z}_i but a larger standard deviation:

$$E\{z_i|y_i\} = y_i = E\{\hat{z}_i|y_i\}, \quad \text{std}\{z_i|y_i\} = \sqrt{\frac{y_i}{\lambda}} = \frac{\text{std}\{\hat{z}_i|y_i\}}{\sqrt{\lambda/\hat{\lambda}}}. \quad (3)$$

A definition such as (2) assumes knowledge of the noise-free y_i , which means that obtaining z_i from \hat{z}_i may be possible only subject to certain approximations. Pragmatically, we formulate an optimization problem in which the sought solution is a non-negative $z_i \geq 0$ that solves (3) in a least-squares sense.

B. Variance-Stabilizing Transformation

VSTs are commonly applied to cease the dependency between the noise-free signal and the noise variance, allowing, e.g., suppression of signal-dependent noise through many off-the-shelf filters for additive models [13]. The typical VST for Poisson data is the Anscombe transformation, which for observations (1) takes the form

$$a_{\hat{\lambda}}(\hat{z}_i) = 2\sqrt{\hat{\lambda}\hat{z}_i + \frac{3}{8}} \quad (4)$$

yielding stabilized variables that can be treated as normal with unit variance: $a_{\hat{\lambda}}(\hat{z}_i) \sim \mathcal{N}(a_{\hat{\lambda}}(y_i) + 1/8, 1)$ [15].

III. NOISE INJECTION

A. Definition

Let f be the VST for \hat{z} . We consider addition of further noise to the stabilized $f(\hat{z})$, and hence we aim at constructing an operator $\Phi_{\lambda, \hat{\lambda}}$ of the form

$$z_i = \Phi_{\lambda, \hat{\lambda}}(\hat{z}_i) = g(f(\hat{z}_i) + \sigma n_i) \quad (5)$$

where $n_i \sim \mathcal{N}(0, 1)$ and $\sigma \geq 0$ so that $\Phi_{\lambda, \hat{\lambda}}(\hat{z}_i)$ satisfies (3). For instance, as demonstrated in the online supplementary material, a tedious but otherwise simple analysis based on mixtures of noncentral χ^2 distributions shows that setting

$$f = a_{\hat{\lambda}}, \quad \sigma^2 = \frac{\hat{\lambda}}{\lambda} - 1, \quad g(x) = \frac{1}{4\hat{\lambda}} \left(x^2 - \frac{3}{2} - \sigma^2 \right) \quad (6)$$

yields

$$E\left\{\Phi_{\lambda, \hat{\lambda}}(\hat{z}_i) | y_i\right\} = y_i \quad (7)$$

$$\text{var}\left\{\Phi_{\lambda, \hat{\lambda}}(\hat{z}_i) | y_i\right\} = \frac{y_i}{\lambda} + \frac{\hat{\lambda}^2 + \hat{\lambda}\lambda - 2\lambda^2}{8\hat{\lambda}^2\lambda^2}. \quad (8)$$

We wish to emphasize that the equalities (7) and (8) are not based on asymptotics or other approximations and are thus precise for any combination of $y_i \geq 0$ and $\hat{\lambda} \geq \lambda \geq 0$. In particular, (7) shows that (5) and (6) solve the left-hand side of (3) exactly for any $y \geq 0$. When this happens, we say that $\Phi_{\lambda, \hat{\lambda}}$ performs an (exact) *unbiased noise injection in variance-stabilized range*. Equation (8) shows that the right-hand side of (3) is solved only approximately, with good relative accuracy for large y . However, this approximation of the desired variance may be rather coarse for small λ or small y . Moreover, (6) does not account for the nonnegativity requirement, yielding variables that can be as low as $g(0) < 0$. The clipped $\Phi_{\lambda, \hat{\lambda}}^+(\hat{z}) = \max\{0, \Phi_{\lambda, \hat{\lambda}}(\hat{z})\}$ ensures nonnegativity, but impacts both (7) and (8), particularly at low count rates [16]. Fig. 1 (left) illustrates how the expectation and standard deviation of $\Phi_{\lambda, \hat{\lambda}}^+(\hat{z})$ differ from the goal (3) at low counts. Let us note that (6) is *per se* already an improvement over [7], [8], where the inverse transformation was an inverse of the Anscombe transformation designed to be unbiased *with* filtering and *without* noise injection, which led to a systematic extra positive bias ($\approx \lambda^{-1}/4$) at both large and small counts.

B. Optimization

The operator $\Phi_{\lambda, \hat{\lambda}}^+$ as defined by (6) fulfills (3) asymptotically. To improve the operator at low counts, we define a practical optimization task. Following [17], we model f and g through rational-polynomial functions as

$$f(x) = 2\sqrt{\frac{\sum_{k=0}^J p_k x^k}{\sum_{k=0}^K q_k x^k}} = 2\sqrt{\frac{P(x)}{Q(x)}} \quad (9)$$

$$g(x) = \frac{\sum_{k=0}^N r_k x^k}{\sum_{k=0}^M s_k x^k} = \frac{R(x)}{S(x)} \quad (10)$$

and optimize the coefficients of the polynomials P , Q , R , and S under the constraint that f and g approach the definitions (6) asymptotically, which ensures [18] that also (3) are attained asymptotically through (7) and (8). Thus, we require

$$\frac{P(x)}{Q(x)} - \hat{\lambda}x - \frac{3}{8} \xrightarrow{x \rightarrow +\infty} 0 \quad (11)$$

$$\frac{R(x)}{S(x)} - \frac{1}{4\hat{\lambda}} \left(x^2 - \frac{3}{2} - \sigma^2 \right) \xrightarrow{x \rightarrow +\infty} 0. \quad (12)$$

These force $K = J - 1$ and $M = N - 2$. For simplicity, we here set $J = 3$ and $N = 4$, for which (11) and (12) hold, provided

$$p_3 = \hat{\lambda}q_2, \quad q_1 = p_2 - \frac{3p_3}{8}, \quad r_4 = \frac{3 + 2\sigma^2}{\hat{\lambda}s_2}$$

$$r_3 = \frac{\hat{\lambda}s_1}{3 + 2\sigma^2}, \quad r_2 = \frac{\hat{\lambda}s_0}{3 + 2\sigma^2} - \frac{3 + 2\sigma^2}{2\hat{\lambda}}.$$

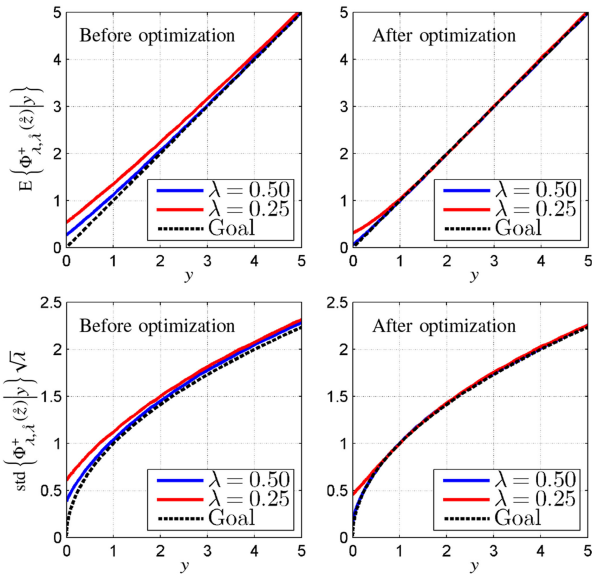


Fig. 1. Expectation and standard deviation of $\Phi_{\lambda, \hat{\lambda}}^+(\hat{z})$ before (left) and after (right) optimization ($\lambda = 0.25, 0.50, \hat{\lambda} = 1$).

We can always fix $q_0 = s_0 = 1$, hence (9) and (10) depend only on few free parameters $\Pi = [p_3 \ p_2 \ p_1 \ p_0 \ r_4 \ r_3 \ r_1 \ r_0]$, which we can vary as to minimize the discrepancy errors

$$\mathcal{E}_E(y) = E \left\{ \Phi_{\lambda, \hat{\lambda}}^+(\hat{z}) | y \right\} - y$$

$$\mathcal{E}_{\text{std}}(y) = \text{std} \left\{ \Phi_{\lambda, \hat{\lambda}}^+(\hat{z}) | y \right\} - \sqrt{\frac{y}{\hat{\lambda}}}$$

between the actual expectation and standard deviation of $\Phi_{\lambda, \hat{\lambda}}^+(\hat{z})$ and their desired values (3). In particular, we define the optimal parameters Π^* as the solution of

$$\Pi^* = \underset{\Pi}{\text{argmin}} \int_0^{+\infty} \frac{\mathcal{E}_E^2(y)}{y_\epsilon^2} + \frac{\mathcal{E}_{\text{std}}^2(y)}{y_\epsilon} dy \quad (13)$$

where $y_\epsilon = \max\{\epsilon, y\}$, $\epsilon > 0$. The integral cost (13) controls the relative quadratic errors; the integral is always finite, at $y \rightarrow 0^+$ by using a fixed positive ϵ , and at $y \rightarrow +\infty$ due to the constraints on the polynomial coefficients.

Note that $\Pi_{\text{init}} = [0 \ 0 \ 1 \ 3/8 \ 0 \ 0 \ -1/2 \ 0]$ gives exactly (6).

IV. EXPERIMENTS

To solve (13), we employ a multistart Nelder–Mead direct-search method [19], [20], with initial condition given by Π_{init} and set $\epsilon = 0.01$. Because cases with $\hat{\lambda} \neq 1$ can be treated using $\frac{1}{\hat{\lambda}} \Phi_{\lambda/\hat{\lambda}, 1}^+(\hat{\lambda} \hat{z})$, without loss of generality we always assume $\hat{\lambda} = 1$. We consider two illustrative cases $\lambda = 0.50$ and $\lambda = 0.25$, which, respectively, correspond to a half and to a quarter exposure (or dose in case of X-ray radiation). Fig. 2 shows the optimized functions f and g , where the latter is plotted as $g^+ = \max\{0, g\}$ to incorporate the nonnegativity of $\Phi_{\lambda, \hat{\lambda}}^+(\hat{z})$. Note the irregular profile, particularly for g with $\lambda = 0.50$, typical of optimized VSTs (see, e.g., [17], [21]). Fig. 1 (right) presents the expectation and standard deviation of the optimized $\Phi_{\lambda, \hat{\lambda}}^+(\hat{z})$, which approximate the goal (3) in practice

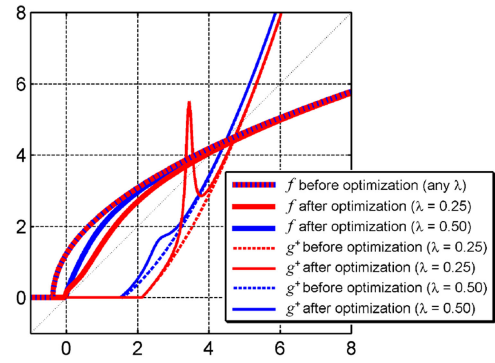


Fig. 2. Functions f and $g^+ = \max\{0, g\}$ before and after optimization of $\Phi_{\lambda, \hat{\lambda}}^+(\lambda = 0.25, 0.50, \hat{\lambda} = 1)$.

perfectly for y as low as 1. A comparison with Fig. 1 (left) demonstrates the significant improvement over the unoptimized operator (6).

In Fig. 3, we compare the cumulative distribution function and mean of z according to the ideal target Poisson distribution (2) with those obtained from $\Phi_{\lambda, \hat{\lambda}}^+(\hat{z})$ before and after optimization, for a few combinations of λ , and y . The first two subplots from the left ($\lambda = 0.50$ and $\lambda = 0.25$) show that a decrease on λ increases the error on the mean, which is corrected by the optimization. The rightmost subplot ($y = 20$) shows that the method converges for high values of the signal even before the optimization is performed.

Further, Fig. 4 demonstrates the application of the proposed approach to a low-count image \hat{z} of fluorescent cells. For this experiment, we have access to a virtually noise-free ground-truth signal y , from which we can obtain a reference ideal noisy z for $\lambda = 0.5$ according to (2), against which we can compare the other noisy images. First, we can notice the bias in the unoptimized $\Phi_{\lambda, \hat{\lambda}}^+(\hat{z})$ solution (6), particularly in the background, which is visibly brighter. It is instead difficult to detect qualitative differences between the optimized $\Phi_{\lambda, \hat{\lambda}}^+(\hat{z})$ (13) obtained from \hat{z} and the ideal z obtained from y : Despite the already low SNR of \hat{z} , many thin filament structures and localized features can be still recognized. We also wish to compare the result of our method to an image ζ , $\lambda \zeta_i \sim \mathcal{P}(\lambda \hat{y}_i)$, generated from an estimate \hat{y} of y by a state-of-the-art denoising method [9], [13] applied to \hat{z} . We can observe a loss of detail and contrast when \hat{y} is used as an approximation of y . For instance, the filament at bottom-left of the image is lost through filtering, and contours are overall less sharp in ζ than in any of the $\Phi_{\lambda, \hat{\lambda}}^+(\hat{z})$ images. We wish to emphasize that differences between ζ and z are caused *only* by the differences between \hat{y} and y , since \mathcal{P} used the same pseudorandom pattern for all images.

As a final experiment, we compare the accuracy of the proposed method to that of the direct injection of signal-dependent noise with $\pi_i \approx \mathcal{N}(\hat{z}_i \lambda, \hat{z}_i \lambda (1 - \lambda/\hat{\lambda}))$, as used by, e.g., [1], [3], [4], [6]. This normal distribution is actually an approximation of the binomial distribution $\mathcal{B}(\hat{z}_i \hat{\lambda}, \lambda/\hat{\lambda}) = \mathcal{P}(\lambda y_i)$, which, while being formally ideal, is never used directly because it does not generalize well to the nonpure Poisson scenario typical of practical applications. Similar to $\Phi_{\lambda, \hat{\lambda}}^+(\hat{z})$, also in this case we need to

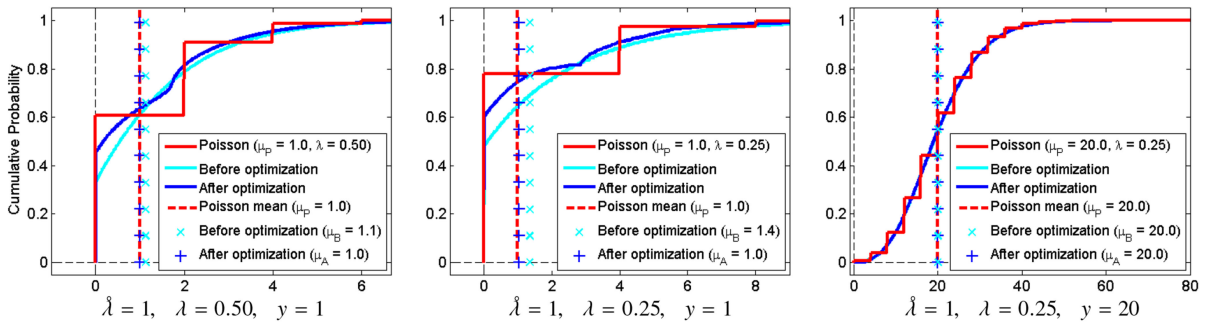


Fig. 3. Cumulative distribution function (CDF) and mean μ_P of z according to the ideal target Poisson distribution (2) versus the CDFs and means μ_B, μ_A obtained from $\Phi_{\lambda, \hat{\lambda}}^+(\hat{z})$ before optimization (6) and after optimization (13). Each subplot corresponds to different combinations of y and λ , while $\hat{\lambda} = 1$.

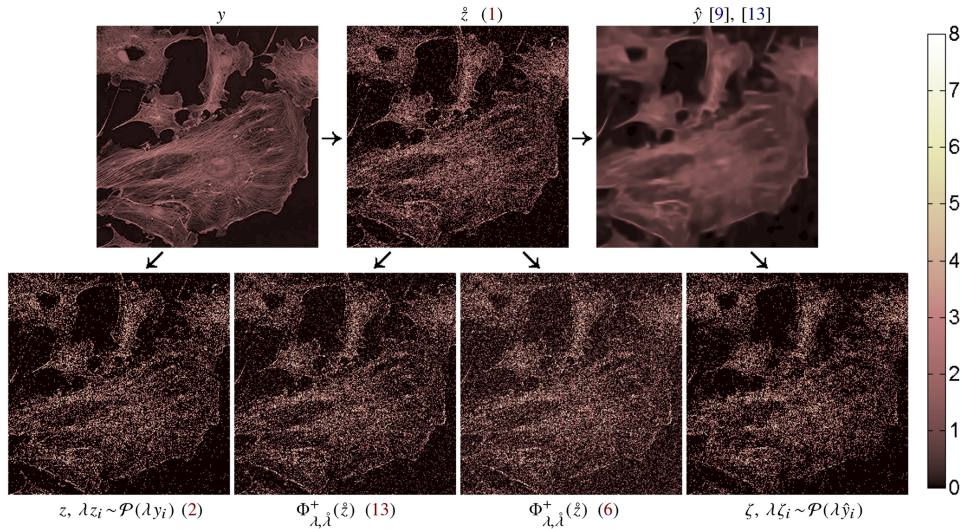


Fig. 4. Comparison of various approaches for obtaining a lower SNR image (3) from a Poisson observation \hat{z} (1), for $\lambda = 0.50, \hat{\lambda} = 1$: results by proposed noise injection before (6) and after optimization (13), Poisson ζ on a denoised estimate \hat{y} , ideal reference Poisson z (2) on noise-free ground-truth y .

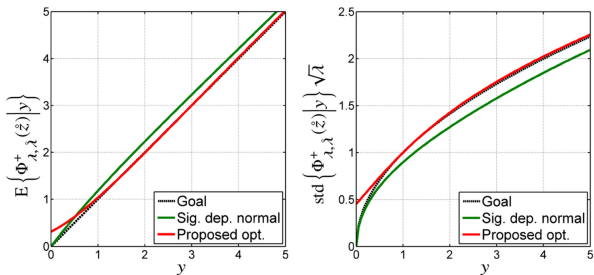


Fig. 5. Comparison of expectation and standard deviation of the random variables produced by direct injection of signal-dependent noise to the image intensities versus the proposed method of injection in variance-stabilized range with optimized transformations ($\lambda = 0.25, \hat{\lambda} = 1$).

enforce nonnegativity which similarly impacts the expectation and variance leading to unwanted bias, as illustrated in Fig. 5 for $\lambda = 0.25$. The case $\lambda = 0.50$, omitted due to space limitation, demonstrates comparably negligible expectation bias for the two methods and a minor deficiency in the directly injected variance.

V. DISCUSSION AND CONCLUSION

We have proposed an operator capable of changing the relative strength of signal-dependent noise corrupting an image. The

injection is pixelwise and is performed in a variance-stabilized range, where knowledge of the ground-truth image is unnecessary. We showed that the initial form of the operator, based on asymptotics, performs poorly at low counts, and have thus developed an optimized operator that significantly improves the results across the dynamic range. Since this approach is based on univariate mappings and on injection of spatially uncorrelated noise, the total computational cost is proportional to the number of pixels in the image. The present goal (3) and the corresponding cost (13) involve only the first two moments of z , but it is of course possible to include extra higher order moments, and employ higher order rational polynomials with $J > 3$ and $N > 4$ or other parametric families of transformations. One may naturally expect better fit by increasing the number of parameters.

In this letter, we have considered the Poisson distribution as the most challenging case. The proposed approach can be easily generalized to other distributions, and we shall consider noise injection also for Poisson–Gaussian combinations, as well as the interaction with quantization. Also, we wish to further investigate the case of spatially correlated noise. Finally, we aim to obtain a closed form of the optimized $\Phi_{\lambda, \hat{\lambda}}^+$, readily applicable to any $0 < \lambda < \hat{\lambda}$.

REFERENCES

- [1] M. Båth, M. Håkansson, A. Tingberg, and L. G. Månsson, "Method of simulating dose reduction for digital radiographic systems," *Radiation Protection Dosimetry*, vol. 114, no. 1–3, pp. 253–259, 2005. [Online]. Available: <http://dx.doi.org/10.1093/rpd/nch540>
- [2] W. J. Veldkamp, L. J. Kroft, J. P. A. van Delft, and J. Geleijns, "A technique for simulating the effect of dose reduction on image quality in digital chest radiography," *J. Digit. Imag.*, vol. 22, no. 2, pp. 114–125, 2009. [Online]. Available: <http://dx.doi.org/10.1007/s10278-008-9104-5>
- [3] A. Svalkvist and M. Båth, "Simulation of dose reduction in tomosynthesis," *Med. Phys.*, vol. 37, no. 1, pp. 258–269, 2010. [Online]. Available: <http://dx.doi.org/10.1118/1.3273064>
- [4] A. Mackenzie, D. R. Dance, A. Workman, M. Yip, K. Wells, and K. C. Young, "Conversion of mammographic images to appear with the noise and sharpness characteristics of a different detector and x-ray system," *Med. Phys.*, vol. 39, no. 5, pp. 2721–2734, 2012. [Online]. Available: <http://dx.doi.org/10.1118/1.4704525>
- [5] S. Zabic, Q. Wang, T. Morton, and K. M. Brown, "A low dose simulation tool for CT systems with energy integrating detectors," *Med. Phys.*, vol. 40, no. 3, 2013. Art. no. 031102. [Online]. Available: <http://dx.doi.org/10.1118/1.4789628>
- [6] A. Mackenzie, D. R. Dance, O. Diaz, and K. C. Young, "Image simulation and a model of noise power spectra across a range of mammographic beam qualities," *Med. Phys.*, vol. 41, no. 12, 2014. Art. no. 121901. [Online]. Available: <http://dx.doi.org/10.1118/1.4900819>
- [7] L. R. Borges, H. C. R. de Oliveira, P. F. Nunes, and M. A. C. Vieira, "Method for inserting noise in digital mammography to simulate reduction in radiation dose," *Proc. SPIE*, vol. 9412, 2015. Art. no. 94125J. [Online]. Available: <http://dx.doi.org/10.1117/12.2082257>
- [8] L. R. Borges, H. C. R. de Oliveira, P. F. Nunes, P. R. Bakic, A. D. A. Maidment, and M. A. C. Vieira, "Method for simulating dose reduction in digital mammography using the Anscombe transformation," *Med. Phys.*, vol. 43, no. 6, pp. 2704–2714, 2016. [Online]. Available: <http://dx.doi.org/10.1118/1.4948502>
- [9] K. Dabov, A. Foi, V. Katkovnik, and K. Egiazarian, "Image denoising by sparse 3-D transform-domain collaborative filtering," *IEEE Trans. Image Process.*, vol. 16, no. 8, pp. 2080–2095, Aug. 2007. [Online]. Available: <http://dx.doi.org/10.1109/TIP.2007.901238>
- [10] E. Vansteenkiste, D. Van der Weken, W. Philips, and E. Kerre, "Perceived image quality measurement of state-of-the-art noise reduction schemes," in *Proc. Adv. Concepts Intell. Vis. Syst.*, 2006, pp. 114–126. [Online]. Available: http://dx.doi.org/10.1007/11864349_11
- [11] P. Chatterjee and P. Milanfar, "Bias modeling for image denoising," in *Proc. Conf. Rec. Forty-Third Asilomar Conf. Signals, Syst. Comput.*, 2009, pp. 856–859. [Online]. Available: <http://dx.doi.org/10.1109/ACSSC.2009.5469988>
- [12] J.-L. Starck, F. D. Murtagh, and A. Bijaoui, *Image Processing and Data Analysis: The Multiscale Approach*. Cambridge, U.K.: Cambridge Univ. Press, 1998. [Online]. Available: <http://www.multiresolution.com/cupbook.pdf>
- [13] M. Mäkitalo and A. Foi, "Optimal inversion of the Anscombe transformation in low-count Poisson image denoising," *IEEE Trans. Image Process.*, vol. 20, no. 1, pp. 99–109, Jan. 2011. [Online]. Available: <http://dx.doi.org/TIP.2010.2056693>
- [14] J. H. Curtiss, "On transformations used in the analysis of variance," *Ann. Math. Statist.*, vol. 14, no. 2, pp. 107–122, 1943. [Online]. Available: <http://dx.doi.org/10.1214/aoms/1177731452>
- [15] F. J. Anscombe, "The transformation of Poisson, binomial and negative-binomial data," *Biometrika*, vol. 35, no. 3/4, pp. 246–254, 1948. [Online]. Available: <http://www.jstor.org/stable/2332343>
- [16] A. Foi, "Clipped noisy images: Heteroskedastic modeling and practical denoising," *Signal Process.*, vol. 89, no. 12, pp. 2609–2629, 2009. [Online]. Available: <http://dx.doi.org/10.1016/j.sigpro.2009.04.035>
- [17] M. Mäkitalo and A. Foi, "Noise parameter mismatch in variance stabilization, with an application to Poisson–Gaussian noise estimation," *IEEE Trans. Image Process.*, vol. 23, no. 12, pp. 5348–5359, Dec. 2014. [Online]. Available: <http://dx.doi.org/10.1109/TIP.2014.2363735>
- [18] S. K. Bar-Lev and P. Enis, "On the construction of classes of variance stabilizing transformations," *Statist. Probability Lett.*, vol. 10, no. 2, pp. 95–100, 1990. [Online]. Available: [http://dx.doi.org/10.1016/0167-7152\(90\)90002-O](http://dx.doi.org/10.1016/0167-7152(90)90002-O)
- [19] J. A. Nelder and R. Mead, "A simplex method for function minimization," *Comput. J.*, vol. 7, no. 4, pp. 308–313, 1965. [Online]. Available: <http://dx.doi.org/10.1093/comjnl/7.4.308>
- [20] A. R. Conn, K. Scheinberg, and L. N. Vicente, *Introduction to Derivative-Free Optimization*. vol. 8, Philadelphia, PA, USA: SIAM, 2009. [Online]. Available: <http://dx.doi.org/10.1137/1.9780898718768>
- [21] A. Foi, "Optimization of variance-stabilizing transformations," 2009, Preprint. [Online]. Available: <http://www.cs.tut.fi/~foi/papers/Foi-OptimizationVST-preprint.pdf>

Appendix to the manuscript “Unbiased Injection of Signal-Dependent Noise in Variance-Stabilized Range”

Lucas Rodrigues Borges, Marcelo Andrade da Costa Vieira, and Alessandro Foi

In this appendix we detail the mathematical steps that lead from (5) and (6) to (7) and (8) on the second page of the manuscript.

We begin from expanding the output of the noise-injection operator as

$$\Phi_{\lambda, \lambda}(\hat{z}) = \frac{x^2}{4\lambda} - \frac{3}{8\lambda} - \frac{\sigma^2}{4\lambda},$$

where x is obtained by applying f to \hat{z} followed by the addition of noise,

$$x = 2\sqrt{\lambda\hat{z} + \frac{3}{8}} + \sigma n, \quad n(\cdot) \sim \mathcal{N}(0, \sigma^2).$$

Throughout our analysis, we treat $\{x^2|y\}$ as a mixture distribution with mixture components $C_j = \{x^2|\hat{z} = \lambda^{-1}j\}$ and mixture weights w_j equal to the scaled Poisson probability $\mathbb{P}(\hat{z} = \lambda^{-1}j|y)$, $j = 0, 1, 2, \dots$. According to this mixture model, we have

$$\mathbb{E}\{\Phi_{\lambda, \lambda}(\hat{z})|y\} = \frac{\mathbb{E}\{x^2|y\}}{4\lambda} - \frac{3}{8\lambda} - \frac{\sigma^2}{4\lambda} = \frac{1}{4\lambda} \sum_{j=0}^n w_j m_j - \frac{3}{8\lambda} - \frac{\sigma^2}{4\lambda} \quad (14)$$

$$\text{var}\{\Phi_{\lambda, \lambda}(\hat{z})|y\} = \frac{\text{var}\{x^2|y\}}{16\lambda^2} = \frac{1}{16\lambda^2} \left(\sum_{j=0}^n w_j (m_j^2 + s_j^2) - m^2 \right) \quad (15)$$

where m_j and s_j^2 are respectively the mean and variance of C_j , and $m = \sum_{j=0}^n w_j m_j = \mathbb{E}\{x^2|y\}$.

For any given value of \hat{z} , the conditional distribution of x is a normal centered at $f(\hat{z})$:

$$\{x|\hat{z}\} \sim \mathcal{N}\left(2\sqrt{\lambda\hat{z} + \frac{3}{8}}, \sigma^2\right).$$

Hence,

$$\left\{\frac{x}{\sigma}|\hat{z}\right\} \sim \mathcal{N}\left(\frac{2}{\sigma}\sqrt{\lambda\hat{z} + \frac{3}{8}}, 1\right)$$

Therefore, for any given value of \hat{z} , x^2/σ^2 follows a non-central χ^2 distribution with 1 degree of freedom and non-centrality parameter $\mu^2 = \mathbb{E}^2\left\{\frac{x}{\sigma}|\hat{z}\right\}$. The conditional expectation and variance are thus

$$\begin{aligned} \mathbb{E}\left\{\frac{x^2}{\sigma^2}|\hat{z}\right\} &= 1 + \mu^2 = 1 + \frac{4}{\sigma^2} \left(\lambda\hat{z} + \frac{3}{8}\right), \\ \text{var}\left\{\frac{x^2}{\sigma^2}|\hat{z}\right\} &= 2 + 4\mu^2 = 2 + \frac{16}{\sigma^2} \left(\lambda\hat{z} + \frac{3}{8}\right). \end{aligned}$$

Hence,

$$\mathbb{E}\{x^2|\hat{z} = \lambda^{-1}j\} = m_j = \sigma^2 + 4 \left(j + \frac{3}{8}\right), \quad (16)$$

$$\text{var}\{x^2|\hat{z} = \lambda^{-1}j\} = s_j^2 = 2\sigma^4 + 16\sigma^2 \left(j + \frac{3}{8}\right). \quad (17)$$

Substituting (16) into (14) and recalling that $\lambda \hat{z} \sim \mathcal{P}(\lambda y)$ yields (7):

$$\begin{aligned} \mathbb{E} \{ \Phi_{\lambda, \lambda}(\hat{z}) | y \} &= \frac{1}{4\lambda} \sum_{j=0}^n \mathbb{P}(\hat{z} = \lambda^{-1} j | y) \left(\sigma^2 + 4 \left(j + \frac{3}{8} \right) \right) - \frac{3}{8\lambda} - \frac{\sigma^2}{4\lambda} = \\ &= \frac{1}{\lambda} \sum_{j=0}^n \mathbb{P}(\hat{z} = \lambda^{-1} j | y) j = \frac{1}{\lambda} \sum_{j=0}^n \mathbb{P}(\lambda \hat{z} = j | y) j = \frac{1}{\lambda} \mathbb{E} \{ \lambda \hat{z} | y \} = y. \end{aligned} \quad (18)$$

Combining (18) with (14) also gives $m = 4\lambda y + \frac{3}{2} + \sigma^2$. We can now substitute (17) into (15):

$$\begin{aligned} \text{var} \{ \Phi_{\lambda, \lambda}(\hat{z}) | y \} &= \frac{1}{16\lambda^2} \left(\sum_{j=0}^n \mathbb{P}(\hat{z} = \lambda^{-1} j | y) \left(\left(\sigma^2 + 4 \left(j + \frac{3}{8} \right) \right)^2 + 2\sigma^4 + 16\sigma^2 \left(j + \frac{3}{8} \right) \right) - \left(4\lambda y + \frac{3}{2} + \sigma^2 \right)^2 \right) = \\ &= \frac{1}{16\lambda^2} \left(\sum_{j=0}^n \mathbb{P}(\hat{z} = \lambda^{-1} j | y) (16j^2 + 24j\sigma^2 + 12j - 16y^2\lambda^2 - 8y\sigma^2\lambda - 12y\lambda + 2\sigma^4 + 6\sigma^2) \right). \end{aligned}$$

Noting, as in (18), that $\sum_{j=0}^n \mathbb{P}(\hat{z} = \lambda^{-1} j | y) j = \mathbb{E} \{ \lambda \hat{z} | y \} = \lambda y$, we obtain

$$\text{var} \{ \Phi_{\lambda, \lambda}(\hat{z}) | y \} = \frac{1}{\lambda^2} \left(\sum_{j=0}^n \mathbb{P}(\hat{z} = \lambda^{-1} j | y) \left(j^2 + \lambda y \sigma^2 - y^2 \lambda^2 + \frac{\sigma^4}{8} + \frac{3\sigma^2}{8} \right) \right).$$

Next, since $y^2 \lambda^2 = \left(\sum_{j=0}^n \mathbb{P}(\hat{z} = \lambda^{-1} j | y) j \right)^2$, we have $\sum_{j=0}^n \mathbb{P}(\lambda \hat{z} = j | y) j^2 - y^2 \lambda^2 = \text{var} \{ \lambda \hat{z} | y \} = \lambda y$ and hence

$$\begin{aligned} \text{var} \{ \Phi_{\lambda, \lambda}(\hat{z}) | y \} &= \frac{1}{\lambda^2} \left(\sum_{j=0}^n \mathbb{P}(\hat{z} = \lambda^{-1} j | y) \left(\lambda y (1 + \sigma^2) + \frac{\sigma^4}{8} + \frac{3\sigma^2}{8} \right) \right) = \\ &= \frac{y(1 + \sigma^2)}{\lambda} + \frac{\sigma^4}{\lambda^2 8} + \frac{3\sigma^2}{8\lambda^2}. \end{aligned}$$

Since $\sigma^2 = \frac{\lambda}{\lambda} - 1$, we finally obtain (8):

$$\text{var} \{ \Phi_{\lambda, \lambda}(\hat{z}) | y \} = \frac{y}{\lambda} + \frac{\lambda^2 + \lambda\lambda - 2\lambda^2}{8\lambda^2\lambda^2}.$$

Paper 4: Method for simulating dose reduction in digital breast tomosynthesis

In reference to IEEE copyrighted material which is used with permission in this thesis, the IEEE does not endorse any of University of São Paulo's products or services. Internal or personal use of this material is permitted. If interested in reprinting/republishing IEEE copyrighted material for advertising or promotional purposes or for creating new collective works for resale or redistribution, please go to http://www.ieee.org/publications_standards/publications/rights/rights_link.html to learn how to obtain a License from RightsLink.

Method for Simulating Dose Reduction in Digital Breast Tomosynthesis

Lucas R. Borges, Igor Guerrero, Predrag R. Bakic, Alessandro Foi,
Andrew D. A. Maidment, and Marcelo A. C. Vieira

Abstract—This work proposes a new method of simulating dose reduction in digital breast tomosynthesis (DBT), starting from a clinical image acquired with a standard radiation dose. It considers both signal-dependent quantum and signal-independent electronic noise. Furthermore, the method accounts for pixel crosstalk, which causes the noise to be frequency-dependent, thus increasing the simulation accuracy. For an objective assessment, simulated and real images were compared in terms of noise standard deviation, signal-to-noise ratio (SNR) and normalized noise power spectrum (NNPS). A two-alternative forced-choice (2-AFC) study investigated the similarity between the noise strength of low-dose simulated and real images. Six experienced medical physics specialists participated on the study, with a total of 2,160 readings. Objective assessment showed no relevant trends with the simulated noise. The relative error in the standard deviation of the simulated noise was less than 2% for every projection angle. The relative error of the SNR was less than 1.5%, and the NNPS of the simulated images had errors less than 2.5%. The 2-AFC human observer experiment yielded no statistically significant difference ($p=0.84$) in the perceived noise strength between simulated and real images. Furthermore, the observer study also allowed the estimation of a dose difference at which the observer perceived a just-noticeable difference (JND) in noise levels. The estimated JND value indicated that a change of 17% in the current-time product was sufficient to cause a noticeable difference in noise levels. The observed high accuracy, along with the flexible calibration, make this method an attractive tool for clinical image-based simulations of dose reduction.

Index Terms—Electronic noise, digital breast tomosynthesis, dose reduction, quantum noise.

I. INTRODUCTION

DIGITAL breast tomosynthesis (DBT) is rapidly emerging as a major clinical tool for breast cancer screening. In DBT, a set of radiographic projections is acquired within a limited angular range around the breast. The projections are then reconstructed into a 3D volume made up of tomographic slices of the breast. The 3D visualization of the breast anatomy reduces tissue overlap if compared to conventional mammography, thus increasing the sensitivity and specificity of cancer detection [1]–[3].

Copyright (c) 2017 IEEE. Personal use of this material is permitted. However, permission to use this material for any other purposes must be obtained from the IEEE by sending a request to pubs-permissions@ieee.org.

This work was supported by the São Paulo Research Foundation (FAPESP grant no. 2016/25750-0), by the Brazilian Foundation for the Coordination of Improvement of Higher Education Personnel (CAPES grant no. 88881.030443/2013-01) and by the Academy of Finland (project no. 252547).

L.R. Borges, I. Guerrero and M.A.C. Vieira are with the University of São Paulo, Brazil (e-mail: lucas.rodrigues.borges@usp.br, igor.guerrero@usp.br, mvieira@sc.usp.br); A. Foi is with Tampere University of Technology, Finland (e-mail: alessandro.foi@tut.fi); P.R. Bakic and A.D.A. Maidment are with the University of Pennsylvania (e-mail: predrag.bakic@uphs.upenn.edu, andrew.maidment@uphs.upenn.edu).

As DBT is still being developed, the optimization of radiation dose is an open issue [4], [5]. The International Basic Safety Standards for Protection against Ionizing Radiation and for the Safety of Radiation Sources defines that diagnostic exposures of patients must “be the minimum necessary to achieve the required diagnostic objective” [6]. The literature presents a variety of approaches to achieve dose savings while maintaining the desired image quality. Some examples are the optimization of acquisition protocols [7], [8], the application of post-processing filters to low-dose projections [9], the development of iterative reconstruction methods [10], [11].

To validate these studies and enforce the minimum dose requirement, it is desirable to have a set of clinical images acquired from the same patient at different radiation doses. However, the availability of such images is extremely limited, since it requires the repeated exposure of patients to x-rays.

One common approach to overcome this limitation is to perform simulations of dose reduction through the injection of quantum noise in clinical images acquired with the standard radiation dose [12]–[14]. In fact, many of the studies regarding the optimization of radiation dose for radiographic imaging systems were conducted using simulated images [15], [16].

X-ray imaging commonly involves signal-dependent noise models where the variance of the noise is expressed as a function of the noise-free signal. Since the noise-free signal is not usually available, some methods simulate signal-dependent noise by approximating, in the definition of the variance, the noise-free signal by the noisy one [12]–[14]. This approximation can be rather coarse, mainly at a reduced count-rate regime [17].

In previous work, we proposed a method of simulating dose reduction in full-field digital mammography (FFDM) images, based on noise injection in a variance-stabilized range [17], [18]. It has the advantage that no previous knowledge of the noise-free signal is needed, avoiding errors due to approximation. However, although it is a precise method for the simulation of 2D digital mammography, it has some constraints that limited the performance of the method to digital breast tomosynthesis (DBT) images [19]: the noise was modeled exclusively as white Poisson noise, that is, it does not consider the spatial correlation between pixels of acquisition system (detector crosstalk) and also does not consider the electronic noise of the equipment. Moreover, the method needs two sets of calibration images: one with the same radiographic factors of the original clinical image (standard dose) and other with the radiographic factors of the simulated low-dose image, which is a challenge for clinical applicability.

Because individual DBT projections are acquired at substantially lower radiation levels, the overall signal at each projection is lower. In a reduced count-rate regime, the additive electronic noise plays an important role and has to be considered in the noise model [20], [21]. Furthermore, approximations of the noise-free signal, commonly applied for the simulation of signal-dependent noise, become coarse at lower counting regimes and thus limits the performance of the simulation methods.

Thus, this work proposes a new method of simulating dose reduction in DBT. It considers both quantum and electronic noise sources, the noise spatial correlation, and eliminates approximations of the noise-free signal. The method also has high clinical practicality, since the number of calibration images is reduced. Moreover, we present an extensive validation of the algorithm through objective measurements and human observer experiments. Although the present work focuses on the validation of the simulation method to DBT images, the algorithm can be explored in other imaging modalities that present similar noise properties.

II. PRELIMINARIES

A. DBT imaging system

In a DBT system, the breast is compressed and kept stationary while the x-ray tube moves around it in a limited angular range. During the movement, a series of raw projections are acquired. The raw projections go through a reconstruction process to generate slices parallel to the detector, known as reconstructed slices. The slices are then transmitted to a diagnostic workstation to be assessed by a radiologist [20].

The proposed simulation method performs mathematical operations on the raw projections, acquired with a standard radiation dose, to simulate lower-dose acquisitions. After the simulation is performed, the simulated projections must be reconstructed to generate lower-dose reconstructed slices.

B. Problem formulation

Let $z_{in}(i, j)$ be observed pixels at positions (i, j) of a DBT raw projection image. We model the input variable z_{in} as

$$z_{in}(i, j) = y(i, j) + \tau + s(y(i, j)) \xi(i, j), \quad (1)$$

where $y > 0$ is the (unknown) noise-free signal, proportional to the energy of the x-rays reaching the detector, $\tau > 0$ is the signal intensity offset, ξ is signal-independent random noise with zero mean and unit variance, and s is a function of y that defines the standard deviation of the overall noise. At each pixel, the expectation and variance of z_{in} are modeled as

$$E\{z_{in}(i, j)|y(i, j)\} = y(i, j) + \tau, \quad (2)$$

$$s^2(y(i, j)) = \text{var}\{z_{in}(i, j)|y(i, j)\} = y(i, j) \lambda_{in}(i, j) + \sigma_E^2, \quad (3)$$

where λ_{in} is the linear coefficient of the noise variance function, which can be attributed to the quantum efficiency and gain in the image formation, and σ_E^2 is the variance of the signal-independent portion of the noise. The above model (2)-(3) can also be used, in practice, in the presence of spatial correlation caused by pixel crosstalk at the detector,

as discussed in Appendix A. The ratio between y and $s(y)$ gives the pixelwise signal-to-noise ratio (SNR) of z_{in} . For a given current and kVp, shorter exposure time means lower radiation dose, hence smaller y and consequently lower SNR.

Our goal is to obtain from z_{in} a new set of noisier observations z_{out} that simulate a lower-dose acquisition and fulfill the following conditions:

$$E\{z_{out}(i, j)|y(i, j)\} = \gamma y(i, j) + \tau, \quad (4)$$

$$\text{var}\{z_{out}(i, j)|y(i, j)\} = \gamma y(i, j) \lambda_{in}(i, j) + \sigma_E^2, \quad (5)$$

where $0 < \gamma < 1$ is the dose reduction factor that we wish to simulate.

III. METHOD

The proposed method consists of five steps: linearization, injection of quantum noise, signal scaling, injection of electronic noise, and injection of signal offset. The method requires a set of raw clinical DBT projections and a set of raw uniform projections acquired with the same radiographic factors as the clinical DBT, which henceforth are named calibration projections. The five-step algorithm is applied to each raw projection of the clinical DBT, using the respective raw projection of the calibration image. The calibration image is required for the estimation of parameters. Fig. 1 shows an overview of the complete pipeline.

A. Estimation of parameters

For the correct application of the dose-reduction simulation pipeline, it is important to correctly estimate the noise and signal parameters τ , σ_E^2 , and λ_{in} .

1) *Pixel offset τ* : The National Health Service Breast Screening Program (NHSBSP) [22] has developed a practical method of calculating the pixel offset, which we applied in this work. Another alternative method of estimating pixel offset is by acquiring a dark-field image [23].

2) *Variance of the electronic noise σ_E^2* : The variance σ_E^2 can be estimated using noise parameter estimation algorithms [24]–[26]. For this purpose, we use software [25], available for download [27]. The software can estimate the standard deviation of the additive portion of signal-dependent noise provided that the pixel gain is constant through the field. To enable this, we selected a rectangular region of interest (ROI) with a short span along the anterior-posterior direction and much longer span along the orthogonal direction, located near the chest wall. Using this elongated ROI, we take advantage of the fact that the pixel gain varies more slowly in the orthogonal direction than in the anterior-posterior direction, due to the flat-field correction commonly used in commercial DBT systems. The estimation of σ_E^2 is performed using raw projections from the input DBT clinical images.

3) *Linear coefficient λ_{in} of the noise variance function*: The ideal way of obtaining λ_{in} would be by accessing the calibration data of the clinical unit used to acquire the DBT projections. However, this information is not easily available and thus λ_{in} has to be estimated from the acquired images. We estimate λ_{in} using the calibration image given as input, acquired at the same radiographic factor as the original image.

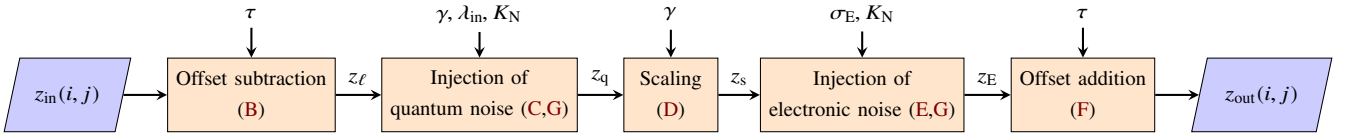


Fig. 1. Overview of the proposed dose-reduction simulation pipeline. Reconstruction methods can be applied to z_{out} , generating lower-dose tomosynthesis slices. The capital letters in parentheses refer to the corresponding subsections within Section III.

The estimation can be performed using a simple derivation of the standard deviation model presented in (2) and (3):

$$\lambda_{in}(i, j) = \frac{\hat{\sigma}^2(i, j) - \sigma_E^2}{\hat{\mu}(i, j) - \tau}, \quad (6)$$

where $\hat{\mu}(i, j)$ and $\hat{\sigma}^2(i, j)$ are, respectively, the local mean and local variance estimated from the calibration image. Values of τ , σ_E^2 , and λ_{in} for the system used in our experimental results are given in Section IV.

B. Offset subtraction

To scale the intensity of the clinical image correctly, the method requires a linear relationship between the expectation of the observed signal z_{in} and the underlying signal y . Thus, we define the linearized signal $z_\ell(i, j)$ as

$$z_\ell(i, j) = z_{in}(i, j) - \tau. \quad (7)$$

C. Injection of quantum noise

In previous work, we proposed an operator capable of injecting signal-dependent quantum noise through a variance-stabilizing transformation (VST) [17], [18], [28]. We have implemented the method to simulate dose reduction in FFDM images [18], and optimized the operator to maintain high performance even for applications with limited count rate [17].

In the current work we propose the injection of quantum noise through a nonlinear operator Φ . In DBT images, the electronic portion of the noise represents a relevant part of the image degradation, thus the operator must be adequate for signal-dependent noise models with affine variance like (3). The operator changes the variance of the combination of input noise and of the injected noise so as to yield the desired signal-dependent quantum noise for the reduced-dose output. It does not require previous knowledge of the shape of the distribution ξ or of the noise-free signal $y(i, j)$, therefore decreasing bias due to approximations, as shown in [17]. Considering the linearized DBT signal $z_\ell(i, j)$, we define the operator Φ as

$$z_q(i, j) = \Phi[z_\ell(i, j)] = \frac{\lambda_{in}(i, j)}{4} \left(x^2(i, j) - \frac{\sigma_A^2}{2} \right), \quad (8)$$

where $\sigma_A = \sqrt{(1/\gamma) - 1}$ and $x(i, j)$ is obtained by applying a root transformation to $z_\ell(i, j)$, followed by addition of signal-independent Gaussian noise with variance σ_A^2 :

$$x(i, j) = 2\sqrt{\frac{z_\ell(i, j)}{\lambda_{in}(i, j)} - \frac{\sigma_A^2}{8}} + \sigma_A \eta(i, j), \quad (9)$$

η being Gaussian noise with zero mean and unit variance, $\eta(i, j) \sim \mathcal{N}(0, 1)$. The mean and variance of z_q are

$$E\{z_q(i, j) | y(i, j)\} = y(i, j), \quad (10)$$

$$\text{var}\{z_q(i, j) | y(i, j)\} = \frac{y(i, j) \lambda_{in}(i, j)}{\gamma} + \sigma_E^2. \quad (11)$$

The variable $z_q(i, j)$, modulo multiplication by the dose reduction factor γ , has quantum noise with the target linear scaling λ_{out} . In Appendix B we provide a method to obtain the operator Φ and discuss its properties.

D. Scaling

The next step is to scale the overall signal of the DBT image. Because the input signal was linearized previously, this can be done by multiplying $z_q(i, j)$ by the dose reduction factor γ :

$$z_s(i, j) = \gamma z_q(i, j). \quad (12)$$

Both the mean and variance of $z_s(i, j)$ match those in (4)-(5), but only limited to the terms linear on $y(i, j)$. Hence, further adjustments are necessary to account for the electronic additive noise and offset.

E. Injection of electronic noise

After the above scaling, the variance of the additive electronic noise is also scaled to lower values. Thus, to fulfill (5), extra signal-independent noise is added to achieve the variance σ_E^2 of the electronic noise found in a clinical acquisition:

$$z_E(i, j) = z_s(i, j) + \sigma_v \nu(i, j), \quad (13)$$

where $\sigma_v = \sqrt{\sigma_E^2 (1 - \gamma^2)}$ and ν is zero-mean Gaussian noise with unit variance, $\nu(i, j) \sim \mathcal{N}(0, 1)$. The variance of z_E is

$$\text{var}\{z_E(i, j) | y(i, j)\} = \gamma y(i, j) \lambda_{in}(i, j) + \sigma_E^2. \quad (14)$$

The variable $z_E(i, j)$ achieves the target signal-dependent variance (5). Note that both noise injection steps (8) and (13) are pointwise and therefore it is irrelevant towards (4) and (5) whether the random variables z_ℓ or x are spatially uncorrelated or not. In fact, in our work, the injected noises η and ν are both spatially correlated to simulate the detector crosstalk, as detailed in Section III.G. The final adjustment addresses the target expectation.

F. Offset addition

Finally, the offset τ subtracted from the signal in the linearization step is added back to the signal:

$$z_{out}(i, j) = z_E(i, j) + \tau. \quad (15)$$

In this way, we attain both (4) and (5) exactly.

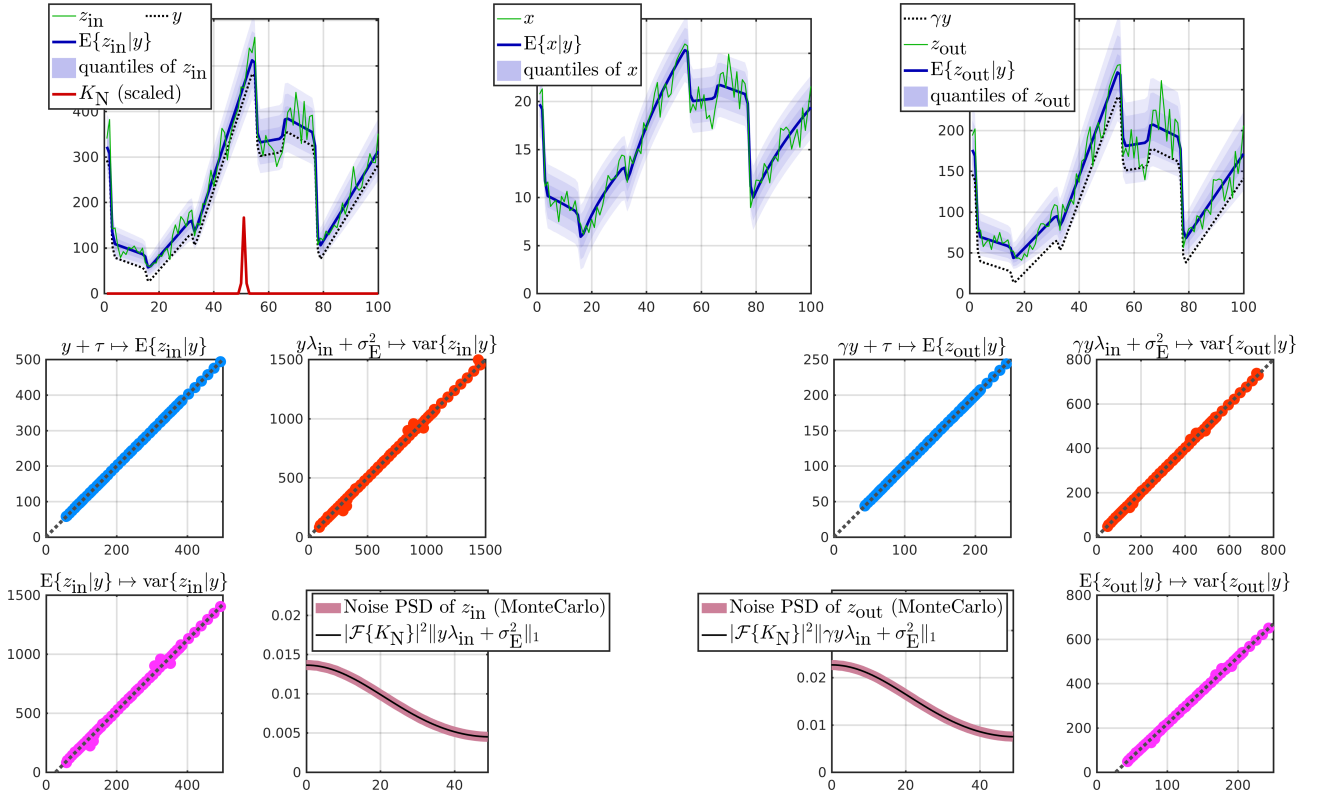


Fig. 2. Exemplary simulation using a 1D piecewise affine signal. The top row shows the input signal z_{in} (1) with parameters $\lambda_{in} = 3$, $\sigma_E = 3$, $\tau = 30$ (left), the transformed signal x used internally by the operator Φ (9) (center) and the output signal z_{out} obtained at the end of the proposed pipeline for a dose reduction factor $\gamma = 0.5$ (right). The kernel K_N is Gaussian with standard deviation 0.5. The four plots to the left show the expectation, variance and noise power spectrum for the input z_{in} computed from a MonteCarlo experiment with 10^6 realizations and compare these statistics with the analytical expressions in (2), (3) and (17). The four plots to the right visualize the same statistics for the output z_{out} and compare them with (4), (5), and (18), demonstrating accurate achievement of the design goals.

G. Detector crosstalk

In this work, we also consider the detector crosstalk, which causes the noise spectrum to be frequency-dependent (i.e. colored noise). This phenomenon is modeled through the power spectral density (PSD) Ψ of the noise. In practice, we compute Ψ from the calibration image through Fourier measurements over a running window as

$$\Psi = \frac{1}{M} \sum_{k=1}^M |\mathcal{F}\{I_{(i_k, j_k)} - S_{(i_k, j_k)}\}|^2, \quad (16)$$

where $I_{(i_k, j_k)}$ and $S_{(i_k, j_k)}$ are, respectively, the noisy calibration image and the local estimate of the noise-free image, over a window centered at (i_k, j_k) . The window selection and estimation S are detailed in Section IV. As we work with a single calibration image, we make a simplifying assumption that a unique PSD describes the correlation within the quantum noise as well as the correlation within electronic noise; we discuss this assumption further in Section VI.

Based on (3) and (5) (see also Appendix A), the noise PSD for z_{in} and z_{out} can be modeled as

$$\Psi_{z_{in}} = |\mathcal{F}\{K_N\}|^2 \|y\lambda_{in} + \sigma_E^2\|_1, \quad (17)$$

$$\Psi_{z_{out}} = |\mathcal{F}\{K_N\}|^2 \|\gamma y\lambda_{in} + \sigma_E^2\|_1, \quad (18)$$

where K_N is a convolution kernel that relates to Ψ as

$$K_N = K \|K\|_2^{-1}, \quad K = \mathcal{F}^{-1}\{\sqrt{\Psi}\}. \quad (19)$$

Hence, given a standard-dose image z_{in} subject to (2), (3) and (17), our goal is to simulate a reduced dose-image z_{out} that satisfies (4), (5), and (18). To this end, we generate correlated noises η (9) and ν (13) by convolving independent and identically distributed (IID) standard Gaussian white noises ω_η and ω_ν against K_N :

$$\eta = K_N * \omega_\eta, \quad \nu = K_N * \omega_\nu, \quad (20)$$

where $*$ denotes the convolution operation. Because K_N has unit ℓ^2 norm, both η and ν inherit the unit pointwise variance of ω_η and ω_ν .

Note that, being nonlinear, the operator Φ (8) may distort the correlation model of η when transforming the injected noise into quantum noise. However, in practice such distortions are not significant for the conditions described in this work.

H. Exemplary simulation

Before demonstrating the proposed approach on real DBT imagery, we illustrate it over a simulated 1D signal, as shown

in Fig. 2. This serves both as a validation of the procedure and as more direct visualization. Note that the shape of the quantile regions visualizes the signal-dependent variance of the signal z_{in} and z_{out} , whereas in x it is practically homoskedastic.

IV. EXPERIMENTAL SETUP

All images used in this work were acquired using a Selenia Dimensions (Hologic, Bedford, MA) DBT unit at the Hospital of the University of Pennsylvania. The system is equipped with an amorphous selenium (a-Se) detector layer that has a thickness of $200 \mu m$ and pixel pitch of $140 \mu m$. A total of 15 projections were acquired within an angular range of 15° .

The pixel offset τ was calculated using the protocol described by the NHSBPS [22], and a collection of central projections of uniform images acquired at four current-time products (60, 52, 42, and 30 mAs). The estimated τ for our experiments was 42.

The standard deviation σ_E of the electronic noise was estimated from an exposure of the anthropomorphic breast phantom in automatic exposure control mode (AEC), $31 kV_p$, tungsten target, aluminum filter and 60 mAs, using a $7 mm \times 105 mm$ ROI positioned close to the chest wall of and the methodology [25]. The estimated σ_E was 2.31.

Previous work on the same machine model found similar values of τ and σ_E [29]. Note that we used the same estimates of τ and σ_E for every experiment, as they do not change significantly over the dose levels considered in our experiments.

The parameters K_N and λ_{in} may change with the system calibration, and were thus estimated from calibration images acquired at the same radiographic factor as the input DBT used in the individual experiments; this is further specified in Sections IV.A and IV.B. Moreover, each projection angle requires a separate estimate of K_N and λ_{in} .

The convolution kernel K_N was estimated using a 64×64 running window with 50% overlap taken from the calibration projections according to (16) and (19). For the experiments, S is given as the mean value of I over the window. Fig. 3a shows one example of the estimated normalized kernel K_N .

The scaling factor λ_{in} was estimated using a 63×63 fully overlapping sliding window taken from the calibration images, and the relation defined by (6). Fig. 3b shows one example of the estimated map of local λ_{in} values at the central projection. Noteworthy, the parameter presented more relevant changes on the anterior-posterior (A-P) than on the orthogonal direction, as previously described in Section III.

A. Objective analysis

To assess the performance of the proposed method, objective metrics were calculated from uniform images. The uniform background allows for easy estimation of the signal and noise features.

The set of uniform images was obtained using a 4 cm poly methyl methacrylate (PMMA) block commonly used for flat-fielding the mammography system. The radiographic factors were manually set to $31 kV_p$, tungsten target and aluminum filter and the current-time product was reduced

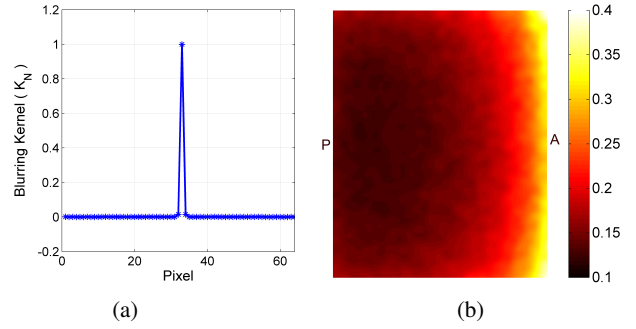


Fig. 3. Example of estimated parameters from the central projection of a calibration image acquired with 60 mAs, and $31 kV_p$. (a) Convolution kernel K_N (standard deviation 0.3). (b) Linear coefficient λ_{in} of the signal-dependent noise. Labels: P (posterior), A (anterior).

from 60 mAs to 52 mAs, 42 mAs and 30 mAs, to achieve reduced dose images. Two acquisitions were performed at each configuration, resulting in eight sets of 15 projections each.

The fidelity of the simulated images was investigated by comparing simulated images and real images acquired at the simulated radiation level. The comparison was done in terms of standard deviation, SNR, and normalized noise power spectrum (NNPS). First, the local standard deviation of the noise was estimated inside a fully overlapping 63×63 sliding window. The average relative error E_σ was calculated as

$$E_\sigma = \frac{100\%}{M} \sum_{k=1}^M \frac{\sigma_R(i_k, j_k) - \sigma_S(i_k, j_k)}{\sigma_R(i_k, j_k)}, \quad (21)$$

where $\sigma_R(i_k, j_k)$ and $\sigma_S(i_k, j_k)$ are the local noise standard deviations of the real and simulated images, respectively, estimated from a window centered at the pixel (i_k, j_k) , and M is the total number of windows.

Next, the SNR was estimated as the ratio between the signal mean and local standard deviation of the noise using the same window configuration mentioned above. The average relative error was calculated using the same approach as (21).

The last objective analysis used the NNPS [23], [30]. The NNPS was calculated for each projection using non-overlapping 64×64 pixels windows, taken from the central portion of the uniform images. The reported NNPS is the average of the spectra calculated for each window. The average relative error was calculated using (21).

Dependency on the calibration: Additional experiments were conducted to investigate the influence of the calibration images on the simulation performance. Ideally, the calibration image should be acquired with the same radiographic factors as the clinical image given as input, and using a PMMA block with attenuation similar to the breast, to enable the assumptions of the noise and signal models (1). Obtaining a wide range of calibration images can be clinically challenging, so we investigated the impact of using non-ideal calibration images as input for the simulation method.

The experiment was set as follows: uniform images were acquired using a 4 cm PMMA block at $31 kV_p$, with 60 mAs and 30 mAs. The proposed simulation method was applied

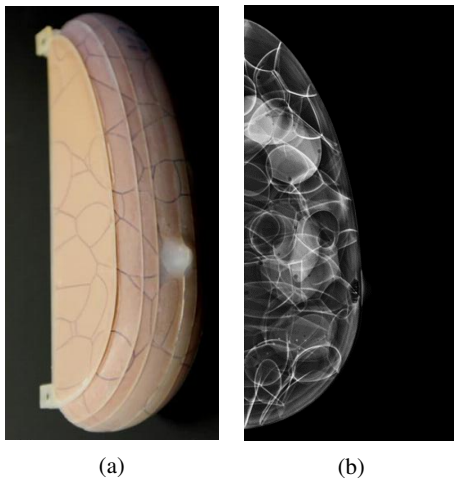


Fig. 4. Anthropomorphic breast phantom used for the human observer studies. (a) Photograph of the phantom. (b) Sample of the central slice.

to the 60 mAs image, simulating 30 mAs images, using a range of calibration images as input. The calibration images were acquired using combinations of 2 cm, 4 cm, and 6 cm PMMA blocks acquired with 40 mAs, 60 mAs, and 80 mAs. The method was evaluated in terms of average relative error of the standard deviation and NNPS, as defined by (21).

B. Human observer study

Inspired by Massoumzadeh *et al.* [31], a two-alternative forced-choice (2-AFC) study was conducted to confirm the equivalence in noise strength between simulated and real low-dose images in terms of human perception. The human observer study was conducted using images of a 3D anthropomorphic physical breast phantom, prototyped by CIRS, Inc. (Reston, VA) under license from the University of Pennsylvania [32]. The phantom consists of six slabs, each containing simulated anatomical structures manufactured using tissue mimicking materials, based upon a realization of the companion breast software phantom [33]. The physical phantom simulates a 450 ml breast, compressed to 5 cm, with 17% volumetric breast density (excluding the skin). Fig. 4 shows a photograph of the anthropomorphic breast phantom and an example of a DBT reconstructed central slice.

Real and simulated projections were reconstructed using a commercially available system (Briona Standard v4.0, Real Time Tomography, Villanova, PA). Reconstructed slices were evaluated using a RadiForce GS320 monitor (Eizo, Japan), with 3 MP resolution. The human observation study was conducted in a dark room appropriately prepared for this purpose, at the Hospital of the University of Pennsylvania. The readings were performed in one session per reader.

The observer study was organized as follows: five sets of projections were acquired using the anthropomorphic physical phantom at the radiographic factors given by the AEC (31 kV_p, tungsten target, aluminum filter and 60 mAs). The current-time product was then manually set to 30 mAs and the other

five sets of projections were acquired. Using the standard-dose image (60 mAs), sets of projections were simulated at 30 mAs, 36 mAs, 42 mAs, 48 mAs, 54 mAs, and 59 mAs. Calibration projections, required by the simulation method, were acquired using the same radiographic factors as the AEC (31 kV_p, tungsten target, aluminum filter and 60 mAs), and a uniform block of PMMA with 4 cm. A collection of four ROIs at nine different depths was selected from each realization and each dose, resulting in one set of 180 real ROIs, and six sets of 180 simulated ROIs, one set at each current-time exposure mentioned above (30 mAs - 59 mAs).

Each observer was presented with 360 pairs of ROIs, extracted from the exact same location in the phantom. One image of the pair was a real acquisition at 30 mAs, while the other image was its simulated counterpart. Sixty simulated images were taken from the pool of 59 mAs, another sixty were taken from the pool of 54 mAs, and so on. The sequence of simulated images at different mAs was randomized prior to presenting them to the observer. The observer was asked to select the image that contained less noise. Observers were allowed to zoom and pan, the position of the observer in relation to the monitor was free, and no window or level tools were allowed.

Software developed for this work automatically recorded the observers' choices and time of decision. If the observer was incapable of perceiving any differences in noise levels, we expected that the simulated image would be chosen randomly 50% of the time. As the difference between noise levels increases, the percentage of correct selection should also increase, reaching 100% when differences are obvious. Ideally, we expect to achieve 50% of correct selection when the simulated exposure time matches the real exposure time (30 mAs in our experiment).

The 2-AFC study can also help to identify the just-noticeable difference (JND) noise for DBT images. In this context, the JND represents how much the current-time product has to be increased (or decreased) before human observers start to perceive a difference in noise levels. The JND point is defined at an accuracy of 75%, which is the midway between complete guessing (50%) and easily noticeable difference (100%) among simulated and real images. This information can also be used as a target for accuracy levels of noise simulation algorithms.

V. RESULTS

The algorithm was validated using our MATLAB implementation. The method reported linear complexity, with approximately 2 Mpixel/s on a 3.40 GHz Intel Core i7-2600K CPU. Considering the size of the images simulated in this work (~3MP), the method simulates one DBT projection every 1.73 (± 0.09) seconds. The clinical unit used in this study acquires 15 projections per exam, thus a new full case is generated every 26 seconds.

A. Objective analysis

The standard deviation of the noise found at simulated and real acquisitions are presented in Fig. 5a and Fig. 5d.

Fig. 5a shows the local standard deviation of the noise at the central projection as a function of the distance to chest wall. Due to the flat-field calibration, the standard deviation of the noise increased as the distance to the chest wall increases, as expected [34]. Furthermore, the simulated values presented a good match visually with the real values. Fig. 5d shows the average error of the standard deviation of the simulated noise for different projections. Error bars represent the standard deviation of the error normalized by the square root of the number of samples. The average relative error was smaller than 2% for each projection angle.

The SNR calculated from simulated and real images are presented in Fig. 5b and Fig. 5e. Fig. 5b shows the local SNR at the central projection as a function of the distance to chest wall. As expected, when the noise standard deviation increased, the SNR decreased. Fig. 5e shows the average error of the SNR of the simulated and real images at different projections and doses. The error bars represent the standard deviation of the error normalized by the square root of the number of samples. The relative average error was smaller than 1% for all the projections.

The NNPS of the simulated and real acquisitions are presented in Fig. 5c and Fig. 5f. Fig. 5c shows the NNPS of the central projection for each simulated reduction. Fig. 5f shows the average error between the NNPS of the simulated and real images. Note that the proposed method was capable of accurately simulating the frequency-dependency of the noise. Error bars represent the standard deviation of the error normalized by the square root of the number of samples. The relative average error is smaller than 2.5% for all the projections.

Fig. 6 illustrates the importance of the spatial correlation considered in our noise model. The graph shows the NNPS calculated for a simulated image assuming that K_N is a dirac delta (i.e. without spatial correlation). The NNPS of a simulated image assuming spatial correlation is shown, estimating K_N using (16) and (19). Also shown is the NNPS of an actual acquisition at the simulated dose.

Dependency on calibration: To investigate the robustness of the proposed method to changes in the calibration image, the average relative error of the noise standard deviation and NNPS of the simulated images were analyzed at a range of beam qualities and PMMA thicknesses used for the calibration image; Fig. 7 shows the results. Fig. 7a shows the average relative error between the standard deviation of real and simulated noise. As expected, calibration images acquired at radiographic factors similar to the standard-dose image (60 mAs, 31 kVp, 4 cm) reported lower errors. Changes in mAs and thickness compensated each other, as seen at 80 mAs, 31 kVp, 6 cm. Fig. 7b shows the average relative error between the NNPS of real and simulated images. Again, the lowest error occurred when the calibration image was acquired at radiographic factors close to the standard-dose input image, and for a thickness similar to the patient's breast.

B. Human observer studies

The observer study allowed a subjective validation of the method. Fig. 8 (top row) shows a magnified ROI taken from

TABLE I. Characteristics of the observers of the 2-AFC study

Observer	1	2	3	4	5	6
Experience (years)	20	5	9	1	5	16
Avg. reading time (s/pair)	12	8	12	6	8	11

raw projections of a real acquisition at 60 mAs (AEC), a simulated image at 30 mAs, and a real acquisition at 30 mAs. The difference in noise levels between 60 mAs and 30 mAs can be appreciated visually. Fig. 8 (bottom row) shows the residual noise for each ROI from Fig. 8 (top row). The residual noise was estimated by subtracting an approximation of the noise-free signal from one of the realizations. The noise-free approximation was obtained by averaging all five realizations of the phantom acquired at the same radiographic factors. Note that the differences in terms of the residual noise of the real 60 mAs and simulated 30 mAs (left and center) were easily noticeable, while simulated 30 mAs and real 30 mAs (center and right) were not discernible, indicating the good performance of the proposed method. Fig. 9 shows a magnified ROI taken from reconstructed slices acquired with 60 mAs, simulated 30 mAs starting from 60 mAs, and acquired with 30 mAs. Note that the differences in noise levels can be easily perceived when analyzing Figs. 9 (a) and (b). Meanwhile, no differences in noise levels can be seen in Figs. 9 (b) and (c), indicating the good performance of the simulation method.

A total of six medical physics specialists participated on the 2-AFC experiment to validate the noise levels in simulated images. Table I provides an overview of the observers' experience in the medical physics field, and the average reading time per image pair.

The frequency of correct selection – which we define as the selection of simulated images – and the average time of decision are shown in Fig. 10, as a function of the relative increase in the current time product.

The first important finding from Fig. 10a is the frequency of correct selection at which the current-time product of simulated and real images were a perfect match (0% increase). For an ideal test (infinite samples) and an ideal simulation method, the desired frequency would be 50%. Our experiment reported a frequency of 47% [38% 60%], where the brackets represent the 95% confidence interval (C.I.). As the 2-AFC task respects a binomial distribution, the theoretical 95% C.I. for random selection with the used number of trials for each observer ($N=60$) can be easily calculated, and is equal to [33% 63%]. Note that the correct selection rate of each observer falls within the theoretical interval.

Additionally, a hypothesis test was performed to investigate if the frequency of correct selection at 0% mAs increment is statistically different from random selection (50%). As the selection frequency follows a Binomial distribution, the arcsin transformation was first applied to the data. A Shapiro-Wilk test [35] confirmed the normality of the transformed distribution ($p = 0.34$). As the hypothesis cannot be rejected at a significance level of 95% ($p = 0.84$), the t-test suggests that the noise strength of simulated and real images are not discernibly different by the human observers.

Fig. 10b shows an expected, but interesting trend in the

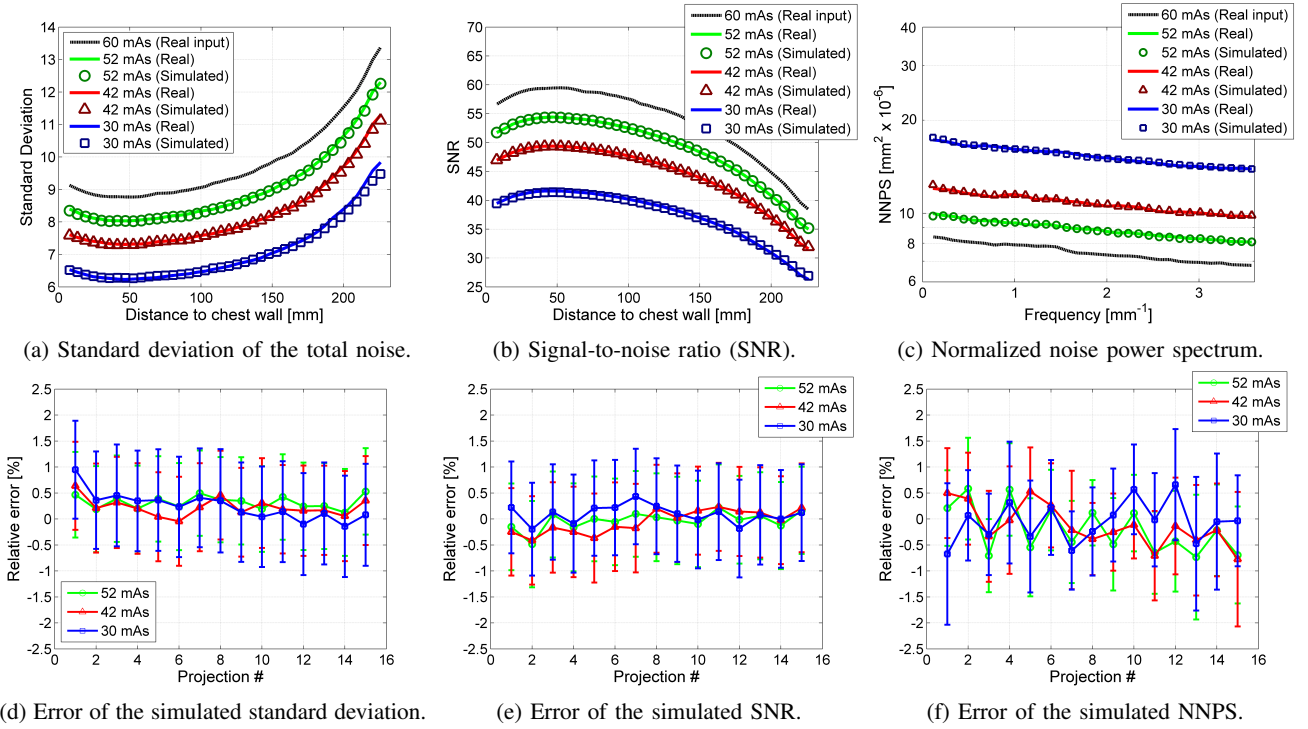


Fig. 5. Top row: objective metrics calculated at the central projection. Bottom row: average relative error between simulated and measured metrics. The bars represent the standardized errors.

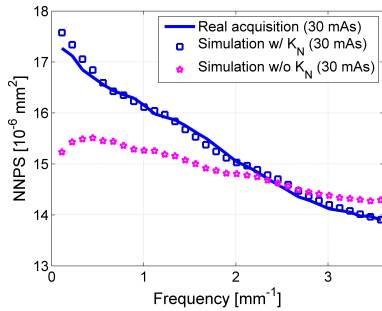


Fig. 6. Comparison of the simulated NNPS assuming no spatial correlation of the noise (w/o K_N), using the complete pipeline (w/ K_N), and the goal (real acquisition).

reading time. As the simulated and real images got more similar, the difficulty of choosing the correct image increased, causing the observer to spend more time trying to find the image containing less noise.

VI. DISCUSSION AND CONCLUSION

An accurate method for simulating dose reduction of DBT images was proposed in this work. It is a useful tool for studies of image quality, human perception and radiation dose when used in combination with DBT clinical images.

The work presented several innovations in relation to our previous methods [17]–[19]. The noise model accounts for flat-field corrections, electronic noise, and spatial correlation of the noise. Signal-dependent quantum noise was added though

a novel operator developed for this purpose. Furthermore, the use of only one calibration image adds to the clinical practicality of the method.

Detailed descriptions of the method, materials and validation were provided. The work also presents experimental techniques, proposed by other authors, for estimating the parameters used in the simulation process. This is important as the parameter estimation plays a crucial role in the simulation method.

To ensure the clinical practicality of the method, the pixel crosstalk was modeled as a single convolution kernel K_N applied to both noise sources. This approximation can only be made under the assumption that the noise color, i.e. the slope of the NNPS curve, does not report relevant changes with dose. As a result, the spectrum of the simulated noise may report errors when simulating dose reduction on highly-correlated systems. Furthermore, the error of the NNPS may increase when the method is used to simulate very low doses.

Extensive validation was conducted to ensure the accuracy of the proposed method. Objective measurements were calculated on uniform images, where the estimation of signal and noise properties are straightforward. The standard deviation of the noise from simulated and real low-dose images were compared in Fig. 5a and Fig. 5d. The results provide evidence that the simulation method was capable of adding noise with the correct standard deviation, even considering the flat field correction, which is made evident by the increase in noise standard deviation for pixels far from the chest wall. No trend is observed when the projection angle of the acquisition is varied, indicating that the method performs well for oblique

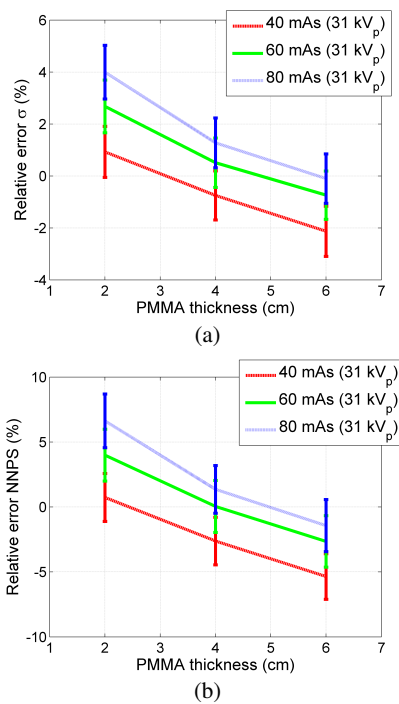


Fig. 7. Average relative error for a range of calibration images. (a) Error of the standard deviation of the simulated noise. (b) Error of the normalized noise power spectrum.

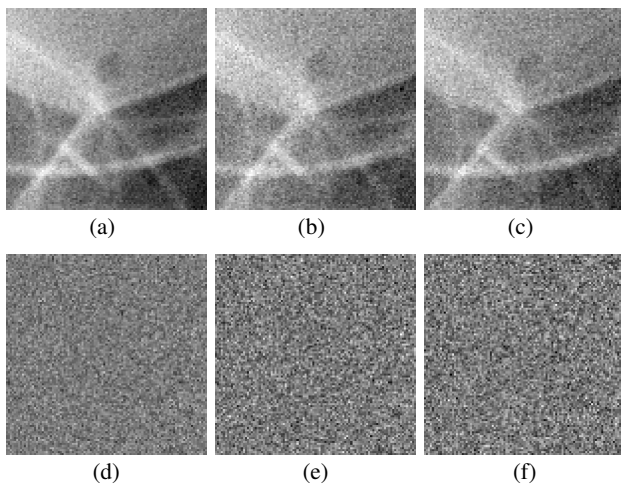


Fig. 8. Visual comparison between real and simulated projections. Raw magnified ROI (top row) and residual noise (bottom row) from acquisition with 60 mAs (a,d), simulation of 30 mAs starting from 60 mAs (b,e), acquisition with 30 mAs (c,f).

acquisition angles.

The second objective metric was the signal-to-noise ratio, presented in Fig 5b and Fig. 5e. As the noise standard deviation provides a good match, the SNR is an important indication that not only noise was simulated correctly, but also the scaling of the image signal. As expected, SNR drops farther from the chest wall, due to the higher standard deviation of the noise.

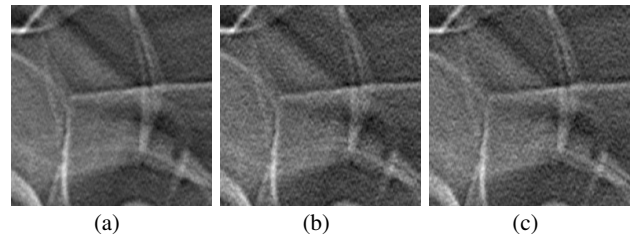


Fig. 9. Visual comparison between reconstructed slices from real and simulated projections. Magnified ROI from acquisition with 60 mAs (a), simulation of 30 mAs starting from 60 mAs (b), acquisition with 30 mAs (c).

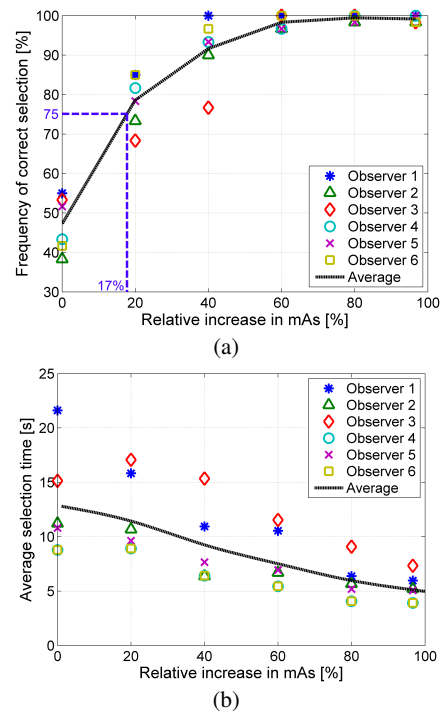


Fig. 10. Results from 2-AFC study. (a) Frequency of correct selection as a function of relative increment in mAs. (b) Time of decision as a function of relative increment in mAs.

The results presented in Fig. 5c and Fig. 5f shows that the spatial correlation, or pixel crosstalk, was simulated correctly in the low-dose images. The normalized noise power spectrum presented a good match with real low-dose acquisitions. Again, no trend can be seen as a function of the projection angle. Note that the correct simulation of the spatial correlation of the noise is crucial for the appropriate performance of readers when analysing simulated images. As spatially correlated noise presents some granularity, it represents an extra challenge to the image interpretation.

As the simulation method depends on a calibration image, we dedicated one section of this work to investigate how the use of non-ideal calibration images impacts the accuracy of the simulation method. The results indicate that it is possible to simulate dose reduction for a 4 cm case acquired at 60 mAs, using calibration images of phantoms from 2 cm to 6 cm

and with current-time product from 40 mAs to 80 mAs. The various combinations of these phantom thickness and current-time products yields errors lower than 6% in terms of standard deviation and 10% in terms of NNPS. We believe that these errors are acceptable, as previous work on CT [31], and photography [36] indicate that differences between 15% and 25% on the noise are not easily noticeable by human observers. Therefore, the proposed method is extremely flexible for clinical use, as a limited set of calibration images could be used to simulate dose reduction on an entire population.

The final validation was performed using a 3D anthropomorphic breast phantom and a 2-AFC observer study. As seen in Fig. 10, readers were not able to notice differences in the noise strength of simulated and real low-dose images, as the selection accuracy was close to random (50%). A Student's t-test was conducted and no statistical differences were found between the perception of noise strength from simulated and real images. Furthermore, Fig. 10 shows that the readers are good at detecting changes in noise levels - a relative increase of 20% in dose was enough to cause the correct selection rate to go from approx. 50% (guessing) to approx. 80%.

After the method was validated and the results indicated that the simulation was accurately performed, Fig. 10 can be interpreted to obtain a second important finding - the JND point. The JND value reported by this study was 17%, which falls within the range reported by others (15% - 25%) [31], [36]. While we do not claim that the dose for DBT examinations can be reduced without affecting the diagnostic outcome, in this study observers were not able to discern a 17% dose difference. The task of detection and lesion characterization were not considered in this work and would require a separate study.

In conclusion, we have proposed and validated a full pipeline capable of simulating dose reduction in DBT images. It considers both quantum and electronic noise and the spatial correlation of the pixels. We believe that the accuracy, along with the computational efficiency and flexibility of calibration make this method an attractive tool for clinical image-based simulations of dose reduction.

APPENDIX A. SPATIALLY CORRELATED SIGNAL-DEPENDENT NOISE

Let z_u denote the hypothetical signal measured by the detector if there were no crosstalk. The mean, variance, and PSD can be formalized as

$$\begin{aligned} \mathbb{E}\{z_u|y_u\} &= y_u + \tau_u, \\ \text{var}\{z_u|y_u\} &= \lambda_u y_u + \sigma_u^2, \\ \Psi_{z_u} &= \|\lambda_u y_u + \sigma_u^2\|_1, \end{aligned}$$

where the noise corrupting z_u is spatially uncorrelated hence white (i.e. flat PSD). By modeling the effect of the detector crosstalk as the convolution of z_u with a kernel $K_u \geq 0$, we have

$$\begin{aligned} \mathbb{E}\{z_u \otimes K_u|y_u\} &= y_u \otimes K_u + \tau_u \|K_u\|_1, \\ \text{var}\{z_u \otimes K_u|y_u\} &= \lambda_u y_u \otimes K_u^2 + \sigma_u^2 \|K_u\|_2^2, \\ \Psi_{z_u \otimes K_u} &= |\mathcal{F}\{K_u\}|^2 \|\lambda_u y_u + \sigma_u^2\|_1, \end{aligned} \quad (22)$$

Let the observations (1) originate from this process and set

$$\begin{aligned} y &= y_u \otimes K_u, & \tau &= \tau_u \|K_u\|_1, \\ z_{\text{in}} &= z_u \otimes K_u, & \lambda_{\text{in}} &= \lambda_u \frac{\|K_u\|_2^2}{\|K_u\|_1}, & \sigma_{\text{E}}^2 &= \sigma_u^2 \|K_u\|_2^2. \end{aligned}$$

These substitutions trivially yield (1), (2), and (17), with $K_N = K_u \|K_u\|_2^{-1}$. We can then analyze the discrepancy between $\lambda_{\text{in}} y = \lambda_{\text{in}} y_u \otimes K_u$ from (3) and $\lambda_u y_u \otimes K_u^2 = \lambda_{\text{in}} \frac{\|K_u\|_1}{\|K_u\|_2^2} y_u \otimes K_u^2$ from (22). In particular, by taking the Maclaurin series of $y_u(t_0 - \cdot)$ at an arbitrary location t_0 and using 1D formalism [37],

$$\begin{aligned} [\lambda_{\text{in}} y_u \otimes K_u](t_0) &= \lambda_{\text{in}} \sum_t y_u(t_0 - t) K_u(t) = \\ &= \lambda_{\text{in}} \sum_t \sum_{k=0}^{+\infty} \frac{\partial^k y_u(t_0) t^k}{(-1)^k k!} K_u(t) = \\ &= \lambda_{\text{in}} \sum_{k=0}^{+\infty} \frac{\partial^k y_u(t_0)}{(-1)^k k!} \sum_t t^k K_u(t), \end{aligned} \quad (23)$$

$$\begin{aligned} [\lambda_u y_u \otimes K_u^2](t_0) &= \lambda_{\text{in}} \frac{\|K_u\|_1}{\|K_u\|_2^2} \sum_t y_u(t_0 - t) K_u^2(t) = \\ &= \lambda_{\text{in}} \frac{\|K_u\|_1}{\|K_u\|_2^2} \sum_{k=0}^{+\infty} \frac{\partial^k y_u(t_0)}{(-1)^k k!} \sum_t t^k K_u^2(t). \end{aligned} \quad (24)$$

Comparing the k -th summand in (23) with the corresponding summand in (24) we observe the following: the first summands (i.e. $k=0$) coincide; if K_u is even symmetric, then the summands are zero for every odd k thanks to the odd symmetry of t^k . The above expressions generalize immediately to the 2D and higher-dimensional cases using the corresponding multi-index form of the Maclaurin series. Thus, the approximation

$$\text{var}\{z_u \otimes K_u|y_u\} = \lambda_u y_u \otimes K_u^2 + \sigma_{\text{E}}^2 \approx \lambda_{\text{in}} y_u \otimes K_u + \sigma_{\text{E}}^2$$

is especially accurate when y_u is smooth, when K_u is symmetric, and in general when K_u has a small support, due to the properties of the Lagrange remainder. Hence, as $z_{\text{in}} = z_u \otimes K_u$ and $y = y_u \otimes K_u$, we can approximate

$$\text{var}\{z_{\text{in}}|y_u\} \approx \lambda_{\text{in}} y + \sigma_{\text{E}}^2.$$

The conditioning upon y_u can be thus replaced by the point-wise conditioning upon y , leading to (3). Careful inspection of the plots of $\text{var}\{z_{\text{in}}|y\}$ in Fig. 2 confirms the goodness of this approximation in the practice and its negligible impact to the accuracy of the final result, even for crosstalk kernels wider than that characteristic of the hardware in our experiments.

APPENDIX B. OPERATOR Φ

In this appendix we demonstrate how the operator Φ was obtained, starting from a noisy input $z_\ell \geq 0$, such that:

$$z_\ell = y(\theta) + s(\theta) \xi_\theta, \quad \xi_\theta \sim \Xi_\theta, \quad (25)$$

where $\theta \in \Theta \subseteq \mathbb{R}$ is the (unknown) parameter conditioning the system, $y(\theta) = \mathbb{E}\{z_\ell|\theta\} \geq 0$, $s(\theta) = \text{std}\{z_\ell|\theta\} \geq 0$, ξ_θ , and Ξ_θ are, respectively, the conditional expectation, the conditional standard deviation, conditional standardized error, and the

standardized conditional distribution of z_ℓ . We represent Ξ_θ through its generalized probability density function p_θ ,

$$\text{prob}(\xi_\theta \leq \tau) = \int_{-\infty}^{\tau} p_\theta(\zeta) d\zeta. \quad (26)$$

Note that we can always identify θ with y , without loss of generality, as long as $y(\theta)$ is an invertible mapping of θ .

We consider a generic noise-injection operator Φ of the form

$$\Phi(z_\ell) = \frac{1}{c_1} \left(\frac{x^2}{4} - c_2 - \frac{\sigma_A^2}{4} \right),$$

where x is obtained by applying a root transformation f to z_ℓ followed by the addition of Gaussian noise,

$$x = f(z_\ell) + n = 2\sqrt{c_1 z_\ell + c_2} + \sigma_A \eta, \quad \eta(\cdot) \sim \mathcal{N}(0, 1).$$

Throughout our analysis, we assume $c_1 \neq 0$, $c_2 \in \mathbb{R}$, and $c_1 z_\ell + c_2 \geq 0$ ¹. We are interested in the case $\sigma_A > 0$, for which $\Phi(z_\ell) \neq z_\ell$.

We treat $\{x^2|\theta\}$ as a mixture distribution with mixture components $\{x^2|\xi_\theta = \zeta\}$ and mixture density $p_\theta(\zeta)$, $\zeta \in \mathbb{R}$. According to this mixture model, we have

$$\text{E}\{\Phi[z_\ell]|\theta\} = \frac{1}{4c_1} \left[\int_{\mathbb{R}} m(\zeta) p_\theta(\zeta) d\zeta - 4c_2 - \sigma_A^2 \right], \quad (27)$$

$$\text{var}\{\Phi[z_\ell]|\theta\} = \frac{1}{16c_1^2} \left[\int_{\mathbb{R}} (m^2(\zeta) + \varsigma^2(\zeta)) p_\theta(\zeta) d\zeta - \left(\int_{\mathbb{R}} m(\zeta) p_\theta(\zeta) d\zeta \right)^2 \right], \quad (28)$$

where $m(\zeta)$ and $\varsigma^2(\zeta)$ are respectively the mean and variance of $\{x^2|\xi_\theta = \zeta\}$, and $\int_{\mathbb{R}} m(\zeta) p_\theta(\zeta) d\zeta = \text{E}\{x^2|\theta\}$.

For any given value of z_ℓ , the conditional distribution of x is a normal centered at $f(z_\ell)$:

$$\{x|z_\ell\} \sim \mathcal{N}(2\sqrt{c_1 z_\ell + c_2}, \sigma_A^2).$$

Hence,

$$\{x\sigma_A^{-1}|z_\ell\} \sim \mathcal{N}(2\sigma_A^{-1}\sqrt{c_1 z_\ell + c_2}, 1).$$

Therefore, for any given value of z_ℓ , $x^2\sigma_A^{-2}$ follows a non-central χ^2 distribution with 1 degree of freedom and non-centrality parameter $\mu^2 = \text{E}^2\{x\sigma_A^{-1}|z_\ell\}$. The conditional expectation and variance are thus

$$\begin{aligned} \text{E}\{x^2\sigma_A^{-2}|z_\ell\} &= 1 + \mu^2 = 1 + 4(c_1 z_\ell + c_2)\sigma_A^{-2}, \\ \text{var}\{x^2\sigma_A^{-2}|z_\ell\} &= 2 + 4\mu^2 = 2 + 16(c_1 z_\ell + c_2)\sigma_A^{-2}. \end{aligned}$$

Consequently,

$$\text{E}\{x^2|\xi_\theta = \zeta\} = m(\zeta) = \sigma_A^2 + 4[c_1(y(\theta) + s(\theta)\zeta) + c_2], \quad (29)$$

$$\text{var}\{x^2|\xi_\theta = \zeta\} = \varsigma^2(\zeta) = 2\sigma_A^4 + 16\sigma_A^2[c_1(y(\theta) + s(\theta)\zeta) + c_2]. \quad (30)$$

¹In practice, negative samples can be replaced by 0, defining $f(z_\ell) = 2\sqrt{\max\{0, c_1 z_\ell + c_2\}}$. This non-negative clipping may lead to some imprecision if the proportion of negative samples is significant, e.g., if $\text{prob}(\xi_\theta \leq \frac{-1}{s(\theta)}(\frac{\xi_\theta^2}{c_1} + y(\theta))) > 0.05$.

Substituting (29) into (27) yields

$$\text{E}\{\Phi(z_\ell)|\theta\} = y(\theta) + s(\theta) \int_{\mathbb{R}} \zeta p_\theta(\zeta) d\zeta = y(\theta) = \text{E}\{z_\ell|\theta\}, \quad (31)$$

where the last identity follows from ξ_θ being a standardized error, thus $\int_{\mathbb{R}} \zeta p_\theta(\zeta) d\zeta = \text{E}\{\xi_\theta|\theta\} = 0$. Eq. (31) means that Φ operates an *exact unbiased injection* of noise. Note that this is valid regardless of the particular choice of c_1 , c_2 , and σ_A .

Next, we substitute (29) and (30) into (28). Simplifications lead to

$$\text{var}\{\Phi[z_\ell]|\theta\} = s^2(\theta) + \frac{\sigma_A^4}{8c_1^2} + \frac{\sigma_A^2 c_2}{c_1^2} + \frac{\sigma_A^2 y(\theta)}{c_1}, \quad (32)$$

where, in order to deduce $\int_{\mathbb{R}} \zeta^2 p_\theta(\zeta) d\zeta = \text{var}\{\xi_\theta|\theta\} = 1$, we again leverage the fact that ξ_θ is a standardized error.

It is important to note that (31) and (32) are valid for arbitrary conditional standard deviation $s(\theta)$ and standardized conditional distribution Ξ_θ of z_ℓ .

For the specific case of a z_ℓ as in (7), we have an affine variance $s^2(\theta) = \lambda_{\text{in}} y(\theta) + \sigma_E^2$, with $\lambda_{\text{in}} > 0$ and $\sigma_E^2 \in \mathbb{R}$; thus

$$\text{var}\{\Phi[z_\ell]|\theta\} = \left(\lambda_{\text{in}} + \frac{\sigma_A^2}{c_1} \right) y(\theta) + \sigma_E^2 + \frac{\sigma_A^4}{8c_1^2} + \frac{\sigma_A^2 c_2}{c_1^2}. \quad (33)$$

Therefore, to obtain a signal-dependent target variance where only the linear portion of the variance function is modified, we have

$$\text{var}\{\Phi[z_\ell]|\theta\} = \lambda_{\text{out}} y(\theta) + \sigma_E^2, \quad (34)$$

with $\lambda_{\text{out}} > \lambda_{\text{in}}$, it suffices to set

$$c_1 = \frac{\sigma_A^2}{\lambda_{\text{out}} - \lambda_{\text{in}}}, \quad c_2 = -\frac{\sigma_A^2}{8}. \quad (35)$$

In particular, for the observations (1)–(3) and goals described by (4) and (5), we have $\lambda_{\text{out}} = \lambda_{\text{in}}/\gamma$, $\sigma_A = \sqrt{(1/\gamma) - 1}$.

The application described in this work has observations with a signal intensity offset τ . The variable z_ℓ considers that such offset has been removed, as done in Section III-B. Furthermore, all the above derivations involve pointwise operations and thus they hold also when the noise η is spatially correlated (i.e. frequency-dependent); only its variance and Gaussian distribution matter. To simulate the spatial correlation due to detector crosstalk, η is obtained by convolving white Gaussian noise against a kernel K_N (20). Neither the variance nor the Gaussianity of η are affected by this operation.

ACKNOWLEDGMENT

The authors would like to thank Real Time Tomography for providing the reconstruction software, Ms. Kristen Lau for her support during the acquisition of images, and the team of medical physicists who volunteered for participating in the 2-AFC experiment. ADAM is a member of the scientific advisory board, and a shareholder of RTT.

REFERENCES

- [1] C. I. Lee, M. Cevik, O. Alagoz, B. L. Sprague, A. N. Tosteson, D. L. Miglioretti, K. Kerlikowske, N. K. Stout, J. G. Jarvik, S. D. Ramsey *et al.*, "Comparative effectiveness of combined digital mammography and tomosynthesis screening for women with dense breasts," *Radiology*, vol. 274, no. 3, pp. 772–780, 2014.
- [2] F. J. Gilbert, L. Tucker, M. G. Gillan, P. Willsher, J. Cooke, K. A. Duncan, M. J. Michell, H. M. Dobson, Y. Y. Lim, T. Suaris *et al.*, "Accuracy of digital breast tomosynthesis for depicting breast cancer subgroups in a UK retrospective reading study (TOMMY trial)," *Radiology*, vol. 277, no. 3, pp. 697–706, 2015.
- [3] R. G. Roth, A. D. Maidment, S. P. Weinstein, S. O. Roth, and E. F. Conant, "Digital breast tomosynthesis: lessons learned from early clinical implementation," *Radiographics*, vol. 34, no. 4, pp. E89–E102, 2014.
- [4] S. S. J. Feng and I. Sechopoulos, "Clinical digital breast tomosynthesis system: dosimetric characterization," *Radiology*, vol. 263, no. 1, pp. 35–42, 2012.
- [5] T. Svahn, N. Houssami, I. Sechopoulos, and S. Mattsson, "Review of radiation dose estimates in digital breast tomosynthesis relative to those in two-view full-field digital mammography," *The Breast*, vol. 24, no. 2, pp. 93–99, 2015.
- [6] International Atomic Energy Agency, "Appendix II: Medical exposure," in *International Basic Safety Standards for Protection against Ionizing Radiation and for the Safety of Radiation Sources*, 1996, pp. 45–56.
- [7] I. Sechopoulos and C. Ghetti, "Optimization of the acquisition geometry in digital tomosynthesis of the breast," *Med. Phys.*, vol. 36, no. 4, pp. 1199–1207, 2009.
- [8] H. Machida, T. Yuhara, T. Mori, E. Ueno, Y. Moribe, and J. M. Sabol, "Optimizing parameters for flat-panel detector digital tomosynthesis," *RadioGraphics*, vol. 30, no. 2, pp. 549–562, 2010, PMID: 20228334. [Online]. Available: <http://dx.doi.org/10.1148/rg.302095097>
- [9] L. R. Borges, P. R. Bakic, A. Foi, A. D. A. Maidment, and M. A. C. Vieira, "Pipeline for effective denoising of digital mammography and digital breast tomosynthesis," in *Proc. SPIE Medical Imaging 2017: Physics of Medical Imaging*, vol. 10132, no. 1013206, 2017. [Online]. Available: <http://dx.doi.org/10.1117/12.2255058>
- [10] T. Wu, R. H. Moore, E. A. Rafferty, and D. B. Kopans, "A comparison of reconstruction algorithms for breast tomosynthesis," *Med. Phys.*, vol. 31, no. 9, pp. 2636–2647, 2004.
- [11] E. Y. Sidky, X. Pan, I. S. Reiser, R. M. Nishikawa, R. H. Moore, and D. B. Kopans, "Enhanced imaging of microcalcifications in digital breast tomosynthesis through improved image-reconstruction algorithms," *Med. Phys.*, vol. 36, no. 11, pp. 4920–4932, 2009.
- [12] A. Svalkvist and M. Båth, "Simulation of dose reduction in tomosynthesis," *Med. Phys.*, vol. 37, no. 1, pp. 258–269, 2010. [Online]. Available: <http://dx.doi.org/10.1118/1.3273064>
- [13] A. Mackenzie, D. R. Dance, A. Workman, M. Yip, K. Wells, and K. C. Young, "Conversion of mammographic images to appear with the noise and sharpness characteristics of a different detector and x-ray system," *Med. Phys.*, vol. 39, no. 5, pp. 2721–2734, 2012.
- [14] A. Mackenzie, D. R. Dance, O. Diaz, and K. C. Young, "Image simulation and a model of noise power spectra across a range of mammographic beam qualities," *Med. Phys.*, vol. 41, no. 12, p. 121901, 2014.
- [15] E. Samei, R. S. Saunders Jr, J. A. Baker, and D. M. Delong, "Digital mammography: Effects of reduced radiation dose on diagnostic performance 1," *Radiology*, vol. 243, no. 2, pp. 396–404, 2007.
- [16] R. S. Saunders, J. A. Baker, D. M. Delong, J. P. Johnson, and E. Samei, "Does image quality matter? Impact of resolution and noise on mammographic task performance," *Med. Phys.*, vol. 34, no. 10, pp. 3971–3981, 2007.
- [17] L. R. Borges, M. A. da Costa Vieira, and A. Foi, "Unbiased injection of signal-dependent noise in variance-stabilized range," *IEEE Signal Proc. Lett.*, vol. 23, no. 10, pp. 1494–1498, Oct 2016.
- [18] L. R. Borges, H. C. de Oliveira, P. F. Nunes, P. R. Bakic, A. D. Maidment, and M. A. Vieira, "Method for simulating dose reduction in digital mammography using the Anscombe transformation," *Med. Phys.*, vol. 43, no. 6, pp. 2704–2714, 2016.
- [19] L. R. Borges, I. Guerrero, P. R. Bakic, A. D. Maidment, H. Schiabel, and M. A. Vieira, "Simulation of dose reduction in digital breast tomosynthesis," in *International Workshop on Digital Mammography*. Springer, 2016, pp. 343–350.
- [20] I. Sechopoulos, "A review of breast tomosynthesis. Part I. The image acquisition process," *Med. Phys.*, vol. 40, no. 1, p. 014301, 2013.
- [21] S. Vedantham, A. Karellas, G. R. Vijayaraghavan, and D. B. Kopans, "Digital breast tomosynthesis: state of the art," *Radiology*, vol. 277, no. 3, pp. 663–684, 2015.
- [22] N. H. Marshall, "Calculation of quantitative image quality parameters," NHSBSP Equipment Report 0902, 2009.
- [23] I. Cunningham, "Applied linear-system theory," in *Handbook of Medical Imaging: Physics and Psychophysics*, R. Van Metter, J. Beutel, and H. Kundel, Eds. SPIE, 2000, pp. 79–155.
- [24] J. Lee and K. Hoppel, "Noise modeling and estimation of remotely-sensed images," in *1989 IEEE Int. Geoscience and Remote Sensing Symposium (IGARSS'89)*, vol. 2, 1989, pp. 1005–1008.
- [25] A. Foi, M. Trimeche, V. Katkovnik, and K. Egiazarian, "Practical Poissonian-Gaussian noise modeling and fitting for single-image raw-data," *IEEE T. Image Process.*, vol. 17, no. 10, pp. 1737–1754, 2008.
- [26] N. Acito, M. Diani, and G. Corsini, "Signal-dependent noise modeling and model parameter estimation in hyperspectral images," *IEEE T Geosci. Remote*, vol. 49, no. 8, pp. 2957–2971, 2011.
- [27] A. Foi. (2016) Signal-dependent noise modeling, estimation, and removal for digital sensors. [Online]. Available: www.cs.tut.fi/~foi/sensornoise
- [28] F. J. Anscombe, "The transformation of Poisson, binomial and negative-binomial data," *Biometrika*, vol. 35, no. 3/4, pp. 246–254, 1948.
- [29] K. Young and J. Oduko, "Technical evaluation of the Hologic Selenia full-field digital mammography system with a tungsten tube," *NHS Cancer Screening Programmes*, 2008.
- [30] J. T. Dobbins III, "Image quality metrics for digital systems," in *Handbook of Medical Imaging: Physics and Psychophysics*, R. Van Metter, J. Beutel, and H. Kundel, Eds. SPIE, 2000, pp. 79–155.
- [31] P. Massoumzadeh, S. Don, C. F. Hildebolt, K. T. Bae, and B. R. Whiting, "Validation of CT dose-reduction simulation," *Med. Phys.*, vol. 36, no. 1, pp. 174–189, 2009.
- [32] L. Cockmartin, P. R. Bakic, H. Bosmans, A. D. Maidment, H. Gall, M. Zerhouni, and N. W. Marshall, "Power spectrum analysis of an anthropomorphic breast phantom compared to patient data in 2D digital mammography and breast tomosynthesis," in *International Workshop on Digital Mammography*. Springer, 2014, pp. 423–429.
- [33] D. D. Pokrajac, A. D. Maidment, and P. R. Bakic, "Optimized generation of high resolution breast anthropomorphic software phantoms," *Med. Phys.*, vol. 39, no. 4, pp. 2290–2302, 2012.
- [34] M. Yaffe, "Digital mammography," in *Handbook of Medical Imaging: Physics and Psychophysics*, R. Van Metter, J. Beutel, and H. Kundel, Eds. SPIE, 2000, pp. 329–372.
- [35] S. S. Shapiro and M. B. Wilk, "An analysis of variance test for normality (complete samples)," *Biometrika*, vol. 52, no. 3/4, pp. 591–611, 1965.
- [36] D. Zwick and D. L. Brothers, "RMS granularity: Determination of just noticeable differences," *Photogr. Sci. Eng.*, vol. 19, no. 4, pp. 235–238, 1975.
- [37] L. Azzari and A. Foi, "Variance stabilization in Poisson image deblurring," in *Proc. 2017 IEEE Int. Sym. Biomedical Imaging (ISBI)*, Melbourne, Australia, 2017.

Paper 5: Pipeline for effective denoising of digital mammography and digital breast tomosynthesis

Copyright 2017 Society of Photo Optical Instrumentation Engineers. One print or electronic copy may be made for personal use only. Systematic reproduction and distribution, duplication of any material in this paper for a fee or for commercial purposes, or modification of the content of the paper are prohibited. <http://dx.doi.org/10.1117/12.2255058>

Pipeline for effective denoising of digital mammography and digital breast tomosynthesis

Lucas R. Borges^{a,b}, Predrag R. Bakic^b, Alessandro Foi^c, Andrew D. A. Maidment^b,
and Marcelo A. C. Vieira^a

^aDepartment of Electrical and Computer Engineering, University of São Paulo, São Carlos, Brazil

^bDepartment of Radiology, University of Pennsylvania, Philadelphia, United States

^cDepartment of Signal Processing, Tampere University of Technology, Tampere, Finland

ABSTRACT

Denoising can be used as a tool to enhance image quality and enforce low radiation doses in X-ray medical imaging. The effectiveness of denoising techniques relies on the validity of the underlying noise model. In full-field digital mammography (FFDM) and digital breast tomosynthesis (DBT), calibration steps like the detector offset and flat-fielding can affect some assumptions made by most denoising techniques. Furthermore, quantum noise found in X-ray images is signal-dependent and can only be treated by specific filters. In this work we propose a pipeline for FFDM and DBT image denoising that considers the calibration steps and simplifies the modeling of the noise statistics through variance-stabilizing transformations (VST). The performance of a state-of-the-art denoising method was tested with and without the proposed pipeline. To evaluate the method, objective metrics such as the normalized root mean square error (N-RMSE), noise power spectrum, modulation transfer function (MTF) and the frequency signal-to-noise ratio (SNR) were analyzed. Preliminary tests show that the pipeline improves denoising. When the pipeline is not used, bright pixels of the denoised image are under-filtered and dark pixels are over-smoothed due to the assumption of a signal-independent Gaussian model. The pipeline improved denoising up to 20% in terms of spatial N-RMSE and up to 15% in terms of frequency SNR. Besides improving the denoising, the pipeline does not increase signal smoothing significantly, as shown by the MTF. Thus, the proposed pipeline can be used with state-of-the-art denoising techniques to improve the quality of DBT and FFDM images.

Keywords: Variance stabilization, denoising, full field digital mammography, digital breast tomosynthesis

1. INTRODUCTION

Full-field digital mammography (FFDM) and digital breast tomosynthesis (DBT) are the most common imaging modalities used for breast cancer screening programs. In breast cancer screening programs, asymptomatic women are exposed to low doses of X-ray radiation. Thus, to guarantee the safety of the patients, the International Basic Safety Standards for Protection against Ionizing Radiation and for the Safety of Radiation Sources instructs that radiation exposures must "...be the minimum necessary to achieve the required diagnostic objective..." [1]. To improve image quality and maintain low radiation levels, a number of authors have investigated the advantages and limitations of applying denoising algorithms to FFDM and DBT images [2] [3] [4]. The common hypothesis of these works is that denoising can improve cancer detection by suppressing the image noise.

The effectiveness of denoising algorithms relies on the correct modeling of the noise statistics. Specifically, the noise found in FFDM and DBT images can be described by a Gaussian-Poisson model. The Gaussian portion describes additive fluctuations of the pixel value which can be caused by, *e.g.*, electronic and thermal noise. The Poisson model accounts for quantum noise, which is inherent to the process of photon generation and detection.

To facilitate the process of noise modeling, a common approach is to use raw images as input for the denoising methods. Although the raw images are the crudest data reported by clinical equipment, some post-processing steps related to detector calibration are incorporated; these must be considered during the denoising process. For example, properties such as the inverse square law and heel effect negatively affect the uniformity of the field, and are frequently compensated by changes in the detector gain (flat-field correction) [5]. Another example of calibration is the pixel offset. The offset is applied to ensure the non-negativity of the pixels. This offset affects the linearity between entrance dose and overall pixel signal.

Additionally, quantum noise is signal-dependent. Many of the best denoising methods in the literature are designed assuming signal-independent Gaussian noise [6] [7]. Mathematical tools such as variance-stabilizing transformations (VST) are capable of eliminating the dependency between noise and signal. If properly applied, these are powerful tools that may be used for denoising FFDM and DBT images.

Therefore, it is essential to prepare the data correctly and choose appropriate tools before denoising FFDM and DBT images. In this work, we propose a pipeline for FFDM and DBT denoising that considers the calibration steps and allows easy modeling of the noise statistics through variance stabilization transformations. Using the proposed pipeline, it is possible to successfully process FFDM and DBT images using any denoising technique designed for Gaussian signal-independent noise.

2. NOISE MODEL & PROBLEM DEFINITION

Consider $z^o(i, j)$ as pixels from a raw (“for processing”) FFDM image or from a raw DBT projection, where (i, j) are spatial coordinates. We model $z^o(i, j)$ as

$$z^o(i, j) = \alpha(i, j)\mathcal{P}(y(i, j)) + \sigma_E\eta + \tau, \quad (1)$$

where $\alpha(i, j)$ are spatially varying detector gain, $\mathcal{P}(y(i, j))$ indicates a Poisson-distributed variate with parameter $y(i, j)$, $y(i, j)$ is the underlying noise-free signal, σ_E is the standard deviation of the electronic noise, η is signal-independent random noise with zero mean and unit variance and τ is the constant signal offset. The conditional expectation and variance of $z^o(i, j)$ given $y(i, j)$ are:

$$E\{z^o(i, j)|y(i, j)\} = \alpha(i, j)y(i, j) + \tau, \quad \text{var}\{z^o(i, j)|y(i, j)\} = \alpha^2(i, j)y(i, j) + \sigma_E^2, \quad (2)$$

The detector gain $\alpha(i, j)$ and the detector offset τ describe the quantum gain and the modifications on the signal due to the calibration steps that are performed prior to the storage of the raw DICOM file. The quantum gain results from the uncertainties related to x-ray generation, transmission and detection; and the calibration is responsible for the correction of non-uniformities caused by properties such as the heel effect, inverse square law, and dark currents (flat-fielding).

Note that the variance of z^o depends on the electronic noise $\sigma_E\eta$ and also on the underlying signal $y(i, j)$ and detector gain $\alpha(i, j)$, which are spatially dependent. The goal of this work is to obtain an estimate $\hat{z}^o(i, j)$ of the noiseless calibrated signal using the raw data $z^o(i, j)$.

3. MATERIALS & METHODS

Many state-of-the-art denoising algorithms assume input signals contaminated with signal-independent Gaussian noise. This assumption limits the choice of denoising filters that can effectively be applied to FFDM and DBT images. To overcome this issue, we use variance-stabilizing transformations (VST) to convert a signal-dependent variable into an approximately Gaussian signal-independent variable, thereby increasing the number of filtering algorithms that can be used. One well-known VST for Poisson-Gaussian variables is the generalized Anscombe transformation (GAT) [8]. However, to correctly stabilize the noise, the calibration parameters $\alpha(i, j)$ and τ must be estimated and removed from $z^o(i, j)$ prior to the application of the VST.

Thus, before denoising the raw data we propose to use a pipeline with two preliminary steps: calibration removal and variance stabilization. In the former step, the image is linearized and the quantum gain is removed. The latter step consists of choosing an appropriate variance stabilization transform that converts a mixture of Gaussian-Poisson distributions into a signal-independent Gaussian distribution. It is important to emphasize that the appropriate inverse transform must be applied after denoising, and the image must be recalibrated. Figure 1 presents an overview of the proposed pipeline.

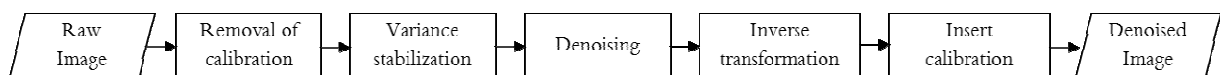


Figure 1. Overall schematic of the proposed pipeline.

3.1. Calibration removal

The goal of this section is to estimate the uncalibrated signal from the available raw image $z^o(i, j)$. Trivially, we can define the uncalibrated signal as:

$$S(i, j) = \frac{z^o(i, j) - \tau}{\alpha(i, j)}. \quad (3)$$

Therefore, to obtain the uncalibrated noisy signal $S(i, j)$ it is necessary to estimate the pixel offset τ and the pixel gain $\alpha(i, j)$. The constant τ can be estimated in various ways. We adopted the method defined by the National Health Service Breast Screening Programme (NHSBSP) [9]. An alternative method for calculating τ consists of acquiring dark-field images.

Next, we estimate the detector gain $\alpha(i, j)$. The best way to obtain $\alpha(i, j)$ would be by accessing the calibration data of the clinical system. However, this information is not always available and thus has to be estimated from acquired images. To this end, we first express the underlying signal $y(i, j)$ as a function of the expectation of $z^o(i, j)$, starting from equation (2):

$$y(i, j) = \frac{E\{z^o(i, j)|y(i, j)\} - \tau}{\alpha(i, j)}. \quad (4)$$

Then, substituting equation (4) into the variance defined in equation (2), we obtain:

$$\alpha(i, j) = \frac{\text{var}\{z^o(i, j)|y(i, j)\} - \sigma_E^2}{E\{z^o(i, j)|y(i, j)\} - \tau}. \quad (5)$$

The variance σ_E^2 of the signal-dependent noise can be estimated using tools described in the literature [10], as explained in the results section. The total noise variance of the calibrated signal $\text{var}\{z^o(i, j)|y(i, j)\}$ and the expectation of the calibrated signal $E\{z^o(i, j)|y(i, j)\}$ can both be estimated from uniform calibration images. Therefore, a good approximation of $\alpha(i, j)$ can be found using equation (5). Finally, $S(i, j)$ can be estimated using the relation defined by equation (3).

3.2. Variance-stabilizing transformation (VST)

Variance-stabilizing transformations are mathematical tools capable of converting signal-dependent noise distributions into signal-independent noise with an approximately Gaussian shape and constant variance. For Poisson-Gaussian data, a common transformation is the generalized Anscombe transformation (GAT), defined by [8]. For observations such as the uncalibrated signal $S(i, j)$, the GAT is defined as

$$\mathcal{A}(S(i, j)) = 2 \sqrt{S(i, j) + \frac{3}{8} + \sigma_E^2}, \quad (6)$$

where $\mathcal{A}(S(i, j))$ is the stabilized signal, which can be modeled as corrupted exclusively by standard Gaussian noise, $\mathcal{N}(0, 1)$. Denoising can finally be applied to the signal, and the denoised image can be recovered by applying the appropriate inverse transformation. The image is then recalibrated by multiplying the signal by the estimated $\alpha(i, j)$ matrix and adding τ .

3.3. Denoising

After stabilization of the variance, we treat the noise as additive independent Gaussian white noise with known variance. In particular, in the case of the generalized Anscombe VST, the variance is unitary. Many denoising methods are suitable for this standard type of noise degradation. A review of the most significant approaches can be found, e.g., in [11] [12]. For the purpose of the present work, we utilize the popular BM3D denoising algorithm [7]. This highly competitive algorithm synergistically combines three important elements found in many modern image filters:

A) *The use of patch-based estimates*, i.e. a redundant image representation composed of multiple overlapping small patches or blocks;

B) *The use of nonlocal self-similarity as a regularization prior*, i.e. leveraging the fact that natural images contain a large number of mutually similar patches at different locations and that noise can be attenuated by adaptively enforcing the mutual similarity between patches;

C) *Transform-domain sparsity*, i.e. the fact that natural signals enjoy a compact representation with respect to suitable decorrelating transforms (e.g., discrete cosine or wavelets) where most of the energy is concentrated in few large-magnitude coefficients within the transform spectrum, and where regularization can be effectively implemented by shrinkage (e.g., hard thresholding) of the spectrum.

Specifically, BM3D represents the image through a collection of spectra of all groups of mutually similar patches by stacking the mutually similar image blocks into 3D data arrays, and by applying a 3-D decorrelating transform to these groups, BM3D achieves an enhanced sparse and redundant representation of the image. The inverse 3D transformation of a shrunk group spectrum yields a group of jointly filtered image patches. Each pixel in the image is then estimated by a multitude of filtered patches, which are finally combined via an adaptive averaging procedure (so-called aggregation) to yield the final image estimate.

3.4. Inverse VST

The denoised image d , obtained after variance stabilization, has to undergo an inverse VST transformation to match the range of S . For this task, we use the exact unbiased inverse of the generalized Anscombe transform \mathcal{A}_{EUI}^{-1} , as proposed in [13]:

$$\mathcal{A}_{EUI}^{-1}(d) = \frac{1}{4}d^2 + \frac{1}{4}\sqrt{\frac{3}{2}}d^{-1} - \frac{11}{8}d^{-2} + \frac{5}{8}\sqrt{\frac{3}{2}}d^{-3} - \frac{1}{8} - \sigma_E^2 \quad (7)$$

The need for this particular inverse stems from the fact that the forward VST is necessarily a nonlinear mapping, which thus does not commute with the mathematical expectation: $E\{\mathcal{A}(S)|y\} = \mathcal{A}(E\{S|y\})$. The inverse [13] is specially designed so that $\mathcal{A}_{EUI}^{-1}(E\{\mathcal{A}(S)|y\}) = E\{S|y\}$, exactly, and for any y . Therefore, applying \mathcal{A}_{EUI}^{-1} to the output of BM3D is justified as soon as we consider that, formally, denoising of $\mathcal{A}(S)$ aims to approximate the conditional expectation $d \approx E\{\mathcal{A}(S)|y\}$. We refer the reader to [13] for more details on the optimal statistical properties of \mathcal{A}_{EUI}^{-1} .

3.5. Metrics

To assess the performance of the proposed pipeline, objective metrics were calculated before denoising, after denoising without the proposed pipeline, and after denoising with the proposed pipeline. The normalized root mean square error (N-RMSE) was used to evaluate the performance of the method in the spatial domain. We adopted the root mean square error normalized by the signal standard deviation:

$$NRMSE(a, r) = \frac{1}{\sigma_{gt}} \sqrt{\frac{1}{MN} \sum_{i=1}^M \sum_{j=1}^N (a(i, j) - r(i, j))^2}, \quad (8)$$

where σ_{gt} is the standard deviation of the signal, $r(i, j)$ are pixels from a reference noiseless image, $a(i, j)$ are the pixels from the image being evaluated, M and N are image dimensions. As our noise model is signal-dependent, we present the improvements in the N-RMSE as a function of the gray level.

The second objective metric used was the normalized power spectrum of the residual noise (NNPS) [5], which evaluates the noise in terms of frequency components. The NNPS is widely used as a quality metric. We also analyzed the signal smoothing caused by the denoising method. For this purpose, we compare the modulation transfer function (MTF) [5] estimated from the denoised images.

Lastly, we estimated the efficiency of the denoising pipeline in terms of the signal-to-noise ratio as a function of spatial frequency. We define the frequency SNR as:

$$SNR_{dB}(u) = 10 \log_{10} \left(\frac{MTF^2(u)}{NNPS(u)} \right), \quad (9)$$

where u are frequency components. The results show the relative improvement in SNR.

3.6. Images

To assess the performance of the proposed pipeline, sets of FFDM and DBT images were acquired using a clinical imaging system Selenia Dimensions (Hologic, Bedford, MA) at the Hospital of the University of Pennsylvania. We chose to perform all tests using a 3D anthropomorphic breast phantom [14] [15]. The phantom allows the acquisition of several instances, facilitating the estimation of the noiseless signal necessary to calculate some of the objective metrics.

The anthropomorphic phantom was prototyped by CIRS, Inc. (Reston, VA) under license of the University of Pennsylvania. It consists of six slabs, each containing simulated anatomical structures manufactured using tissue mimicking materials, based upon a realization of the companion breast software phantom [16]. The phantom simulates a 450 ml breast, compressed to 5 cm, with 17% volumetric breast density (excluding the skin). In addition to the normal breast anatomy, individual pieces of calcium oxalate (99%, Alfa Aesar, Ward Hill, MA), with different sizes were placed between slabs of the phantom to mimic a cluster of microcalcifications. Figure 2 shows a photograph of all the slabs of the anthropomorphic breast phantom used in this study, an example of a FFDM acquisition, and the central slice of a DBT reconstructed image.

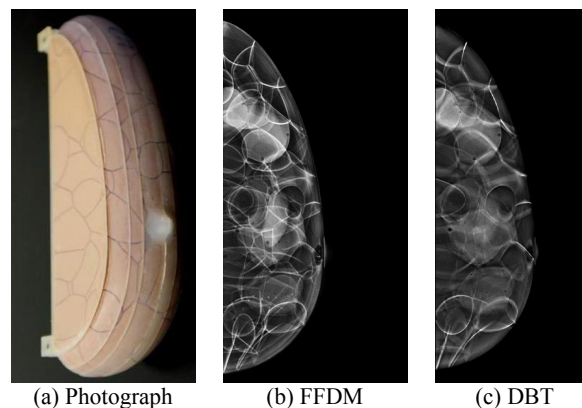


Figure 2. Anthropomorphic phantom used for validation.

First, one FFDM of the phantom was acquired using the automatic exposure control mode (AEC). This exposure was used to define the optimal acquisition settings for the phantom composition (29 kVp, 160 mAs). Next, the acquisition was switched to manual mode and 15 images were acquired using the exposure settings given by the AEC. The current-time product (mAs) was then decreased from the AEC value (160 mAs) to 120 mAs and 80 mAs to simulate lower radiation levels. Five images were acquired at each dose.

Sets of DBT images were also acquired using the same equipment. Again, one exposure was performed to define the optimal exposure parameters, followed by the manual acquisition of 15 sets of DBT projections at the configuration given by the AEC (31 kVp/60 mAs), and 5 additional sets of reduced dose images were acquired at 42 mAs and 30 mAs. For both modalities, an approximation of the noiseless image was calculated by averaging ten acquisitions at the highest dose level.

As mentioned in the previous section, the MTF was used as a measurement for evaluation of signal smoothing. The MTF is commonly calculated using a highly attenuating uniform object positioned over a uniform background, which results on a high contrast step used to estimate the MTF. However, the denoising algorithm proposed in this work takes advantage of the self-similarities found in the input image. Thus, denoising such uniform images and calculating the MTF would yield good results, but it would not represent the real performance of the pipeline in a real application. To

simulate the real denoising performance, metal features were inserted between slabs of the anthropomorphic phantom. This configuration results in images with real structured background that forces the pipeline to perform a challenging denoising task, but at the same time allows the estimation of the MTF using the border of the metal feature. Figure 3 shows ROIs containing the metal inserts used to estimate the MTF.

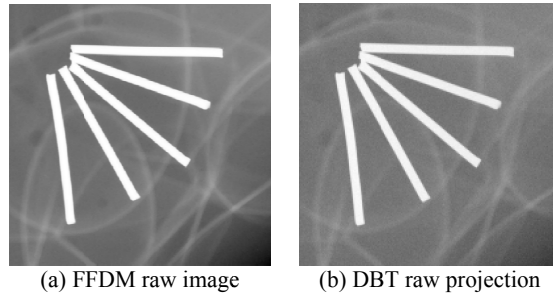


Figure 3. Metal inserts used to calculate the MTF.

The estimation of the calibration parameters requires a set of uniform images acquired with the same equipment as used for the acquisition of the FFDM and DBT input images. For this purpose, we created a pool of uniform images using a 45 mm poly methyl methacrylate (PMMA) block, commonly used for flat-felding the system. Uniform FFDM images were acquired at the following entrance air kerma: 5.86 mGy, 5.14 mGy, 4.41 mGy and 2.93 mGy. Also, uniform DBT projections were acquired at entrance air kerma of 5.46 mGy, 4.65 mGy, 3.83 mGy and 2.74 mGy.

4. RESULTS & DISCUSSION

4.1 Estimation of detector offset τ

The NHSBSP method [9], which we adopt to estimate the detector offset, consists of acquiring a set of uniform images at a range of current-time products and calculating the mean pixel value (MPV) inside a 100 mm square ROI positioned at the midline, 60 mm from the chest wall. The relation between the detector entrance surface air kerma and MPV is fitted to an affine function, and the MPV at zero air kerma is the estimated τ . Details can be found in [9]. The estimated τ_{FFDM} was 42, and τ_{DBT} was 58.

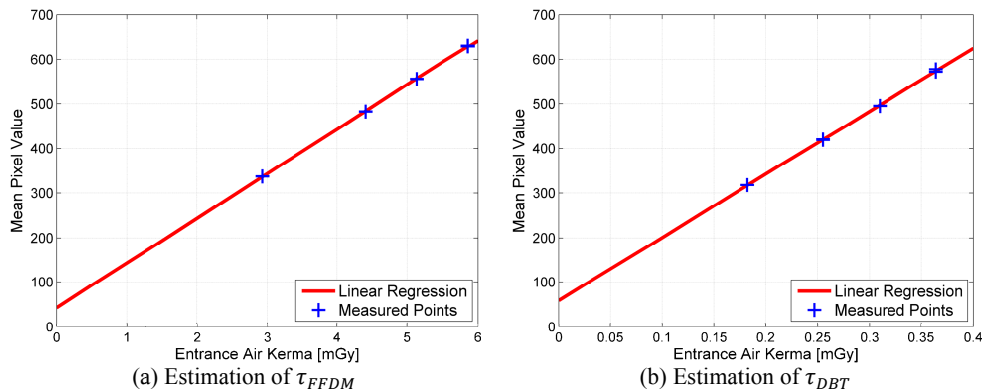


Figure 4. Linear regressions used to estimate the pixel offset.

4.2. Estimation of electronic noise σ_E^2 and detector gain $\alpha(i, j)$

As defined by equation (5), an initial estimation of σ_E^2 is required to estimate the detector gain $\alpha(i, j)$. For this purpose, we use software [10] available for download at the authors' website [17]. The program can estimate the standard deviation of the additive portion of a Gaussian-Poisson mixture provided that the pixel gain $\alpha(i, j)$ is constant through the field. To meet this requirement, we selected a rectangular ROI with a short span along the chest-nipple direction

(14 mm) and a much longer span along the orthogonal direction (140 mm). Using this elongated layout, we take advantage of the fact that the pixel gain varies more slowly on the orthogonal direction than in the chest-nipple direction. The ROI was taken from 15 realizations of the high dose images after the subtraction of τ . For DBT images, the estimation was performed on the 15 central projections, perpendicular to the field.

The estimated σ_E^2 was 1.8 ± 0.4 for FFDM images, and 7.2 ± 1.3 for DBT images. Note that the variance of the electronic noise estimated from the DBT projection is four times the variance estimated from the FFDM image. This relationship is consistent with the theory, as the DBT system used in this work uses the same detector as used for FFDM, but it performs 2×2 pixel binning. Therefore, DBT images are expected to report electronic noise four times higher.

The pixel gain was estimated via equation (5) using the uniform images acquired with the AEC mode. Figure 5 shows the estimated $\alpha(i, j)$ for each spatial position. Note that, as mentioned before, $\alpha(i, j)$ has more relevant changes in the chest wall to nipple direction, than in the orthogonal direction.

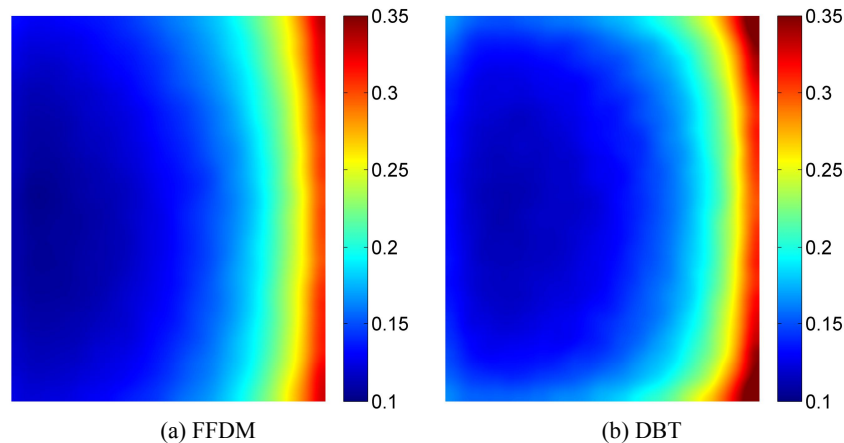


Figure 5. Spatially dependent detector gain $\alpha(i, j)$.

4.3. Variance Stabilization

After the calibration was removed following the previous steps, it is possible to stabilize the noise variance using the VST defined by (6). Figure 6 visualizes the local standard deviation calculated using a ROI positioned inside the breast with the AEC acquisition. Note that before stabilization the standard deviation spans a wide range, and is signal dependent as noticed by the presence of structures inherent in the images. Figures 6 (b) and (d) show that the signal-dependency is removed after the VST is applied. Note that, not only the noise is stabilized, but also that the standard deviation is unity. The average of the standard deviation shown in Figure 6 (b) is 1.01, and in Figure 6 (d) is 1.07. Furthermore, we would like to emphasize that the signal-dependency of the noise is much more evident on FFDM images, although it can also be noticed in the DBT image. This shows that the signal-independent electronic noise has higher relative strength on DBT images compared to FFDM. This can be explained by the 2×2 binning performed by the DBT system, and by the fact that DBT images have lower overall signal due to the lower radiation used at each projection.

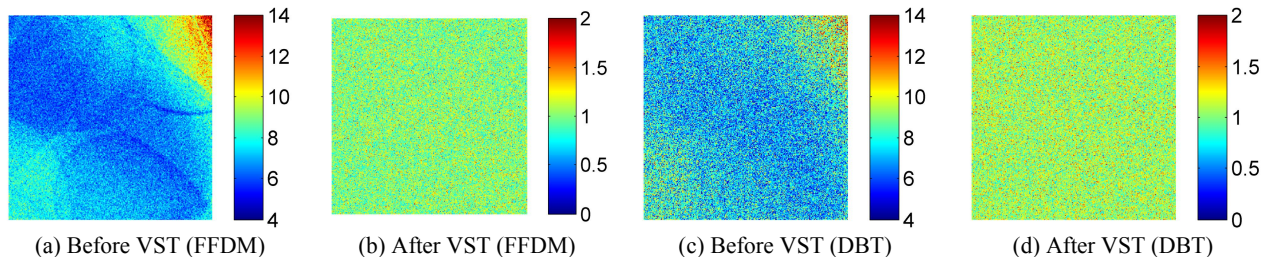


Figure 6. Standard deviation of FFDM and DBT images before (a,c), and after (b,d) variance stabilization.

4.4. Denoising

Figure 7 shows a magnified portion of the ROI taken from FFDM and DBT images acquired with the AEC configuration, for visual comparison. Figure 7 also shows the pixel profile taken from the region indicated by the lines.

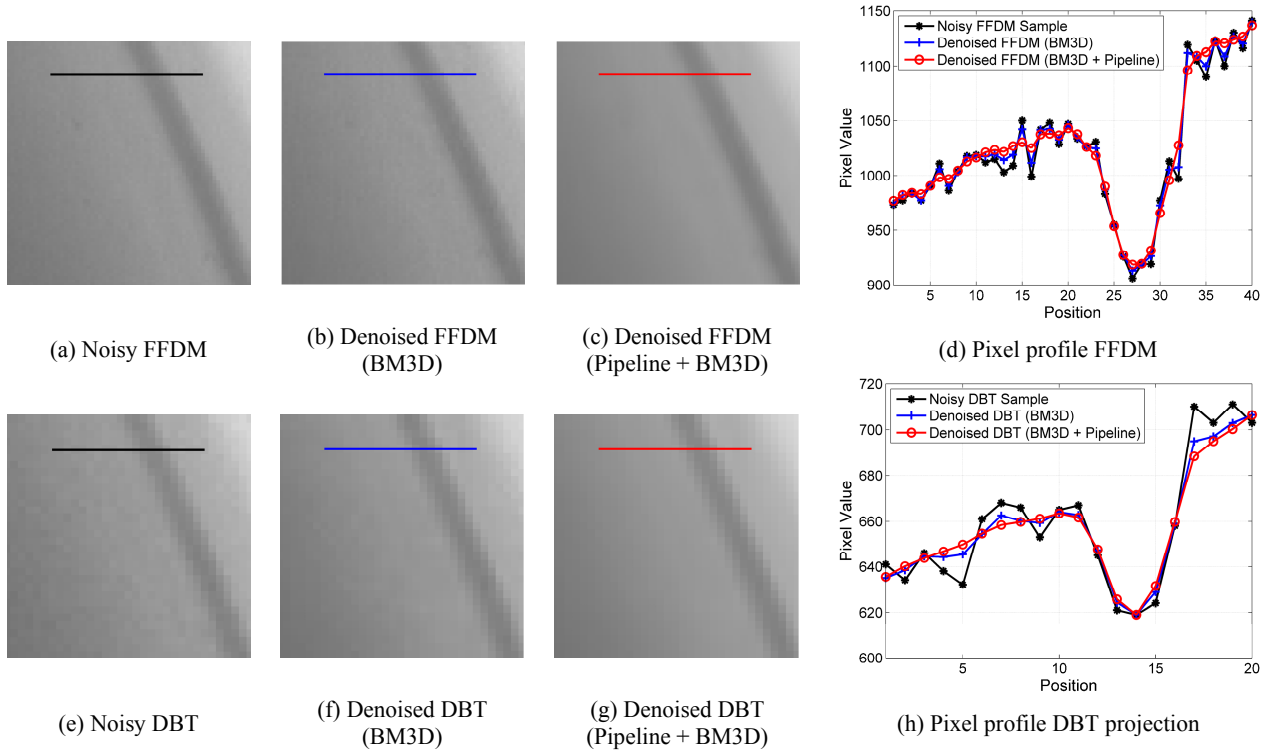


Figure 7. Magnified view of a bright area from FFDM and DBT images, and the pixel profile of the region indicated by the line.

As shown by Figure 7, the pipeline improved the denoising process enough to be appreciated visually, and on the line profiles. Figure 8 shows the standard deviation of the residual noise after denoising is performed with and without the pipeline for each pixel. The results show that the proposed pipeline improves the denoising in regions with bright pixels. As the noise is signal-dependent, dark regions are over-smoothed and bright pixels are under-filtered, due to the assumption of signal-independent noise. The DBT results were calculated from the central projection.

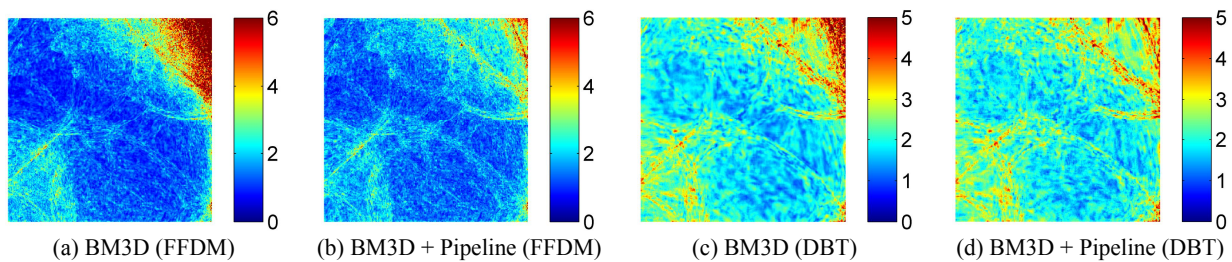


Figure 8. Standard deviation of the residual noise after denoising is performed.

Visual comparison between Figures 6 and 8, with special attention to the color scale, makes evident the potential of the denoising technique chosen in this work. Even with an incorrect noise model, the filter was capable of suppressing a large portion of the noise when the pipeline is not used. However, bright areas such as the top-right corner have higher residual noise when the pipeline is not used.

Since the denoising strength depends on the mean pixel value, in Figure 9 we present the relative improvement on N-RMSE as a function of underlying gray level. Again, results show that bright pixels were not filtered effectively when the pipeline is not applied. The use of the variance-stabilizing transformation improved denoising in those areas.

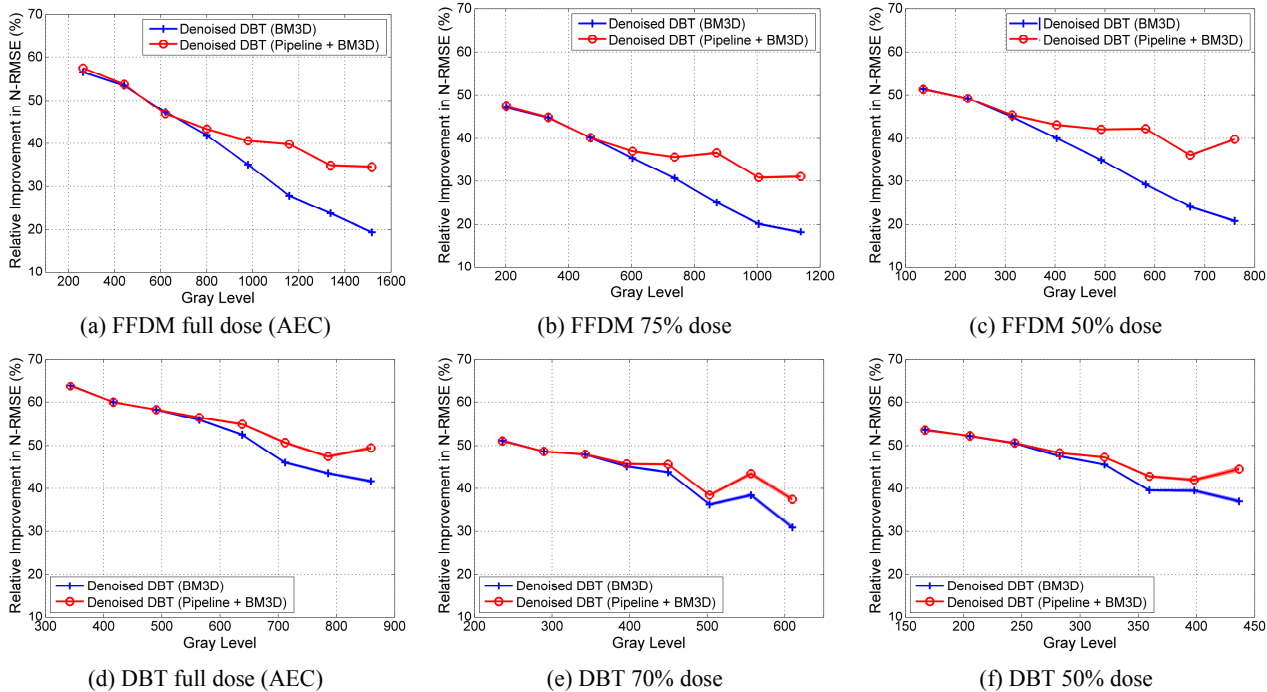


Figure 9. N-RMSE and relative improvement in N-RMSE of each method at different entrance dose levels.

Next, the normalized noise power spectrum of the residual noise was calculated, Figure 10 shows the results. Note that the denoising successfully suppressed the noise components especially at high frequencies.

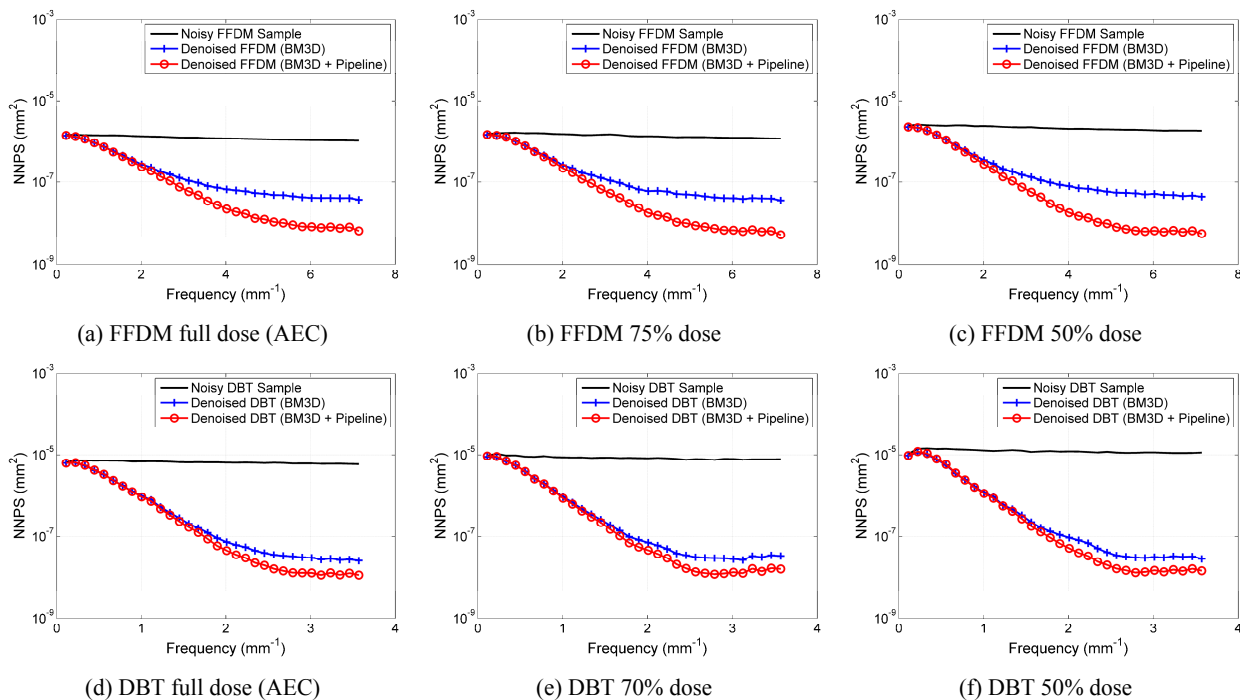


Figure 10. Normalized power spectrum of the residual noise from denoised images at different dose levels.

In general, the denoising process consists of a compromise between noise removal and signal smoothing. Therefore, Figure 11 presents the MTF calculated from denoised images. The MTF was calculated using the anthropomorphic phantom with inserted metal features, which generates high contrast borders.

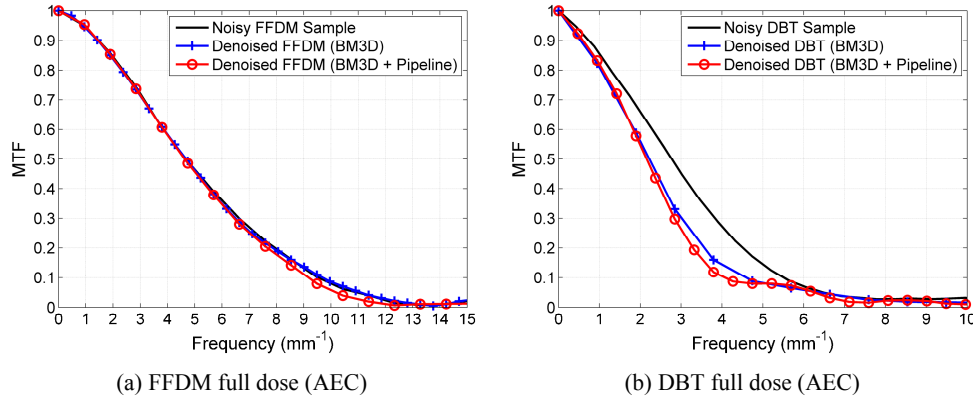


Figure 11. Modulation transfer function of the noisy and denoised images acquired with the AEC mode.

Note that, even though the noise was successfully suppressed in FFDM images, the MTF is preserved. The pipeline improved the denoising in comparison to the BM3D alone with no changes to the MTF. The denoising of DBT images caused a slight drop of the MTF. As DBT projections are acquired at lower radiation levels, they require more aggressive denoising compared to FFDM images, which may justify the slight drop in the MTF.

Lastly, Figure 12 shows the relative improvement of the SNR at the frequency domain. This measurement represents the tradeoff between signal blur and noise suppression.

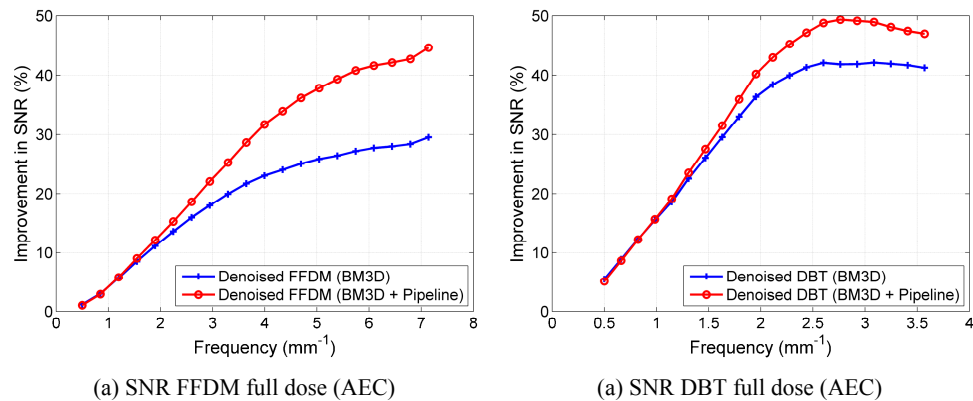


Figure 12. Signal-to-noise ratio as a function of spatial frequency.

Figure 12 shows that the pipeline improves the efficiency of the denoising algorithm. Note that the denoising method is more efficient at suppressing the mid and high frequency noise.

5. CONCLUSION

In this work we investigated the feasibility of a pre-processing pipeline for image denoising. The pipeline is compatible with any denoising technique that assumes additive Gaussian noise. The results support the application of the pipeline, which is especially valuable for FFDM images. Denoising was performed more effectively with the pipeline, showing no relevant detriment to the signal sharpness, as indicated by the MTF. Thus, the efficiency of the denoising was improved, as shown by the relation between signal blur and noise suppression.

ACKNOWLEDGEMENT

This work was supported by the São Paulo Research Foundation (FAPESP), by the Brazilian Foundation for the Coordination of Improvement of Higher Education Personnel (CAPES grant no. 88881.030443/2013-01) and by the Academy of Finland (project no. 252547).

REFERENCES

- [1] International Atomic Energy Agency, "Appendix II: Medical exposure," in *International Basic Safety Standards for Protection against Ionizing Radiation and for the Safety of Radiation Sources*. IAEA, pp. 45-56, 1996.
- [2] L. C. Romualdo, M. A. Vieira, H. Schiabel, N. D. Mascarenhas and L. R. Borges, "Mammographic image denoising and enhancement using the Anscombe transformation," *Journal of Digital Imaging*, vol. 26, no. 2, pp. 183-197, 2013.
- [3] A. Jain, S. Singh and V. Bhateja, "A robust approach for denoising and enhancement of mammographic images contaminated with high density impulse noise," *Int. Journal of Convergence Computing*, vol. 1, no. 1, pp. 38-49, 2013.
- [4] G. Wu, J. G. Mainprize and M. Yaffe, "Dose reduction for digital breast tomosynthesis by patch-based denoising in reconstruction," in *Proceedings of the International Workshop on Digital Mammography (IWDM)*, Springer, pp. 21-28, 2012.
- [5] M. Yaffe, "Digital Mammography," in *Handbook of Medical Imaging: Volume 1 Physics and Psychophysics*, Bellingham, SPIE, pp. 329-372, 2000.
- [6] A. Buades, B. Coll and J. Morel, "A Review of Image Denoising Algorithms, with a New One," *Multiscale Model. Simul.*, vol. 4, no. 2, pp. 490-530, 2005.
- [7] K. Dabov, A. Foi, V. Katkovnik and K. Egiazarian, "Image Denoising by Sparse 3-D Transform-Domain Collaborative Filtering," *IEEE Trans. Image Process.*, vol. 16, no. 8, pp. 2080-2095, 2007.
- [8] B. Zhang, M. J. Fadili, J. -L. Starck and J. -C. Olivo-Marin, "Multiscale Variance-Stabilizing Transform for Mixed-Poisson-Gaussian Processes and its Applications in Bioimaging," in *IEEE International Conference on Image Processing*, San Antonio, 2007.
- [9] National Health Service Breast Screening Program, "Calculation of quantitative image quality parameters NHSBSP," NHSBSP Publications, Sheffield, 2009.
- [10] A. Foi, M. Trimeche, V. Katkovnik and K. Egiazarian, "Practical Poissonian-Gaussian noise modeling and fitting for single-image raw-data," *IEEE Transactions on Image Processing*, vol. 17, no. 10, pp. 1737-1754, 2007.
- [11] V. Katkovnik, A. Foi, K. Egiazarian and J. Astola. "From local kernel to nonlocal multiple-model image denoising," *Int. J. Comput. Vision*, vol. 86, no. 1, pp. 1-32, 2010.
- [12] P. Milanfar. "A tour of modern image filtering: New insights and methods, both practical and theoretical," *IEEE Signal Processing Magazine*, vol. 30, no. 1, pp. 106-128, 2013.
- [13] M. Makitalo and A. Foi, "A closed-form approximation of the exact unbiased inverse of the Anscombe transformation," *IEEE Transactions on Image Processing*, vol. 20, no. 9, pp. 2697-2698, 2011.
- [14] L. Cockmartin, P. R. Bakic, H. Bosmans, A. D. A. Maidment, H. Gall, M. Zerhouni and N. W. Marshall, "Power spectrum analysis of an anthropomorphic breast phantom compared to patient data in 2D digital mammography and breast tomosynthesis," in *International Workshop on Digital Mammography*, Springer, pp. 423-429, 2014.
- [15] A.-K. Carton, P. R. Bakic, C. Ullberg, H. Derand and A. D. A. Maidment, "Development of a 3D anthropomorphic breast phantom," *Medical Physics*, vol. 38, no. 2, pp. 891-896, 2011.
- [16] D. D. Pokrajac, A. D. A. Maidment and P. R. Bakic, "Optimized generation of high resolution breast anthropomorphic software phantoms," *Medical Physics*, vol. 39, no. 4, pp. 229-2302, 2012.
- [17] A. Foi, "Signal-dependent noise modeling, estimation, and removal for digital imaging sensors," 2016. [Online]. Available: www.cs.tut.fi/~foi/sensornoise.html. [Accessed 18 July 2016].

Paper 6: Restored Low-Dose Digital Breast Tomosynthesis: A Perception Study

This paper has been submitted to the Physics in Medicine and Biology journal on May, 15, 2017, and is currently under review.

Restored Low-Dose Digital Breast Tomosynthesis: A Perception Study

Lucas R. Borges,^a Predrag R. Bakic,^b Andrew D. A. Maidment,^b Marcelo A. C. Vieira.^a

^aUniversity of São Paulo, São Carlos School of Engineering, Department of Electrical and Computer Engineering, 400 Trabalhador São-carlense Av., São Carlos, Brazil, 13566-590

^bUniversity of Pennsylvania, Hospital of the University of Pennsylvania, Department of Radiology, 3400 Spruce Street, Philadelphia, USA, 19104

Purpose: To investigate the perception of noise and blur from restored low-dose digital breast tomosynthesis (DBT) images.

Methods: Low-dose DBT images were generated using a state-of-the-art simulation algorithm, starting with clinical images acquired from a Selenia Dimensions (Hologic, Inc.) system at the Hospital of the University of Pennsylvania using automatic exposure control (AEC). Low-dose images were first denoised with a state-of-the-art denoising pipeline, developed specifically for DBT images. Denoised and noisy images were then combined in a restoration framework to generate images with signal-to-noise ratio similar to the full-dose images. The quality of restored low-dose images and full-dose images were first compared in terms of an objective non-reference quality metric previously validated for mammography systems. In the second analysis, regions-of-interest (ROIs) were selected from the restored low-dose images and full-dose images, and were displayed side-by-side on a high-resolution monitor. Five medical physics specialists were asked to choose the image containing less noise and less blur using 2-AFC experiments.

Results: The objective metric shows that, after the proposed image restoration framework was applied, images with as little as 60% of the AEC dose yielded similar quality indices when compared to images acquired with the full-dose. In the 2-AFC experiments, the observers were

1
2
3
4 expected to choose randomly between restored and original images when the noise and blur levels
5
6 were equivalent. The results showed that, when the denoising framework was used, a 30%
7
8 30 reduction in dose was possible without any perceived difference in noise or blur.
9
10

11 **Conclusions:** The results of this study indicate that the proposed restoration framework was
12
13 capable of restoring images acquired with up to 30% less dose than the standard acquisition. Note
14
15 that this study evaluated the observer's perception to noise and blur and does not claim that the
16
17 dose of DBT examinations can be reduced with no harm to the detection of cancer. Future work
18
19
20
21 35 is necessary to make any claims regarding detection, localization and characterization of lesions.
22
23

24 **Keywords:** Denoising, image restoration, digital breast tomosynthesis, two-alternative
25
26 forced-choice.
27
28
29
30
31
32
33
34
35
36
37
38
39
40
41
42
43
44
45
46
47
48
49
50
51
52
53
54
55
56
57
58
59
60

40 1. Introduction

1
2
3
4
5
6
7 In breast cancer screening, the x-ray radiation dose must be optimized to ensure that image quality
8 is sufficient for clinical use while radiation dose is kept to a minimum [1]. However, excessively
9 low-dose acquisitions yield images with low quality, which negatively affects the radiologists'
10 interpretation [2,3]. Therefore, there is a compromise between image quality and radiation dose.
11
12
13
14

15
16
17 45 Many denoising methods have been tested to suppress noise from low-dose DBT acquisitions
18 [4,5]. The goal of denoising is to enhance, as much as possible, the signal-to-noise ratio (SNR),
19 starting from images with low SNR. However, due to the Gaussian-Poisson nature of the noise
20 found in DBT images, and particularities such as the detector offset, and spatially varying detector
21 gain, denoising is not an easy task in DBT systems.
22
23
24
25
26
27
28
29

30 50 In previous work, our group has proposed a dedicated denoising pipeline capable of effectively
31 suppressing noise in DBT images [5]. Although the proposed method yields images with high SNR
32 and very low noise, the smooth appearance of the denoised images is not appreciated by
33 radiologists. In the current paper, an alternative approach to DBT denoising is proposed. The
34 method performs a controlled injection of denoised signal into a noisy low-dose acquisition to
35 achieve similar a SNR regime as a reference full-dose acquisition, avoiding the smooth appearance
36 normally observed in denoised images.
37
38
39
40
41
42 55
43
44
45
46
47

48 The contribution of the new method includes the capability of restoring low-dose DBT projections
49 to achieve the image quality obtained using current imaging protocols, considering particularities
50 such as detector offset and spatially varying detector gain. An extensive validation is presented,
51 using an objective image quality metric, sensitive to blur and noise, and a two-alternative
52 forced-choice (2-AFC) human observer study.
53
54
55 60
56
57
58
59
60

2. Materials and methods

2.1. Denoising

The denoising pipeline adopted in this paper has been proposed and validated previously for DBT images [5]. The proposed pipeline accounts for the Gaussian-Poisson noise, as well as the pixel offset and the spatially varying pixel gain. It requires a uniform calibration image, acquired with similar radiographic parameters as the clinical image being denoised. Section 2.3 describes the acquisition of clinical and calibration images required by the denoising algorithm. The block-matching and 3D filtering (BM3D) algorithm [6] was adopted in the denoising process.

2.2. Restoration framework

Let us assume $y_F(i, j)$ as noise-free pixel intensities from a raw DBT projection, acquired with full-dose, at spatial coordinates (i, j) . The observed pixels $z_F^o(i, j)$ can be approximated by a scaled Poisson-Gaussian distribution, as follows:

$$z_F^o(i, j) = \lambda(i, j)\mathcal{P}(y_F(i, j)/\lambda(i, j)) + \sigma_E\eta(i, j) \quad (1)$$

$$E\{z_F^o(i, j)|y_F(i, j)\} = y_F(i, j) \quad (2)$$

$$Var\{z_F^o(i, j)|y_F(i, j)\} = \lambda(i, j)y_F(i, j) + \sigma_E^2 \quad (3)$$

where \mathcal{P} represents a Poisson distribution, $\lambda(i, j)$ is the spatially varying Poisson gain, which is related to the pixel gain defined during the calibration process, σ_E is the standard deviation of the electronic Gaussian noise, E and Var are the expectation and the variance of the distribution, respectively.

Now, let us assume that $y_\gamma(i, j)$ is the noise-free intensity of a DBT image at spatial coordinates (i, j) , acquired using lower radiation dose, reduced by a factor of γ ($0 < \gamma < 1$). Again, the observed pixels $z_\gamma^o(i, j)$ can be approximated to a scaled Poisson-Gaussian distribution, as follows:

$$z_\gamma^o(i, j) = \lambda(i, j)\mathcal{P}\left(y_\gamma(i, j)/\lambda(i, j)\right) + \sigma_E\eta(i, j) \quad (4)$$

$$E\{z_\gamma^o(i, j)|y_\gamma(i, j)\} = y_\gamma(i, j) \quad (5)$$

$$\text{Var}\{z_\gamma^o(i, j)|y_\gamma(i, j)\} = \lambda(i, j)y_\gamma(i, j) + \sigma_E^2 \quad (6)$$

If the system is correctly linearized, *i.e.*, if the pixel intensity changes linearly with the exposure time*, the variance and expectation of the low-dose acquisition can be described as a function of the full-dose acquisition:

$$E\{z_\gamma^o(i, j)|y_\gamma(i, j)\} = y_\gamma(i, j) = \gamma y_F(i, j) \quad (7)$$

$$\text{Var}\{z_\gamma^o(i, j)|y_\gamma(i, j)\} = \lambda(i, j)y_\gamma(i, j) + \sigma_E^2 = \gamma\lambda(i, j)y_F(i, j) + \sigma_E^2 \quad (8)$$

The signal-to-noise ratio (SNR) of each variable at each spatial position is described as:

$$\text{SNR}_F(i, j) = \frac{y_F(i, j)}{\sqrt{\lambda(i, j)y_F(i, j) + \sigma_E^2}} \quad (9)$$

$$\text{SNR}_\gamma(i, j) = \frac{y_\gamma(i, j)}{\sqrt{\lambda(i, j)y_\gamma(i, j) + \sigma_E^2}} = \frac{\gamma y_F(i, j)}{\sqrt{\gamma\lambda(i, j)y_F(i, j) + \sigma_E^2}} \quad (10)$$

Because $0 < \gamma < 1$, the low-dose acquisition has lower SNR, and therefore has lower image quality. The goal of this work is to process the low-dose acquisition to achieve the SNR of a full-dose acquisition ($\text{SNR}_F(i, j)$).

* For more details on the linearization of DBT raw projections please refer to [5].

Let us now consider $z^D(i, j)$ as pixels of the denoised low-dose acquisition. If we assume that the denoising pipeline efficiently removed the noise without excessive signal smoothing, then:

$$E\{z^D(i, j)|y_\gamma(i, j)\} = y_\gamma(i, j) = \gamma y_F(i, j) \quad (11)$$

$$\text{Var}\{z^D(i, j)|y_\gamma(i, j)\} = 0 \quad (12)$$

90 We propose that z^D and z^o be combined using the following weighted average:

$$z_w^o = wz_\gamma^o + (1 - w)z^D \quad (13)$$

The expectation and variance of (13) are:

$$E\{z_w^o(i, j)|y_\gamma(i, j)\} = w\gamma y_F(i, j) + (1 - w)\gamma y_F(i, j) = \gamma y_F(i, j) \quad (14)$$

$$\text{Var}\{z_w^o(i, j)|y_\gamma(i, j)\} = w^2\text{Var}\{z_\gamma^o(i, j)|y_\gamma(i, j)\} + (1 - w)^2\text{Var}\{z^D(i, j)|y_\gamma(i, j)\} \quad (15)$$

Using equations (8), (12) and (14), the SNR of the weighted average is given by:

$$\begin{aligned} \text{SNR}_w(i, j) &= \frac{E\{z_w^o(i, j)|y_\gamma(i, j)\}}{\sqrt{w^2\text{Var}\{z_\gamma^o(i, j)|y_\gamma(i, j)\} + (1 - w)^2\text{Var}\{z^D(i, j)|y_\gamma(i, j)\}}} \quad (16) \\ &= \frac{\gamma y_F(i, j)}{w\sqrt{\gamma\lambda(i, j)y_F(i, j) + \sigma_E^2}} \end{aligned}$$

Because the goal of this work is to achieve the SNR of a full-dose acquisition, equations (9) and (16) can be used to calculate the desired weighting factor w :

$$w = \frac{\gamma\sqrt{\lambda(i, j)y_F(i, j) + \sigma_E^2}}{\sqrt{\gamma\lambda(i, j)y_F(i, j) + \sigma_E^2}} \quad (17)$$

95 Note that, although the exact weighting factor w can be mathematically described by equation (17), the definition of w requires knowledge of the underlying noise-free signal $y_F(i, j)$, which is not accessible in most clinical applications. Fortunately, for the values of $\gamma\lambda(i, j)y_F(i, j)$

considered in this work, the assumption $\gamma\lambda(i, j)y_F(i, j) \gg \sigma_E^2$ can be made with no prejudice to the validity of the work[†], and therefore:

$$w \cong \frac{\gamma\sqrt{\lambda(i, j)y_F(i, j)}}{\sqrt{\gamma\lambda(i, j)y_F(i, j)}} = \sqrt{\gamma} \quad (18)$$

Thus, the SNR regime of a full-dose acquisition can be approximated using the weighted average presented in equation (13), and the weighting factor defined in equation (18).

2.3. Image dataset

A set of 72 patients were selected from the American College of Radiation Imaging Network (ACRIN) PA 4006 dataset. The images were obtained fully anonymized and the study was HIPAA compliant and IRB approved. All the selected images were acquired using Selenia Dimensions (Hologic, Inc.) systems, from the Hospital of the University of Pennsylvania. Raw DBT projections of the cranio-caudal view of the right breast were used in this study, with a total of 72 sets of 15 projections. The patients were chosen to represent a range of breast thickness from 3.5 cm to 8.0 cm. Table 1 presents the breast thickness intervals and radiographic factors of the selected patients.

Table 1 - Breast thickness and radiographic factors intervals of the patients used in this study.

Breast Thickness	kVp	mAs	Number of patients (%)
3.5 – 5	29 – 30	33 – 55	24 (33.3%)
5.1 – 7	31 – 34	45 – 76	29 (40.3%)
7.1 – 8	35 – 36	70 – 78	19 (26.4%)

Both the denoising and simulation of dose reduction algorithms require a calibration image acquired with radiographic factors close to the ones used in the clinical acquisition. Calibration

[†] For further clarification on this assumption, please refer to the Appendix A.

1
2
3
4 images were acquired using a system of the same model, at the same institution as the clinical
5
6 115 images. Uniform PMMA blocks were used to approximate the attenuation of the breast. A wide
7
8 range of radiographic parameters and PMMA thickness were used to build a calibration dataset.
9
10 The calibration image used for each patient was selected to be the closest in thickness, kVp and
11
12 mAs. Table 2 shows the radiographic parameters used for each calibration acquisition.
13
14
15

16 Table 2 – Radiographic factors and thickness of the uniform PMMA phantom of each calibration image.

PMMA Thickness (cm)	kVp	mAs
4	29	33, 39, 45, 48, 54, 60, 63
4	30	45, 48, 54
6	31	45, 48, 54, 60, 63, 69
6	32	48, 54, 60, 63, 64, 69, 75, 78
6	33	54, 60, 64, 70
6	34	60, 63, 64, 70, 76
8	35	70, 75, 76, 78
8	36	69, 75, 78

17
18
19
20
21
22
23
24
25
26
27
28
29
30
31
32
33 120 **2.4. Simulation of dose reduction**

34
35
36 To simulate images acquired at lower radiation levels, this work adopted the simulation method
37
38 described in [7]. The simulation algorithm has been widely validated by our group, and was
39
40 especially designed for DBT systems. The simulation method requires a calibration image acquired
41
42 with radiographic factors similar to the ones used for the clinical acquisition. In this work, we
43
44 investigated 90%, 80%, 70%, 60%, and 50% of the dose reported by the AEC of the clinical
45
46 125 system.
47
48
49
50

51 **2.5. No-reference anisotropic image quality index (NAQI)**

52
53
54 To perform an objective measurement of the image quality in clinical images, this work adopted
55
56 the no-reference anisotropic quality index (NAQI), extensively tested and validated in previous
57
58
59
60

1
2
3 130 works [8-10]. The NAQI is sensitive to noise and blur present in the image, and does not require
4
5 an approximation of the ground-truth signal to estimate the image quality. Higher values of NAQI
6
7 can be found in images with lower noise levels and less blur.
8
9

10 11 **2.6. Two-alternative forced-choice (2-AFC) observer study** 12 13

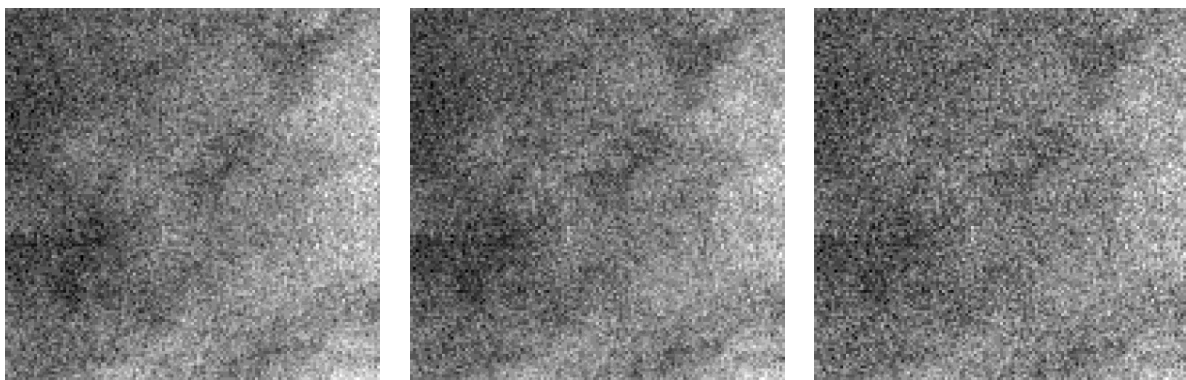
14
15 A 2-AFC observer study was conducted to investigate the differences in noise and blur levels
16
17 135 between restored low-dose and full-dose acquisitions. Sets of two images were presented to human
18
19 observers and two questions were asked: “1 – Which image contains less noise?” and “2 – Which
20
21 *image contains less blur?*”. One of the displayed images was a 512×512 region of interest (ROI)
22
23 taken from a reconstructed slice of a DBT exam at 10mm above the breast support, acquired with
24
25 the system AEC, representing the full-dose acquisition. The second image contained the
26
27 corresponding ROI taken from a reconstructed slice of a DBT exam at a simulated lower dose,
28
29 140 processed to yield the same SNR as the full-dose image. The image order was randomized, and
30
31 the readers were blinded as to which of the images was full-dose or restored low-dose. The readers
32
33 were expected to guess (~50% selection rate) when there were no perceived differences in noise
34
35 and blur levels between the full-dose and restored low-dose images.
36
37
38
39
40

41
42 145 A group of five medical physics specialists participated on the experiment, with 360 readings each,
43
44 for a total of 1,800 readings. Before the reading session, each of the observers were trained by an
45
46 instructor, to align the interpretation of noise and blur from the image. Readers were instructed to
47
48 look for uniform portions of the ROI and assess the intensity of the random fluctuations caused by
49
50 noise. The ROI with more fluctuations are considered noisier. For the blur evaluation, readers were
51
52 instructed to look for borders from anatomical features inside the ROI. The ROI containing
53
54 150 smoother borders should be selected as blurry. The answers were recorded using software designed
55
56
57
58
59
60

1
2
3
4 for this study, and each observer performed all readings during one session. All images used in the
5
6 human observers' experiment were reconstructed using a commercially available system (Briona
7
8 Standard v4.0, Real Time Tomography, Villanova, PA). The reconstructed data was assessed using
9
10 a RadiForce GS320 monitor (Eizo, Japan). The experiment was conducted in a darkened room
11
12 appropriately prepared for human observers experiments, at the Hospital of the University of
13
14 Pennsylvania.
15

16 17 18 **3. Results and discussion**

19
20
21 The proposed framework was prototyped using MATLAB. Figure 1 shows the example of a ROI
22
23 taken from the central projection of a DBT acquired at full-dose, after the framework was applied,
24
25 160 and before the framework was applied.
26
27
28
29



43 (a) Original full-dose

44 (b) Restored low-dose (50%)

45 (c) Original low-dose (50%)

46 Figure 1 – Visual example containing a magnified ROI.

47 48 **3.1. Objective analysis**

49
50
51 To investigate the quality of restored images, the NAQI was calculated on the raw projections of
52
53 the full-dose acquisition, simulated low-dose before the restoration process, and simulated
54
55 165 low-dose after the proposed framework was applied. Figure 2 shows the results.
56
57
58
59
60

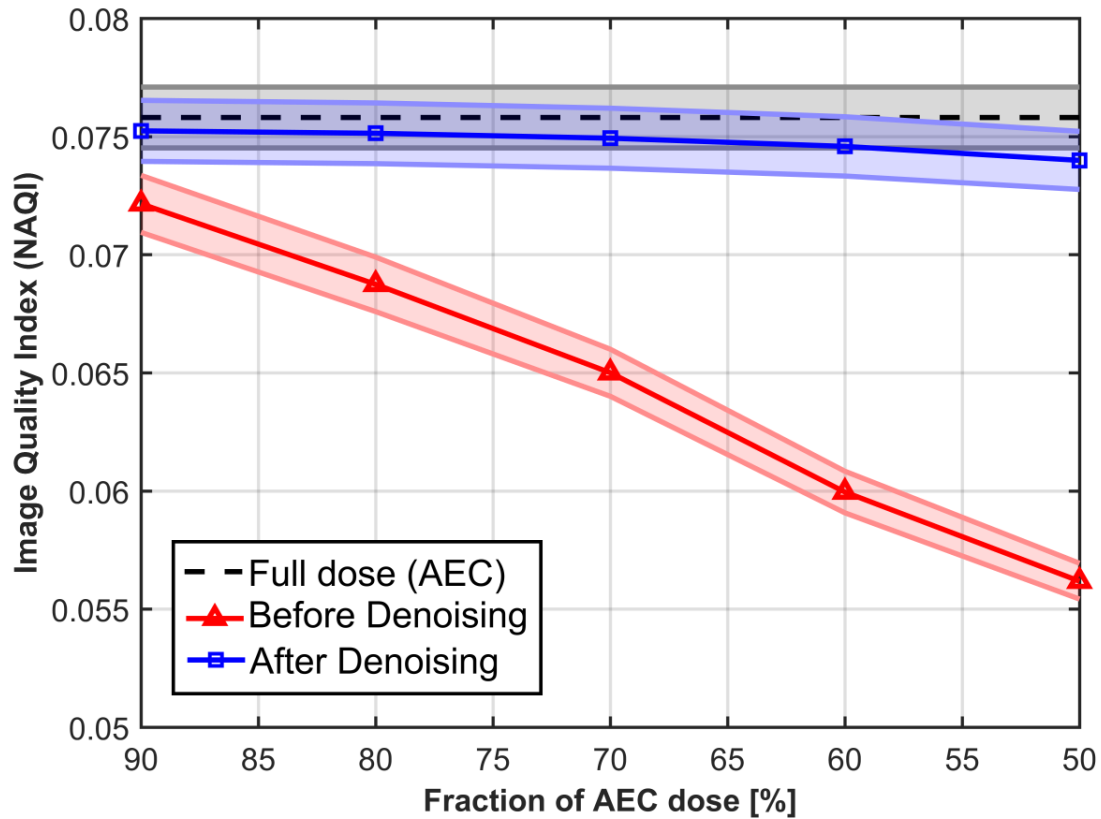


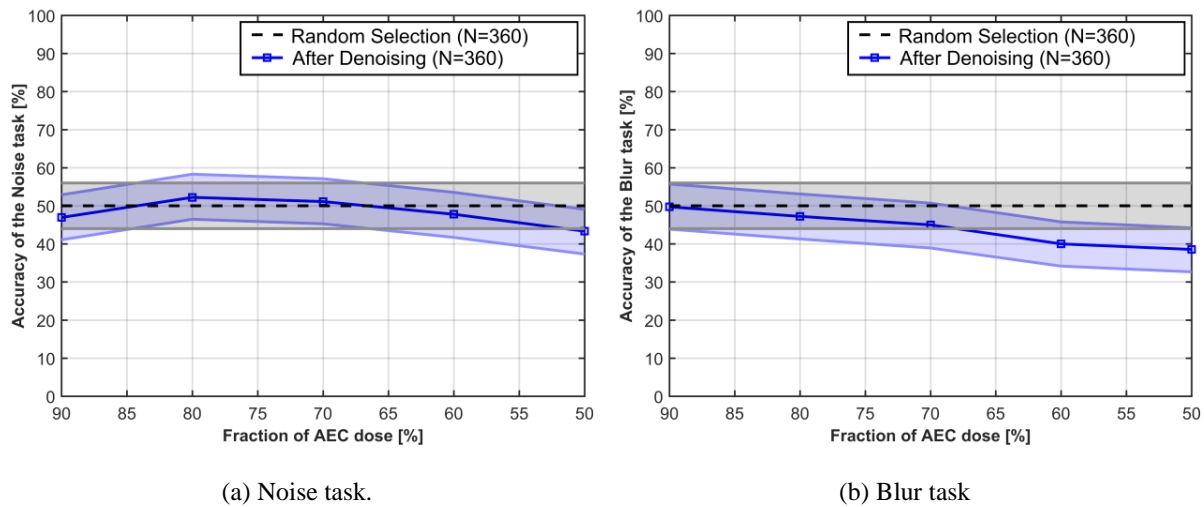
Figure 2 – Image quality metric NAQI at a range of dose levels.

The shaded areas of Figure 2 represent the 95% confidence interval of each dose. The dashed line represents the NAQI calculated at the full-dose acquisition, which is the goal of the proposed image processing framework. As seen by the triangular markers, image quality drops significantly with dose reduction. The quality was recovered to values close to the full-dose acquisition (dashed line) after the proposed method was applied, as indicated by the square markers.

3.2. Subjective analysis

The first task analyzed was the selection of the image containing lower noise. Observers were expected to choose randomly (50%) between the full-dose acquisition and restored low-dose acquisition if the two images have the same noise levels. Figure 3(a) shows the results.

1
2
3
4 It is important to notice the drop in selection frequency when images acquired with 50% dose were
5 used. This point shows where the limitations of the denoising algorithms start to play a role, and
6
7
8 180 the observers begin to select the full-dose image more often than the restored image. This indicates
9
10 higher levels of noise in the restored data, suggesting that complete image restoration is not
11
12 possible with this dose reduction.
13
14



31
32 (a) Noise task. (b) Blur task
33 Figure 3 – Observers' accuracy at choosing the image containing less noise (a) or blur (b).
34
35

36 The process of signal denoising is a compromise between noise suppression and signal smoothing.
37
38 Thus, the second aspect analyzed was the image blur. Again, observers were expected to choose
39
40 randomly (50%) between the full-dose acquisition and restored low-dose acquisition if the two
41 185 images have the same blur levels. Figure 3(b) shows the results.
42
43
44

45 As seen in Figure 3(b), there was a considerable drop in selection after a 30% of dose reduction,
46
47 indicating that the readers could identify the restored images due to the smooth appearance.
48
49
50

51 Statistical analysis was performed using a two-sided sign test. Table 3 shows the results. In the
52
53
54 190 tests, H=0 indicates that the null hypothesis cannot be rejected at 90% confidence, and therefore
55
56
57
58
59
60

the observers had no statistical difference in selection between restored low-dose and full-dose images. When $H=1$, the observers had a statistical difference in selection between images.

Table 3 – Results of the sign test. The hypothesis is rejected ($H=1$) when the readers had a statistically significant difference in selection between restored low-dose and full-dose images.

	90% AEC dose H (p)	80% AEC dose H (p)	70% AEC dose H (p)	60% AEC dose H (p)	50% AEC dose H (p)
Noise	0 (0.62)	0 (1.00)	0 (1.00)	0 (0.62)	0 (0.37)
Blur	0 (0.62)	0 (0.62)	0 (0.12)	1 (0.06)	1 (0.06)

195 The analysis from Table 3 shows that the observers were not able to perceive any differences in noise levels even at 50% of the dose, after the restoration framework was applied. However, the smooth appearance of the restored images could be perceived at 40% dose reduction. Thus, the results show that a 30% reduction in dose was possible without any differences in noise or blur being perceived by human observers.

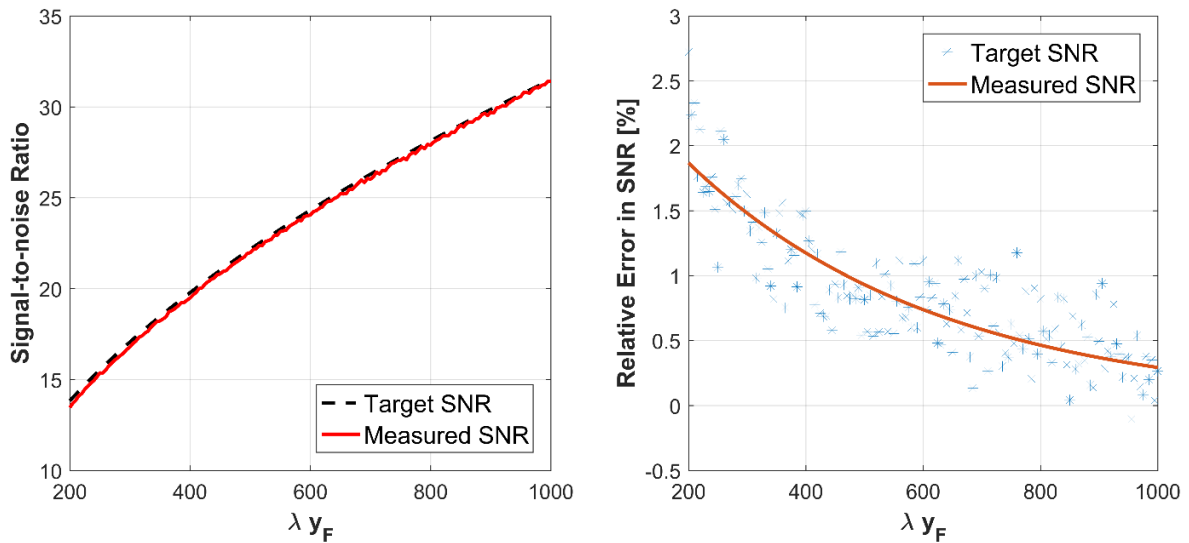
200 4. Conclusions

This work investigates the perception of noise and blur in restored low-dose images. The innovative aspect of the proposed restoration framework is the injection of denoised signal into the noisy image, to reach the SNR regime of a full-dose acquisition. This process is important to avoid excessive smoothness of the restored image. While we do not claim that the dose of DBT examinations can be reduced with no harm to the detection of cancer, the results suggest that, with 205 the use of the proposed restoration framework, no differences can be perceived in terms of noise and blur for images with 70% of the standard radiation dose. A detailed future study is necessary to investigate the impact regarding detection, localization and characterization of lesions.

Appendix A – Approximations on the weighting factor w

210 In this appendix, we investigate the approximation on w discussed in the manuscript. To quantify
 211 the errors resulted from the approximation, a hypothetical signal, with $200 < \lambda y_F < 1000$, was
 212 synthetically generated, and Poisson-Gaussian noise was injected to it. The selected range of λy_F
 213 and the parameters of the Poisson-Gaussian noise represent the values commonly found in systems
 214 of the type described in the manuscript ($\lambda = 0.1, \sigma_E = 3$).

215 Figure 4(a) shows the measured and target signal-to-noise ratio (SNR) achieved by the proposed
 216 algorithm with and without the approximation (for $\gamma = 0.5$). Figure 4(b) shows the relative error
 217 of the SNR. The error is lower than 2%, and it decreases exponentially as the signal increases.



(a) Standard deviation.

(b) Relative error of the standard deviation.

Figure 4 – SNR and relative error caused by the approximation on the weighting factor w .

Acknowledgements

220 This work was supported by the São Paulo Research Foundation (grant 2016/25750-0), the
Brazilian Foundation for the Coordination of Improvement of Higher Education Personnel (grant
88881.030443/2013-01), the Burroughs Wellcome Fund (IRSA 1016451), the Komen Foundation
(grant IIRI326610), the National Institutes of Health and National Cancer Institute (grant
1R01CA154444).

225 The authors would like to thank Real Time Tomography for providing the reconstruction software,
Ms. Kristen Lau for her support during the acquisition of images, and the team of medical
physicists who volunteered for participating in the 2-AFC experiment. ADAM is a member of the
scientific advisory board, and a shareholder of RTT.

References

230 ¹ International Atomic Energy Agency, “Appendix II: Medical exposure,” in: International Basic
Safety Standards for Protection against Ionizing Radiation and for the Safety of Radiation Sources.
IAEA, 45-56 (1996).

235 ² R.S. Saunders, J.A. Baker, D.M. DeLong, J.P. Johnson, and E. Samei, “Does image quality
matter? Impact of resolution and noise on mammographic task performance,” *Med. Phys.* **34**(10),
3971–3981 (2007).

³ M. Ruschin, P. Timberg, M. Bath, B. Hemdal, T. Svahn, R. Saunders, E. Samei, I. Andersson, S.
Mattsson, D.P. Chakraborty and A. Tingberg, “Dose dependence of mass and microcalcification
detection in digital mammography: free response human observer studies,” *Med. Phys.* **34**(2), 400–
407 (2007).

240 ⁴ X. Wang, J.G. Mainprize, G. Wu, M.J. Yaffe “Wiener filter for filtered back projection in digital
breast tomosynthesis,” *Proc. SPIE 8313, Medical Imaging 2012: Physics of Medical Imaging*,
83134Z (2012).

245 ⁵ L.R. Borges, P.R. Bakic, A. Foi, A.D.A. Maidment, and M.A.C. Vieira, “Pipeline for effective
denoising of digital mammography and digital breast tomosynthesis,” *Proc. SPIE 10132, Medical
Imaging 2017: Physics of Medical Imaging*, 1013206 (2017).

1
2
3
4
5
6
7
8
9
10
11
12
13
14
15
16
17
18
19
20
21
22
23
24
25
26
27
28
29
30
31
32
33
34
35
36
37
38
39
40
41
42
43
44
45
46
47
48
49
50
51
52
53
54
55
56
57
58
59
60

⁶ K. Dabov, A. Foi, V. Katkovnik and K. Egiazarian, "Image Denoising by Sparse 3-D Transform-Domain Collaborative Filtering," *IEEE Trans. Image Process.* **16**(8), 2080-2095 (2007).

⁷ L.R. Borges, I. Guerrero, P.R. Bakic, A. Foi, A.D.A. Maidment, and M.A.C. Vieira, "Method of simulating dose in digital breast tomosynthesis," Currently Under Review. Available at: < http://www.cs.tut.fi/~foi/papers/Borges-DBT_Sim.pdf >.

⁸ H.C.R. de Oliveira, B. Barufaldi, L.R. Borges, S. Gabarda, P.R. Bakic, A.D.A. Maidment, M.A.C. Vieira, "Validation of no-reference image quality index for the assessment of digital mammographic images," *Proc. SPIE 9787, Medical Imaging 2016: Image Perception, Observer Performance, and Technology Assessment*, 978713 (2016).

⁹ B. Barufaldi, L.R. Borges, M.A.C. Vieira, S. Gabarda, A.D.A. Maidment, P.R. Bakic, D.D. Pokrajac, H. Schiabel, "The effect of breast composition on a no-reference anisotropic quality index for digital mammography," *Proc. IWDM 2016, LNCS 9699*, 226-233 (2016).

¹⁰ B. Barufaldi, L.R. Borges, P.R. Bakic, M.A.C. Vieira, H. Schiabel, A.D.A. Maidment, "Assessment of the automatic exposure control performance in digital mammography using a no-reference anisotropic quality index," *Proc. SPIE 10136, Medical Imaging 2017: Image Perception, Observer Performance, and Technology Assessment*, 101360U (2017).

Conclusions

In this Ph.D. thesis, we have presented and validated an image restoration framework capable of recovering DBT images acquired at low radiation doses, to achieve the SNR regime of full-dose acquisitions.

In the first portion of the work, a few operators were designed to perform signal-dependent noise injection into observed data. The first algorithm, presented in **Paper 1**, assumed a Poisson noise model and was validated on DM images, yielding low errors in terms of noise variance and noise power spectrum.

Some limitations are related to the first proposed algorithm. The assumption of pure Poisson noise, for example, holds true for DM systems, but not for other systems such as DBT.

The algorithm also considered a flat noise spectrum, *i.e.*, no pixel crosstalk. The validation was performed on a commercial system that reports minimal pixel crosstalk. Thus, the error on the NNPS may increase if the algorithm is applied to other system models.

Furthermore, the variance-stabilization used on the first algorithm yields errors that decrease asymptotically with the counting values. Thus, it reports high errors for applications with low photon fluence.

The evaluation of the first algorithm, applied to DBT, was performed in **Paper 2**, and the limitations of a pure Poisson model assumption were made evident on this work. Note that **Paper 2** is a short work submitted to a conference, and therefore was not subject to a full peer-reviewed process. Some aspects such as the depth dependency of the error shown in Figure 7 (b) of this work are still not fully understood.

The next operator, presented in **Paper 3**, was optimized to perform noise injection even at low photon fluence applications. This optimization is important for noise injection into applications such as microscopy. However, to be used in DBT systems, the algorithm still needed to be adapted to account for the Poisson-Gaussian model, and the pixel crosstalk.

In **Paper 4**, the final noise injection operator was presented and validated using DBT

images. Both the Poisson-Gaussian noise model and pixel crosstalk were considered in the operator. The algorithm was validated using both objective metrics as well as a human observers experiment, which indicated that no differences in noise levels between simulated and real images could be perceived.

Once the algorithm for simulation of dose reduction was proposed and validated, the next portion of this thesis focused on the improvement of the image quality in low-dose DBT acquisitions. First, a denoising pipeline was proposed. The pipeline accounted for a Poisson-Gaussian noise model, with spatially varying quantum gain. **Paper 5** presented the formalization and the validation of the pipeline, which showed that the use of a more accurate noise model improved the efficiency of the denoising algorithm. Note that **Paper 5** is a short work submitted to a conference, and therefore was not subject to a full peer-reviewed process. One limitation of this work is the experimental setup used for the estimation of the modulation transfer function (MTF). Due to the non-linearity of the filter used, the proposed experiment is not optimal and could be replaced by better alternatives.

The final results of this Ph.D. thesis were presented in **Paper 6**. Using the simulation method proposed previously, and a set of 72 clinical DBT exams, a human observer experiment was performed. The experiment investigated the perceived difference in terms of noise and blur levels between full-dose and restored low-dose images. The results showed that dose reductions of up to 30% could be achieved, with no perceived changes in noise and blur levels, when the proposed restoration framework was applied.

Note that, although the results presented in this Ph.D. thesis indicate that dose savings could be achieved by improving the signal processing aspects of images acquired at lower radiation levels, a detailed work is necessary before this framework is applied into a clinical context.

9.1 Future works

Although this entire thesis was developed with focus on breast imaging modalities, the algorithms proposed in this work are agnostic to the imaging modality, as long as a Poisson or Poisson-Gaussian noise model is appropriate. Thus, there are many possible extensions to this Ph.D. thesis.

One immediate extension of this work is to apply the dose reduction algorithm to investigate the feasibility of achieving dose savings by improving image reconstruction, image enhancement, protocol optimization, among others. Furthermore, it can be used to evaluate quality metrics, and quality assurance protocols.

The simulation and restoration algorithms could also be used together to build pre-clinical trials for dose savings in other imaging modalities modeled by a Poisson or Poisson-Gaussian noise distribution.

Furthermore, **Paper 6** investigated the perception of blur and noise from restored images. Another immediate extension of this work would be investigating the effect of the restoration framework on the detection, localization, and characterization of these lesions.

Finally, a complete statistical risk assessment could be performed to estimate the impact of the dose reduction into the number of lives saved and the possible reduction on the number of induced cancers on breast screening programs.

9.2 Publications

Other scientific publications are related to this Ph.D. thesis, and were developed with the direct support of the author:

- BORGES, L.R.; GUERRERO, I.; BAKIC, P.R.; MAIDMENT, A.D.A.; VIEIRA, M.A.C. Gaussian-Poisson noise estimation from individual mammography images. In: **Proceedings of the Workshop de Visão Computacional**, Campo Grande, 2016.
- NUNES, P.F.; BINDILATTI, A.A.; OLIVEIRA, H.C.R.; BORGES, L.R.; BAKIC, P.R.; MAIDMENT, A.D.A.; MASCARENHAS, N.D.A.; VIEIRA, M.A.C. Nova proposta do algoritmo de médias não-locais para filtragem de ruído quântico na mamografia digital. In: **Proceedings of the Congresso Brasileiro de Engenharia Biomédica**, Foz do Iguaçu, 2016.
- BARUFALDI, B.; BORGES, L.R.; VIEIRA, M.A.C.; GABARDA, S.; MAIDMENT, A.D.A.; BAKIC, P.R.; POKRAJAC, D.D.; SCHIABEL, H. The Effect of Breast Composition on a No-reference Anisotropic Quality Index for Digital Mammography. In: Anders Tingberg; Kristina Lang; Pontus Timberg. **Breast Imaging**. 1ed.: Springer, v. 9699, p. 226-233, 2016.
- OLIVEIRA, H.C.R.; BARUFALDI, B.; BORGES, L.R.; GABARDA, S.; BAKIC, P.R.; MAIDMENT, A.D.A.; SCHIABEL, H.; VIEIRA, M.A.C. The Effect of Breast Density on a No-reference Anisotropic Quality Index for Digital Mammography. In: **Proceedings of the SPIE Medical Imaging 2016: Image Perception**, San Diego, 2016.
- BORGES, L.R.; VIEIRA, M.A.C.; FOI, A. Unbiased Noise Injection in Variance-Stabilized Range. In: **Proceedings of the SIAM Conference on Imaging Science**, Albuquerque, 2016.

- ❑ BORGES, L.R.; VIEIRA, M.A.C.; FOI, A. Unbiased Injection of Signal-Dependent Noise in Variance- Stabilized Range. In: **Proceedings of the IEEE Workshop on Statistical Signal Processing**, Palma de Mallorca, 2016.
- ❑ BORGES, L.R.; HWUANG, E.; ACCIAVATTI, R. J.; VIEIRA, M. A. C.; MAIDMENT, A. D. A. Tomosynthesis Reconstruction Based on Principal Component Analysis (PCA). In: **Radiological Society of North America**, 2016, Chicago, 2016.
- ❑ BORGES, L.R.; BAKIC, P.R.; MAIDMENT, A.D.A.; VIEIRA M.A.C. Metal Artifact Reduction using a patch-based reconstruction for digital breast tomosynthesis. In: **Proceedings of the SPIE Medical Imaging 2017: Physics of Medical Imaging**, Orlando, 2017.
- ❑ OLIVEIRA, H.C.R.; MORAES, D.R.; RECHE, G.A.; BORGES, L.R.; CATINI, J.H.; BARROS, N.; MELO, C.F.E.; GONZAGA, A.; VIEIRA M.A.C. A New Texture Descriptor Based on Local Micro-Patter for Detection of Architectural Distortion in Mammographic Images. In: **Proceedings of the SPIE Medical Imaging 2017: Physics of Medical Imaging**, Orlando, 2017.
- ❑ BARUFALDI, B.; BORGES, L.R.; BAKIC, P.R.; VIEIRA, M.A.C.; SCHIABEL, H.; MAIDMENT, A.D.A. Assessment of automatic exposure control performance in digital mammography using a no-reference anisotropic quality index. In: **Proceedings of the SPIE Medical Imaging 2017: Physics of Medical Imaging**, Orlando, 2017.
- ❑ BARUFALDI, B.; BORGES, L.R.; BAKIC, P.R.; VIEIRA, M.A.C.; SCHIABEL, H.; MAIDMENT, A.D.A. Assessment of automatic exposure control performance in digital mammography using a no-reference anisotropic quality index. In: **Proceedings of the SPIE Medical Imaging 2017: Physics of Medical Imaging**, Orlando, 2017.

Bibliography

BAKER, J. A.; LO, J. Y. Breast tomosynthesis: state-of-the-art and review of the literature. **Academic radiology**, 2011. Elsevier, v. 18, n. 10, p. 1298–1310, 2011.

BATH, M. et al. Method of simulating dose reduction for digital radiographic systems. **Radiation Protection Dosimetry**, 2005. v. 114, n. 1-3, p. 253–259, 2005.

BORGES, L. R.; VIEIRA, M. A. da C.; FOI, A. Unbiased injection of signal-dependent noise in variance-stabilized range. **IEEE Signal Processing Letters**, 2016. v. 23, n. 10, p. 1494–1498, Oct 2016. ISSN 1070-9908.

CONANT, E. F. et al. Breast cancer screening using tomosynthesis in combination with digital mammography compared to digital mammography alone: a cohort study within the prospr consortium. **Breast Cancer Research and Treatment**, 2016. v. 156, n. 1, p. 109–116, 2016. ISSN 1573-7217. Disponível em: <<http://dx.doi.org/10.1007/s10549-016-3695-1>>.

DURAND, M. A. et al. Early clinical experience with digital breast tomosynthesis for screening mammography. **Radiology**, 2015. v. 274, n. 1, p. 85–92, 2015. PMID: 25188431. Disponível em: <<http://dx.doi.org/10.1148/radiol.14131319>>.

FRUSH, D. P. et al. Computer-simulated radiation dose reduction for abdominal multidetector ct of pediatric patients. **American Journal of Roentgenology**, 2002. Am Roentgen Ray Soc, v. 179, n. 5, p. 1107–1113, 2002.

GONZALEZ, A. B. de et al. Estimated risk of radiation-induced breast cancer from mammographic screening for young brca mutation carriers. **Journal of the National Cancer Institute**, 2009. v. 101, n. 3, p. 205–209, 2009.

GREESS, H. et al. Dose reduction in computed tomography by attenuation-based on-line modulation of tube current: evaluation of six anatomical regions. **European radiology**, 2000. Springer, v. 10, n. 2, p. 391–394, 2000.

HAUS, A.; YAFFE, M. Screen-film and digital mammography. image quality and radiation dose considerations. **Radiologic clinics of North America**, 2000. v. 38, n. 4, p. 871–898, July 2000. ISSN 0033-8389.

HUDA, W. et al. Experimental investigation of the dose and image quality characteristics of a digital mammography imaging system. **Medical Physics**, 2003. v. 30, n. 3, p. 442, 2003.

INCA. Estimativa 2016: Incidência de câncer no brasil. **Instituto Nacional de Câncer José Alencar Gomes da Silva**, 2016. 2016.

KALENDER, W. A.; WOLF, H.; SUESS, C. Dose reduction in ct by anatomically adapted tube current modulation. ii. phantom measurements. **Medical physics**, 1999. Wiley Online Library, v. 26, n. 11, p. 2248–2253, 1999.

LEIPSIC, J. et al. Estimated radiation dose reduction using adaptive statistical iterative reconstruction in coronary ct angiography: the erasir study. **American Journal of Roentgenology**, 2010. Am Roentgen Ray Soc, v. 195, n. 3, p. 655–660, 2010.

MACKENZIE, A. et al. Image simulation and a model of noise power spectra across a range of mammographic beam qualities. **Medical Physics**, 2014. v. 41, n. 12, 2014.

_____. Conversion of mammographic images to appear with the noise and sharpness characteristics of a different detector and x-ray system. **Medical Physics**, 2012. v. 39, n. 5, p. 2721–2734, 2012.

MANDUCA, A. et al. Projection space denoising with bilateral filtering and ct noise modeling for dose reduction in ct. **Medical Physics**, 2009. American Association of Physicists in Medicine, v. 36, n. 11, p. 4911–4919, 2009. ISSN 2473-4209. Disponível em: <<http://dx.doi.org/10.1118/1.3232004>>.

MASSOUMZADEH, P. et al. Validation of ct dose-reduction simulation. **Medical physics**, 2009. Wiley Online Library, v. 36, n. 1, p. 174–189, 2009.

NCI. **NCI-funded Breast Cancer Surveillance Consortium (HHSN261201100031C)**. 2009. Disponível em: <<http://breastscreening.cancer.gov/>>.

SAUNDERS, R. S. et al. Does image quality matter? impact of resolution and noise on mammographic task performance. **Medical Physics**, 2007. v. 34, n. 10, p. 3971–3981, 2007.

SAUNDERS, R. S.; SAMEI, E. A method for modifying the image quality parameters of digital radiographic images. **Medical Physics**, 2003. v. 30, n. 11, p. 3006–3017, 2003.

SILVA, A. C. et al. Innovations in ct dose reduction strategy: application of the adaptive statistical iterative reconstruction algorithm. **American Journal of Roentgenology**, 2010. Am Roentgen Ray Soc, v. 194, n. 1, p. 191–199, 2010.

SKAANE, P. et al. Two-view digital breast tomosynthesis screening with synthetically reconstructed projection images: Comparison with digital breast tomosynthesis with full-field digital mammographic images. **Radiology**, 2014. v. 271, n. 3, p. 655–663, 2014. PMID: 24484063. Disponível em: <<http://dx.doi.org/10.1148/radiol.13131391>>.

SVALKVIST, A.; BATH, M. Simulation of dose reduction in tomosynthesis. **Medical Physics**, 2010. v. 37, n. 1, p. 258–269, 2010.

VERONESI, U. et al. Breast cancer. **The Lancet**, 2005. v. 365, n. 9472, p. 1727 – 1741, 2005. ISSN 0140-6736.

VIEIRA, M. A.; BAKIC, P. R.; MAIDMENT, A. D. Effect of denoising on the quality of reconstructed images in digital breast tomosynthesis. **Proc. SPIE Medical Imaging**, 2013. v. 8668, p. 86680C1–14, 2013.

VIEIRA, M. A. et al. Feasibility study of dose reduction in digital breast tomosynthesis using non-local denoising algorithms. **Proc. SPIE Medical Imaging**, 2015. p. 94122C–94122C, 2015.

WANG, J. et al. Penalized weighted least-squares approach to sinogram noise reduction and image reconstruction for low-dose x-ray computed tomography. **IEEE transactions on medical imaging**, 2006. IEEE, v. 25, n. 10, p. 1272–1283, 2006.

WU, G.; MAINPRIZE, J.; YAFFE, M. Dose reduction for digital breast tomosynthesis by patch-based denoising in reconstruction. **Breast Imaging**, 2012. Springer, p. 721–728, 2012.

YAFFE, M. J.; MAINPRIZE, J. G. Risk of radiation-induced breast cancer from mammographic screening. **Radiology**, 2011. v. 258, n. 1, p. 98–105, 2011.